KfK 4652
Dezember 1989

The Karlsruhe 4π Barium Fluoride Detector

K. Wisshak, K. Guber, F. Käppeler, J. Krisch,
H. Müller, G. Rupp, F. Voß
Institut für Kernphysik
Hauptabteilung Ingenieurtechnik

Kernforschungszentrum Karlsruhe

KERNFORSCHUNGSZENTRUM KARLSRUHE
Institut für Kernphysik
Hauptabteilung Ingenieurtechnik

KfK 4652

THE KARLSRUHE 4π BARIUM FLUORIDE DETECTOR

K. Wisshak, K. Guber, F. Käppeler, J. Krisch, H. Müller, G. Rupp, and F. Voß

Kernforschungszentrum Karlsruhe GmbH, Karlsruhe

Kernforschungszentrum Karlsruhe GmbH
Postfach 3640, 7500 Karlsruhe 1

ISSN 0303-4003

ZUSAMMENFASSUNG

DER KARLSRUHER 4π BARIUM FLUORID DETEKTOR

Es wurde ein neuartiges Experiment aufgebaut, um Wirkungsquerschnitte für Neutroneneinfang im Energiebereich von 5 bis 200 keV sehr genau zu bestimmen. Der Karlsruher 4π Barium Fluorid Detektor besteht aus 42 Kristallen in der Form von fünf- und sechseckigen Pyramidenstümpfen. Sie bilden eine Kugelschale mit 10 cm Innenradius und 15 cm Dicke. Jeder Kristall ist mit Reflektor und Photomultiplier ausgerüstet und stellt einen unabhängigen Detektor für Gammastrahlung dar. Jedes Modul erfaßt von einer Gammaquelle im Zentrum des Detektors den gleichen Raumwinkel.

Die Energieauflösung des 4π Detektors beträgt 14 % bei 662 keV und 7 % bei 2.5 MeV Gammaenergie. Die Zeitauflösung ist 500 ps und die Nachweiswahrscheinlichkeit für die volle Energie der Gammaquanten 90 % bei 1 MeV. Diese einmalige Kombination von Eigenschaften wurde jetzt bei einem Detektor für Gammastrahlen ermöglicht, da seit kurzem Barium Fluorid Kristalle mit einem Volumen bis zu 2.5 l erhältlich sind. Mit dem Detektor kann die Gamma-Kaskade nach Neutroneneinfang mit 95 % Wahrscheinlichkeit oberhalb einer Schwelle von 2.5 MeV nachgewiesen werden.

Die Neutronen werden mit dem gepulsten Protonenstrahl eines Van de Graaff Beschleunigers über die $^{7}Li(p,n)^{7}Be$ Reaktion erzeugt. Durch geeignete Wahl der Protonenenergie läßt sich das Neutronenspektrum im Energiebereich von 5 bis 200 keV an die experimentellen Anforderungen anpassen. Ein gebündelter Neutronenstrahl geht durch den Detektor und trifft die Probe in seinem Zentrum. Die Energie der eingefangenen Neutronen wird über ihre Flugzeit bestimmt, der Flugweg beträgt 77 cm.

Die Kombination aus kurzem Flugweg, 10 cm Innenradius der BaF_2 Kugelschale und dem geringen Einfangquerschnitt von Barium erlaubt es, den Untergrund durch Einfang gestreuter Neutronen im Szintillatormaterial auf Grund seiner Zeitstruktur vom Messeffekt zu unterscheiden. Diese Eigenschaft, zusammen mit der guten Energieauflösung und der hohen Ansprechwahrscheinlichkeit, ermöglicht es, die verschiedenen Komponenten des Untergrundes so gut vom Messeffekt zu trennen, daß das Verhältnis der Wirkungsquerschnitte zweier Isotope mit einer Genauigkeit $\leq$1.2 % bestimmt werden kann.

Der Detektor wird für astrophysikalische Untersuchungen, die der Erforschung des Ursprungs der schweren Elemente dienen, eingesetzt.

ABSTRACT

A new experimental approach has been implemented for accurate measurements of neutron capture cross sections in the energy range from 5 to 200 keV. The Karlsruhe 4π Barium Fluoride Detector consists of 42 crystals shaped as hexagonal and pentagonal truncated pyramids forming a spherical shell with 10 cm inner radius and 15 cm thickness. All crystals are supplied with reflector and photomultiplier, thus representing independent gamma-ray detectors. Each detector module covers the same solid angle with respect to a gamma-ray source located in the centre.

The energy resolution of the 4π detector is 14% at 662 keV and 7% at 2.5 MeV gamma-ray energy, the overall time resolution is 500 ps and the peak efficiency 90% at 1 MeV. This unique combination of attractive features for a gamma-ray detector became possible by the recent availability of large barium fluoride crystals with volumes up to 2.5 l. The detector allows to register capture cascades with 95% probability above a threshold energy of 2.5 MeV in the sum energy spectrum.

Neutrons are produced via the $^7Li(p,n)^7Be$ reaction using the pulsed proton beam of a Van de Graaff accelerator. The neutron spectrum can be taylored according to the experimental requirements in an energy range from 5 to 200 keV by choosing appropriate proton energies. A collimated neutron beam is passing through the detector and hits the sample in the centre. The energy of captured neutrons is determined via time of flight, the primary flight path being 77 cm.

The combination of short primary flight path, a 10 cm inner radius of the spherical BaF_2 shell, and the low capture cross section of barium allows to discriminate background due to capture of sample scattered neutrons in the scintillator by time of flight, leaving part of the neutron energy range completely undisturbed. This feature together with the high efficiency and good energy resolution for capture gamma-rays allows to separate the various background components reliably enough, that the capture cross section ratio of two isotopes can be determined with an accuracy of ≤ 1.2 %.

The detector will be used for nuclear astrophysics to investigate the origin of the heavy elements in the slow neutron capture process.

CONTENTS

1 INTRODUCTION 1

2 DESIGN STUDIES FOR A NEUTRON CAPTURE DETECTOR

2.1 Basic requirements 3

2.2 Detector material 7

2.3 Design studies and Monte Carlo simulations 8

2.4 Shielding of scattered neutrons 19

3 DESIGN OF THE KARLSRUHE 4π BARIUM FLUORIDE DETECTOR

3.1 Detector geometry 21

3.2 Mechanical setup 22

4 THE INDIVIDUAL DETECTOR MODULES

4.1 Crystal handling 30

4.2 Reflector, photomultiplier, and voltage divider 30

4.3 Pulse shape 32

4.4 Energy and time resolution 35

4.5 Linearity 37

4.6 Background 37

4.7 Long term stability 40

5 DETECTOR ELECTRONICS

5.1 General aspects 43

5.2 Signal processing 44

5.3 Control electronics 50

5.4 Electronics for data acquisition 51

6 SETTING, CONTROL, AND STABILIZATION OF THE 4π DETECTOR

6.1 Setting of individual parameters 53

6.2 Automatic adjustment and gain stabilization 53

7 PERFORMANCE OF THE 4π DETECTOR

7.1 Energy resolution 57

7.2 Detector efficiency 59

7.3 Time resolution 61

7.4 Stability 64

8 REGISTRATION OF NEUTRON CAPTURE EVENTS

8.1 Neutron source 65

8.2 Measurements and data evaluation 66

9 CONCLUSIONS

9.1 Improvements 76

9.2 Summary 77

10 REFERENCES 78

11 APPENDICES

11.A A FORTRAN code for Monte Carlo simulation of neutron scattering from the capture sample 81

11.B Tables of coordinates for a spherical shell of 12 pentagons and 30 hexagons 100

11.C Mechanical construction 105

12 ACKNOWLEDGEMENTS 115

1 INTRODUCTION

One of the main topics of nuclear astrophysics is the origin of the chemical elements and of their isotopes [1,2,3]. It is generally accepted that only the lightest nuclei are produced in the big bang , i.e. H, He and small amounts of Li. All other elements are built up in stars. While elements lighter than iron ($Z < 26$) are produced in fusion reactions, all heavier elements from zink up to uranium can only be synthesized by successive neutron capture reactions.

According to the time scale for neutron capture, two nucleosynthesis processes can be distinguished. The slow neutron capture process (s-process) occurring at a neutron density of some 10^8 cm^{-3} is characterized by time intervals of 1 to 10 y between successive capture events. The rapid neutron capture process (r-process) is realized in szenarios with much higher neutron densities of $>10^{20}$ cm^{-3} leading to capture times of the order of milliseconds.

For any quantitative s-process model the neutron capture cross sections of the involved isotopes are the most important input data [4]. Due to the comparably long time scale, the nuclei synthesized in the s-process are located in the valley of β-stability, and are thus accessible to laboratory experiments. As the s-process occurs in stars during helium burning (i.e. during the late stages of stellar evolution) at typical temperatures of 200 - 300 million K, the corresponding neutron spectrum represents a Maxwell-Boltzmann distribution with a thermal energy around $kT = 25$ keV. Hence, experimental determinations of the relevant capture cross section have to cover the energy range up to 200 keV.

Many investigations during the last years showed [4] that the accuracy of 5-10 % that can be achieved for the neutron capture cross sections with established techniques is not sufficient to constrain the physical conditions during the s-process reliably. This would require an accuracy of the order of 0.5 to 1%. In that context, it is sufficient to know the neutron capture cross section ratio relative to the standard cross section of gold with that precision. Therefore, it was our aim to implement a new and precise technique for the determination of neutron capture cross sections in the neutron energy range from 5 to 200 keV.

Detailed design studies resulted in a 4π BaF_2 detector with about 100% efficiency for gamma-rays in the energy range up to 10 MeV. It is the first spherical symmetric 4π detector made from this material, which shows outstanding features for gamma-ray detection [5]. The Karlsruhe 4π detector is the second approach of a large BaF_2 array after the Crystal Castle [6] that was constructed for investigating heavy ion reactions and has a geometry symmetric to the horizontal plane.

The detector consists of 42 crystals shaped as hexagonal or pentagonal truncated pyramids forming a spherical shell with 10cm inner radius and 15 cm thickness. The spectrometer is a versatile instrument not only suited for neutron capture cross section measurements. It allows for the simultaneous determination of gamma-ray multiplicities, angular distributions, and gamma-ray spectra. In connection with the 3 MV Van de Graaff accelerator, the experimental setup can also be used to measure (p,γ) and (α,γ) reactions, which are of interest for the nucleosynthesis of light elements. If used as a multiplicity spectrometer, the determination of the fission to capture cross section ratio of actinide isotopes, which is of importance for reactor applications is also possible.

The first attempt to measure neutron capture events with a 4π detector of good energy resolution and high efficiency was made by Muradyan et al. [7]. However, the use of NaI(Tl) as detector material did not allow for very accurate measurements in the keV neutron energy range (§ 2.2). The same holds for a significantly smaller spectrometer described by Block et al. [8]. Both instruments are well suited for measurements below 1 keV neutron energy, where the detector can easily be shielded from scattered neutrons. BGO as detector material was used by Yamamoto et al. [9]; however, their design is simpler and less efficient, and hence not suited for the accuracy aimed at in our approach. Presently, a 4π BaF_2 detector is under construction at the LANSCE facility in Los Alamos [10] . It has about the same efficiency as the Karlsruhe detector, but an important feature of the present setup is lost: because the scintillator is immediately surrounding the sample, it does not allow for the discrimination of background due to sample scattered neutrons by time of flight (§ 2.3).

The first proposal for the present detector was still based on BGO as scintillator [11]. The gamma-ray efficiency of a spherical shell of BaF_2 and BGO for monoenergetic gamma-rays and neutron capture cascades has been calculated by Wisshak et al. [12]. The properties of large BaF_2 crystals for the detection of energetic photons and the first tests of prototype modules for the present design are documented in refs. [13, 14, 15].

In the present paper we summarize in § 2 the basic requirements, which have to be met by a detector for the precise determination of neutron capture cross sections as well as the corresponding design studies. The mechanical construction of the 4π detector and the features of the individual detector modules are given in §§ 3 and 4. The subsequent §§ 5 and 6 describe the electronics, and the detector operation, while the detector performance is presented in § 7. Finally, first results from neutron capture measurements are discussed in § 8, and further improvements are considered in § 9.

2 DESIGN STUDIES FOR A NEUTRON CAPTURE DETECTOR

2.1 BASIC REQUIREMENTS

The unambiguous registration of a neutron capture reaction, which is required for the accurate determination of the cross section is hampered by the fact that there is a more complex signature in the exit channel as, e.g. in (n,p) or (n,α) reactions. Neutron capture events are characterized by a cascade of prompt gamma-rays. The multiplicity and the energies of the individual gamma quanta are determined by the transition probabilities to a great variety of accessible nuclear levels. The only fixed quantity is the sum energy of the cascade that corresponds to the binding energy of the captured neutron (6–8 MeV for most of the isotopes of interest for s-process studies) increased by the kinetic energy of the captured neutron. For isotopes with Z larger than ~26, the level density at excitation energies of several MeV is so large that the capture cross section is composed of contributions from many possible cascades as indicated schematically in fig. 1. According to statistical model calculations for neutron captures in gold [16], more than 4000 possible cascades have to be considered in order to cover 95 % of the cross section. For medium weight isotopes like ^{56}Fe, the respective number is still 300 [12,17]. The average gamma-ray multiplicity of the cascades is 3–4 with maximum values up to 10.

Therefore, the essential requirements of an improved detector for neutron capture cross section measurements are the following:

(i) Efficiency of about 100 % for gamma-ray energies up to 10 MeV.

(ii) Good energy resolution (10 % at 1 MeV).

(iii) Good time resolution ($\Delta t = 1$ ns).

(iv) Low sensitivity for the detection of neutrons scattered into the detector material.

The first feature guarantees that all gamma-rays of the capture cascade are registered in the detector; their sum corresponds to the total gamma-ray energy, which is the only true signature of a capture event. This feature is also important as it makes the detector efficiency independent of gamma-ray multiplicity.

If the second requirement can be realized simultaneously, the capture events show up in the sum energy spectrum as a sharp line indicated schematically in fig. 1. Hence, they appear well separated from the expected gamma-ray background at low energies, resulting in favorable signal to background ratios. A good time resolution is essential as the energy of the captured neutron has to be determined by the time of flight (TOF) technique. In the present application, it is also useful for the TOF discrimination of background due to sample scattered neutrons (§ 2.3).

The last requirement is of key importance for the neutron energy range above ~1 keV, where the cross sections for neutron scattering are typically 10 to 100 times larger than for capture. If these scattered neutrons are captured in the detector material, it is very difficult to distinguish this background from true capture events in the sample.

Historically, the first approach to measure neutron capture cross sections by the TOF technique was to use large liquid scintillator tanks for the detection of capture gamma-rays [18,19]. The main disadvantage of these detectors is their poor energy resolution, which does not allow to separate capture events sufficiently well from the background due to the 2.2 MeV gamma-ray line from neutron captures in the hydrogen of the scintillator. In addition, the 60 % efficiency of a 800 l tank for gamma-rays of 6 MeV is too low to ensure that the detection of a capture cascade does not depend on the multiplicity. As these problems cause systematic uncertainties of about 10 %, this method was abandoned some ten years ago.

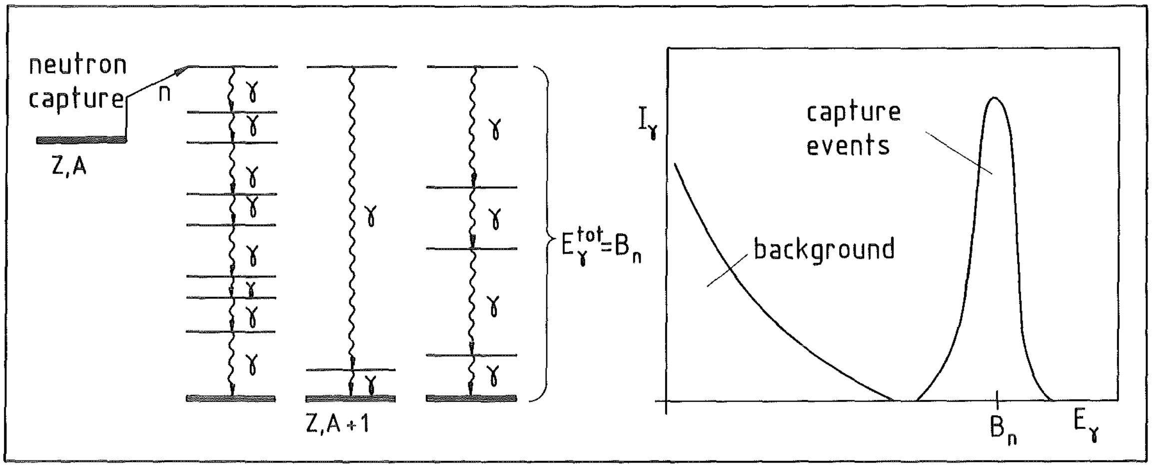

Fig. 1 Left: The excited states in the compound nucleus that are populated by neutron capture can decay via many different gamma-ray cascades.
Right: A 4π detector with 100 % efficiency adds these cascades in an isolated line at the binding energy of the captured neutron, well separated from most of the background.

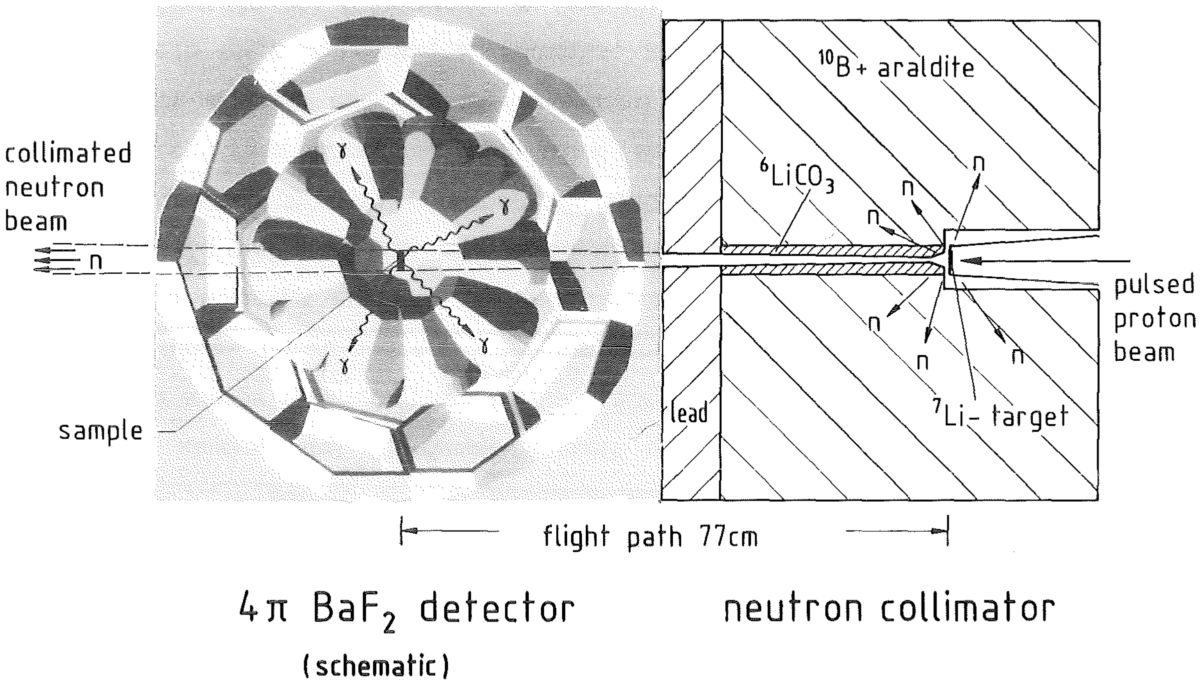

Fig. 2 Schematic setup of the Karlsruhe 4π BaF_2 detector for the determination of neutron capture cross sections in the energy range from 5 to 200 keV.

A completely different approach was introduced by Moxon and Rae [20]; the absolute efficiency of their detector is small, but increases linearly with gamma-ray energy. The combination of these features yields a detection probability for capture events independent of gamma-ray multiplicity. The efficiency for a capture cascade is given as the sum over the individual cascade gamma-rays

$$\varepsilon_{capt} = \sum \varepsilon(E_\gamma) = \sum k E_\gamma = k E_{\gamma,tot}$$

and is thus proportional to the total gamma-ray energy after averaging over a sufficient number of events. Obviously, the detection probability for a cascade of 6 gamma-rays of 1 MeV is the same as for a single gamma-ray of 6 MeV provided that gamma-rays of the first cascade are not detected simultaneously. The main disadvantage of this method is the low efficiency of about 1% at 1 MeV. In practice, there are also deviations from the ideal shape of the efficiency causing systematic uncertainties of 3 – 10 % depending on the capture gamma-ray spectrum [17,21].

The third method, which was most widely used in the last years [22,23] takes an intermediate position between the two extremes described above. A hydrogen-free liquid scintillator like C_6D_6 or C_6F_6 of about 1 l volume is used for the detection of capture gamma-rays. It combines an efficiency of about 20% for capture cascades with a very low sensitivity to capture of scattered neutrons. For these detectors, a linear increase of the efficiency with gamma-ray energy can only be achieved by means of a so called weighting function: each measured pulse height is multiplied with the corresponding value of the weighting function, such that the inherent efficiency is properly corrected. Traditionally, the weighting function was calculated by considering the response of the scintillator for gamma-rays, but also the influence of detector canning, sample and all surrounding materials of the experimental setup. Recently, the weighting function was determined experimentally [24], showing severe discrepancies to previous calculations at high gamma energies. This implies that the detection of energetic Compton electrons produced outside of the scintillator were probably not correctly treated in the earlier calculations, and may explain large discrepancies in experimental results obtained with different setups [21, 25, 26]. This problem being often not sufficiently considered, casts some doubt on the optimistic uncertainties, that are sometimes claimed for cross sections determined with this method.

In summary, the existing experimental techniques are not suited for obtaining the accuracy required in analyses of the astrophysical s-process. The present approach returns to the old concept of 100% efficiency for all gamma-rays, but replacing the liquid scintillator by scintillator crystals with good energy resolution. This became possible with the advent of scintillators showing low sensitivity to capture of scattered neutrons.

The design criteria for the new 4π BaF_2 detector are closely related to the experimental conditions at Karlsruhe. Accordingly, fig. 2 shows the schematic setup for measurements using a Van de Graaff accelerator. Neutrons are produced via the $^7Li(p,n)^7Be$ reaction with a pulsed proton beam of 250 kHz repetition rate and 0.7 ns pulse width. At proton energies of ~2 MeV, continuous neutron spectra in the required energy range from 5 to 200 keV are obtained. A well collimated neutron beam is produced by a carefully designed shield around the lithium target, and hits the sample in the center of the capture gamma-ray detector at a flight path of about 1 m. The complete gamma-ray cascade is registered in the detector, and the energy of the captured neutron is determined via TOF (typically 100-500 ns depending on neutron energy).

The main sources of background in such an experiment are the following:

(i) Time independent gamma-rays from natural radioactivity of the scintillator crystal, surrounding materials, cosmic-rays, etc;
(ii) Time dependent and time independent background produced by fast and moderated neutrons escaping from the shielding;
(iii) Time dependent background caused by neutrons scattered in the sample and captured in the scintillator or nearby.

The first two components can be minimized by the design of collimator and shielding, whereas the third one depends on the scintillator and canning materials.

2.2 DETECTOR MATERIAL

Application of the four criteria listed in § 2.1 to those scintillator crystals that are available in appropriate sizes for the 4π detector, i.e. to NaI(Tl), BGO, CsI(Tl) and BaF_2 rules out all materials containing iodine as ^{127}I has a large neutron capture cross section of 635 mb at 30 keV [27]. Consequently, scattered neutrons are immediately captured in the scintillator material, giving rise to unacceptable backgrounds. In the energy range of interest, shielding the detector from scattered neutrons would require thick layers of ^{10}B, ^{6}Li and H (see § 2.4), which in turn would degrade the capture gamma-ray spectrum significantly, thus destroying the advantage of the good energy resolution. Below ~1 keV neutron energy, however, a thin layer of ^{10}B is sufficient to absorb scattered neutrons, and therefore NaI(Tl) can be used as suggested in refs. [7,8].

Compared to NaI(Tl), BaF_2 and BGO are significantly less sensitive to keV neutrons. The neutron magic isotope ^{138}Ba makes up for 72 % of the natural barium abundance; due to its small capture cross section of 3.9 mb at 30 keV [27] the elemental barium cross section is only 50 mb. The respective value for the monotopic element Bi is 11 mb, while the elemental cross section for germanium is 76 mb. The neutron sensitivity of the detector materials can roughly be estimated as the product of the thickness in molecules per cm^2 of a spherical shell with comparable efficiency and the capture cross section at 30 keV. For the scintillator materials NaI(Tl), BaF_2, and BGO it scales as 15 : 1 : 0.6, suggesting BGO to be the best choice. However, the binding energies of ^{135}Ba and ^{137}Ba are 9.1 and 8.6 MeV, with both isotopes accounting for 75 % of the elemental capture cross section, whereas the respective values for the even germanium isotopes range between 6.5 and 7.4 MeV, contributing 85 %. As most of the isotopes of interest for nuclear astrophysics have binding energies between 6 and 8 MeV a significant fraction of this background can be discriminated in BaF_2 detectors by an upper threshold in the sum energy (see § 8). In this way, the neutron background in an actual experiment will be lower for BaF_2 .

Other important aspects in favor of BaF_2 compared to BGO are the superior resolution in gamma-ray energy and, especially, in time. In energy resolution, the difference for large crystals is about a factor of two [14, 28, 29, 30], while the time resolution is at least four times better [14, 31]. The only drawback of BaF_2 crystals is the unavoidable contamination with radium, the chemically homologous element to barium, which causes a relatively high time independent background (§ 4.6)

2.3 DESIGN STUDIES AND MONTE CARLO SIMULATIONS

The two most important features of a 4π detector for the detection of neutron capture events, the efficiency for neutron capture cascades and the background due to sample scattered neutrons, have been simulated on the computer.

The efficiency of a spherical shell of BGO or BaF_2 for monoenergetic gamma-rays in the energy range up to 10 MeV has been calculated by Schatz and Oehlschläger [32] using analytical methods. Capture cascades for neutron capture in ^{56}Fe, ^{197}Au, and ^{241}Am, three isotopes with widely different capture gamma-ray spectra, have been calculated previously with the statistical and optical model [16, 17, 33]. The combination of both informations allows to determine the pulse height spectra for the expected sum energies of the respective capture reactions [12]. The essential results are plotted in fig. 3 showing the shape of the capture gamma-ray spectra, and in fig. 4, where the corresponding sum energy spectra are displayed for a spherical shell of BaF_2 with 10 cm inner radius and 15 cm thickness. One finds that roughly 95 % of the capture events are registered with a sum energy of more than 2.5 MeV. For the cross section ratios $\sigma(Fe)/\sigma(Au)$ or $\sigma(Am)/\sigma(Au)$, the correction due to differences in efficiency is of the order of only 1 %, with the respective systematic uncertainties being well below 0.5 %. This holds the more for measurements on neighboring isotopes, e.g. for the important ratio $\sigma(^{148}Sm)/\sigma(^{150}Sm)$, where only small differences in the shapes of the two gamma-ray spectra are expected.

The background due to neutrons scattered from the sample in the centre of the detector was determined by Monte Carlo calculations; the code (appendix A) follows each neutron until it is either captured in the scintillator or it escapes from the detector. For each possibility the time since emission from the sample, the number of scattering interactions, and the final neutron energy were calculated. For neutron captures, the respective position in the scintillator (radius from the centre) was stored as well. The capture and scattering cross sections of up to three materials were used as input to determine the respective reaction probabilities. For scattering events, the scattering angles were randomly selected according to the angular distributions, and the respective energy losses were considered. In this way, the neutrons were followed for up to 100 interactions. If the randomly selected interaction point was located inside the inner sphere, the next interaction was transferred to the opposite part of the spherical shell following a straight line.

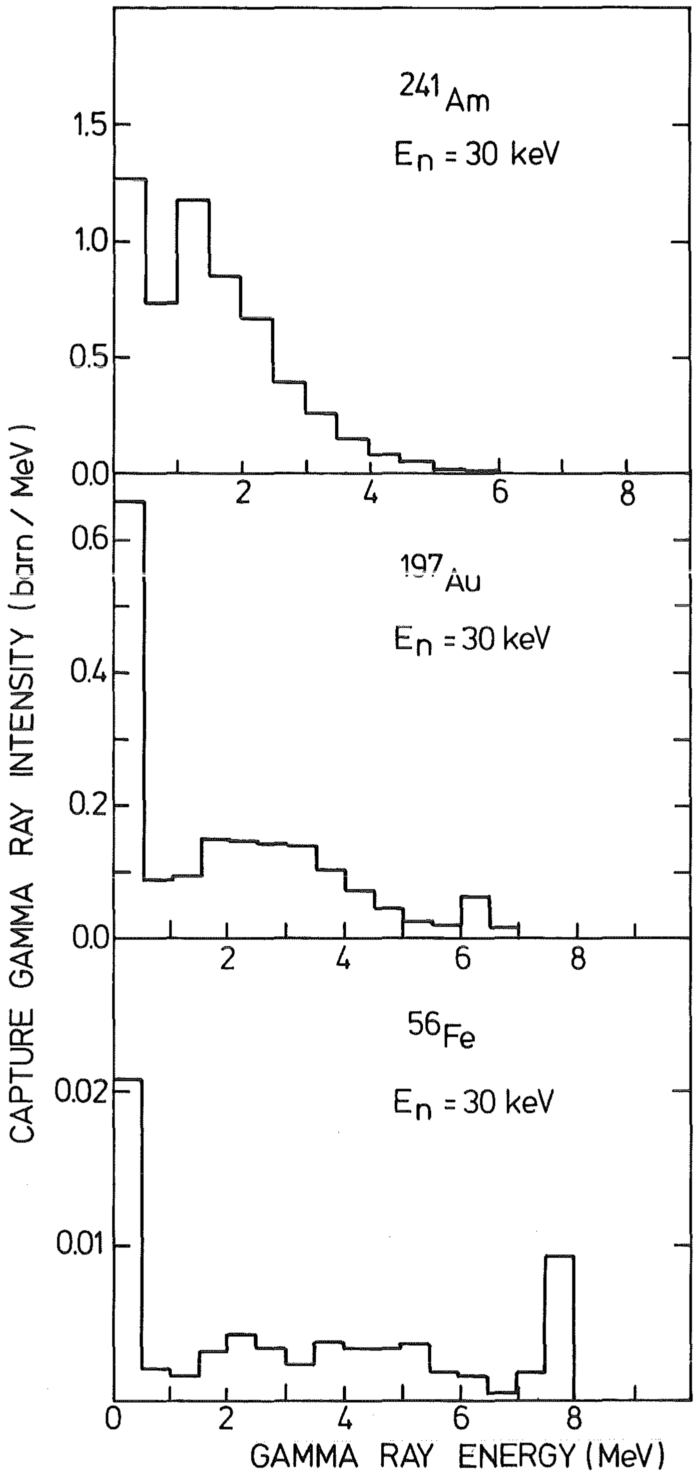

Fig. 3 Gamma-ray spectra calculated for neutron capture in ^{241}Am, ^{197}Au, and ^{56}Fe at a neutron energy of 30 keV [16,17].

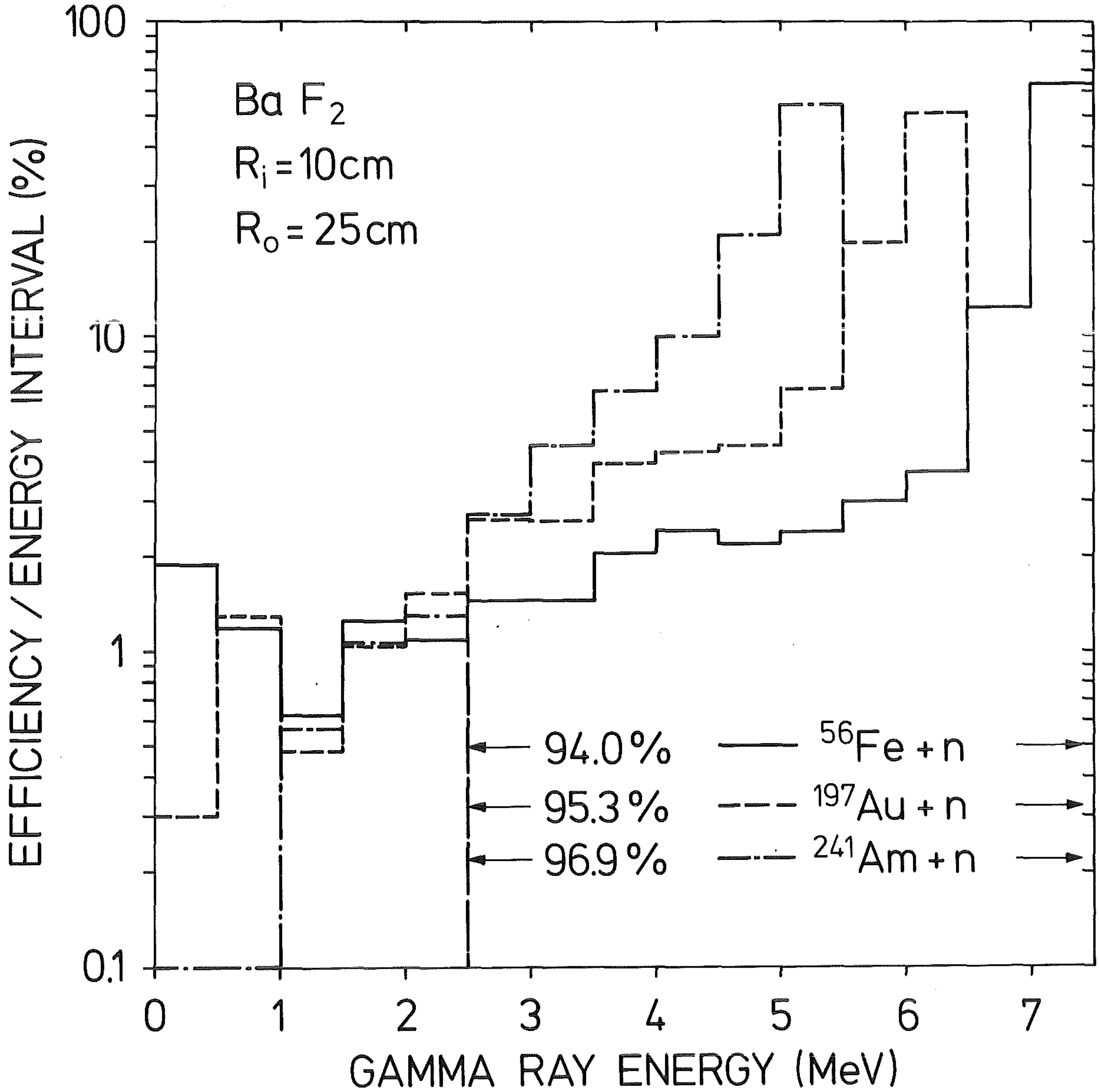

Fig. 4 Calculated pulse height spectra for neutron captures in ^{56}Fe, ^{197}Au, and ^{241}Am for a spherical shell of BaF_2 crystals (R_i = 10 cm, R_o = 25 cm).

Table 1. Capture and escape probabilities for neutrons emitted from the centre of spherical scintillator shells with about equal gamma-ray efficiency. The fourth column denotes the probability for hitting the sample again.

Initial neutron	Probability (%)			Average number of interactions		
energy (keV)	escape	capture	sample	escape	capture	sample
BaF_2 (inner radius 10 cm, thickness 15 cm)						
95	93.5	6.5	2.8	19.7	23.3	5.5
85	93.3	6.7	2.5	17.8	21.9	4.8
75	94.0	6.0	1.9	16.0	21.8	5.5
65	93.9	6.1	1.3	16.1	19.9	5.9
55	92.2	7.8	1.8	17.8	21.0	6.6
45	92.1	7.9	1.8	15.8	19.5	5.0
35	91.8	8.2	1.6	15.8	19.3	7.2
25	91.3	8.7	2.2	13.9	19.3	4.4
17.5	89.3	10.7	1.8	13.9	19.1	4.2
12.5	87.2	12.8	2.1	14.0	19.0	4.5
7.5	82.3	17.7	2.1	13.9	17.4	5.0
BGO (inner radius 10 cm, thickness 10 cm)						
95	95.7	4.3	2.0	17.1	26.5	6.7
85	95.3	4.7	2.4	17.5	25.1	6.4
75	94.9	5.1	1.8	17.3	26.9	6.4
65	94.9	5.1	2.3	17.6	27.0	6.1
55	93.8	6.2	2.3	18.0	26.9	6.4
45	93.5	6.5	2.0	18.2	25.8	7.4
35	92.5	7.5	2.2	18.6	27.2	7.0
25	90.6	9.4	2.0	19.0	25.6	7.6
17.5	89.5	10.5	2.0	19.6	26.9	8.5
12.5	85.7	14.3	3.0	23.1	28.2	7.0
7.5	84.5	15.5	2.0	18.9	24.3	6.5

Table 1 continued

Initial neutron energy (keV)	Probability (%) escape	capture	sample	Average number of interactions escape	capture	sample
NaI(Tl) (inner radius 10 cm, thickness 25 cm)						
95	59.3	40.7	1.5	9.5	9.3	3.2
85	56.6	43.4	1.5	9.5	9.2	2.9
75	53.7	46.3	1.5	9.7	8.9	2.9
65	51.5	48.5	1.0	9.4	8.9	3.3
55	43.3	56.7	2.2	11.2	9.3	2.7
45	46.0	54.0	1.5	8.6	7.7	2.7
35	41.5	58.5	1.5	8.3	7.4	2.8
25	35.3	64.7	1.4	8.0	7.4	3.2
17.5	28.9	71.1	2.0	8.0	7.0	2.8
12.5	22.6	77.4	1.4	7.7	7.5	2.8
7.5	11.9	88.1	1.5	10.9	10.2	3.4

The resulting time and energy spectra for captured and escaping neutrons were calculated as a function of the initial neutron energy, using the data of spherical shells of BaF_2, BGO, and NaI(Tl) as input. The probabilities for capture in or escape from the detector are compiled in table 1 for neutrons in the energy range from 5 to 100 keV. The fourth column in table 1 gives the probability that the neutron hits the sphere with 1 cm radius around the centre, showing that the chance for delayed capture events is very small. The dimensions of the detectors were such as to obtain about equal efficiency. The columns 5 to 7 present the respective average number of interactions in the scintillator. The probability for a neutron to escape from the scintillator shows little difference for BaF_2 (91 %) and BGO (92 %), while it is only 41 % for NaI(Tl). Note, that neutron captures in the first two materials occur on average only after 20 to 25 scattering interactions; this means that these events are strongly delayed in time with respect to the primary interactions. In NaI(Tl) neutrons are already captured after 8 interactions. The time and energy spectra for incident neutron energies of 100 and 25 keV and the number of scattering interactions are plotted in fig. 5 for the BaF_2 scintillator. The total number of Monte Carlo histories is 10000.

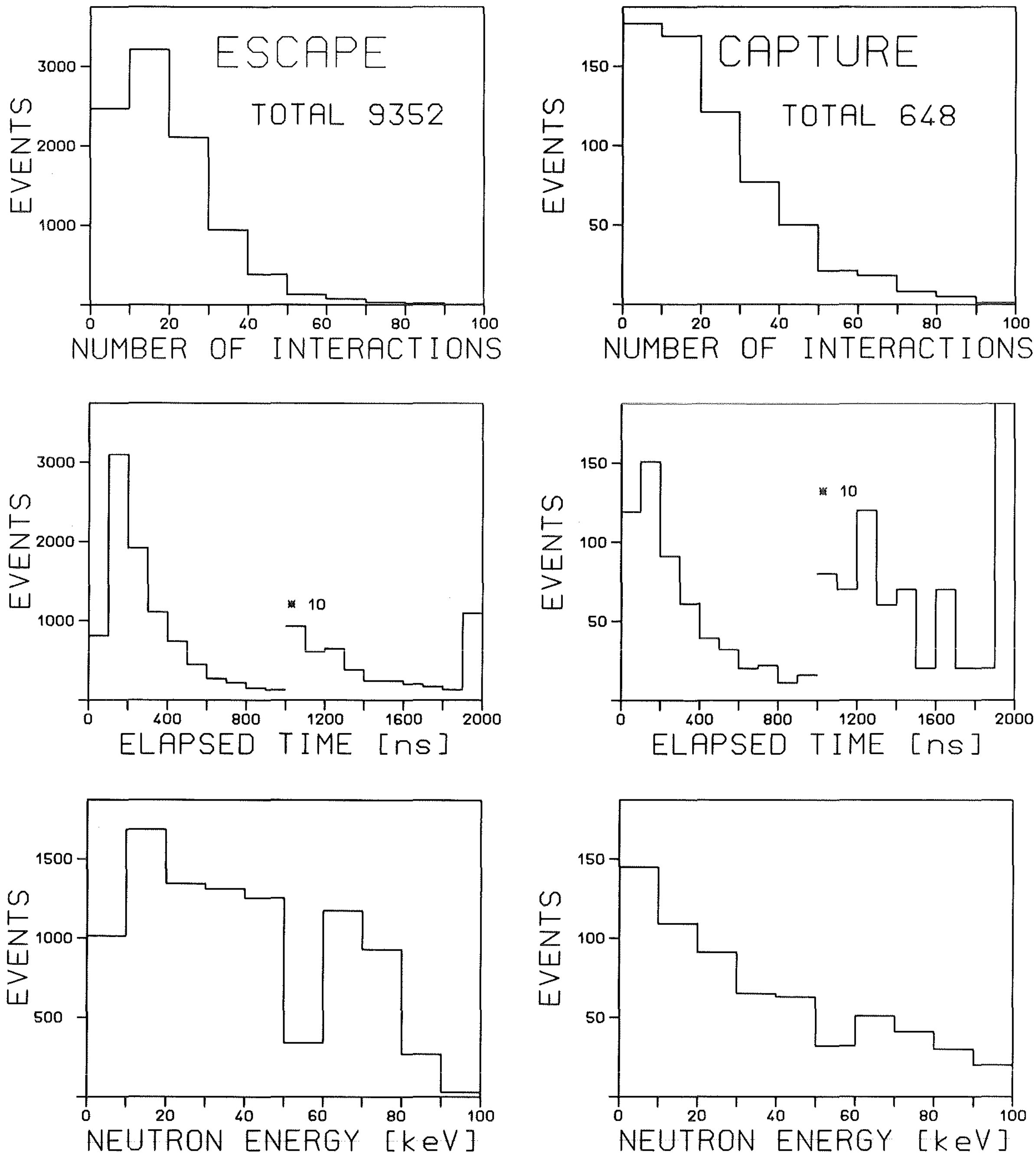

Fig. 5 a) Monte Carlo calculations of the energy and time distributions of neutrons escaping from or being captured in the spherical BaF_2 shell ($R_i = 10$ cm, $R_o = 25$ cm), assuming that 100 keV neutrons start at time zero from the centre. The number of interactions are shown on top.

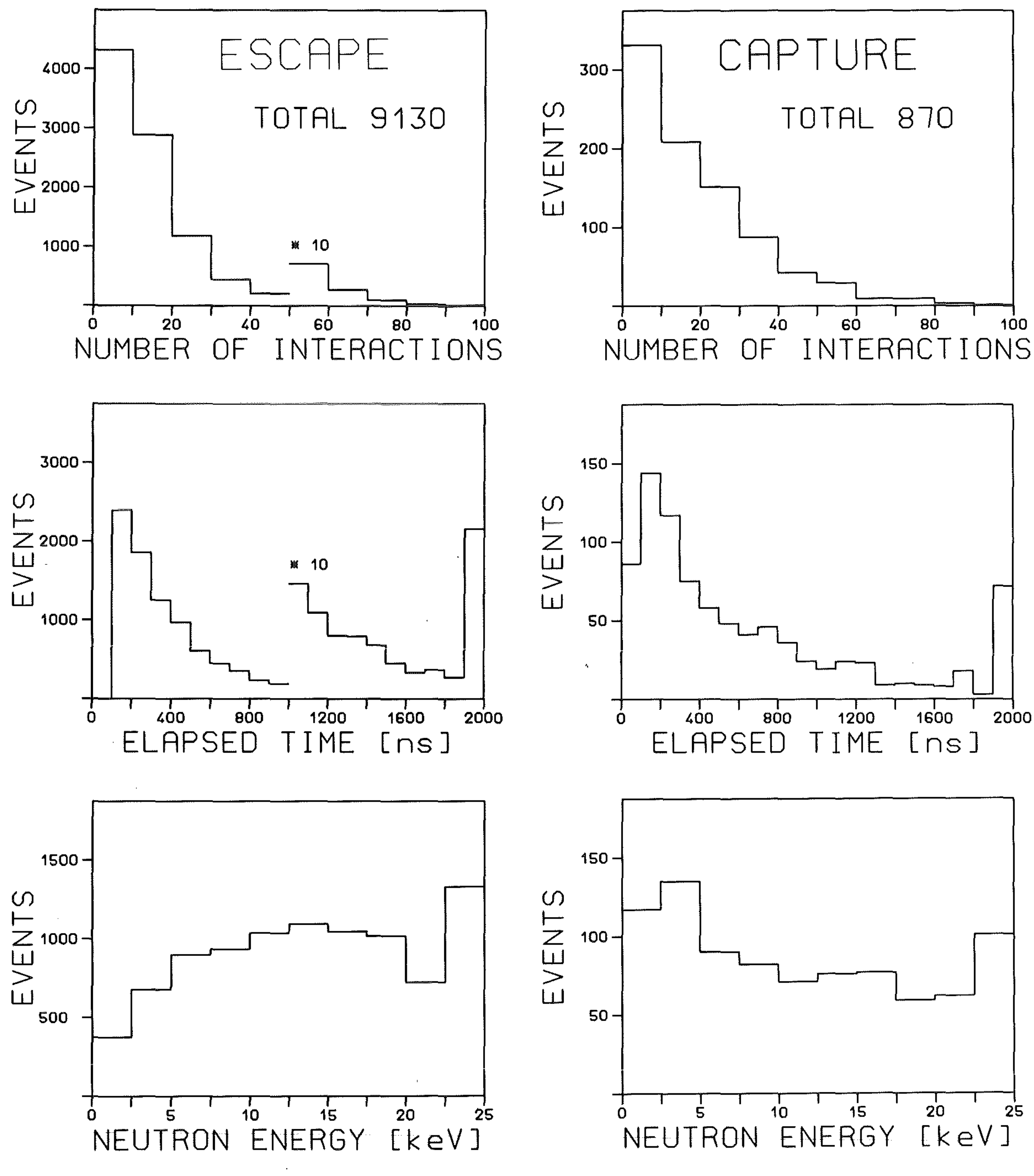

Fig. 5 b) as fig. 5.a, but for 25 keV neutrons.

The situation of an actual experiment is simulated according to the following assumptions:

(i) The shape of the neutron energy spectrum is that of the $^{7}Li(p,n)^{7}Be$ reaction at a proton energy 30 keV above threshold ranging from 5 to 100 keV (§ 8).

(ii) The capture cross section of the sample follows the 1/v law.

(iii) The scattering cross section is ten times larger than the capture cross section.

(iv) The primary flight path is 80 cm.

(v) The 4π detectors have 10 cm inner radius and about equal gamma- ray efficiency.

The result of this calculation is given in fig. 6, which compares the TOF spectra of the capture events in the sample with the background due to neutrons scattered in the sample and captured in the scintillator. While captures in the sample are concentrated in a time interval of about 200 ns, events due to capture of scattered neutrons are spread out in time over more than 2 µs. Therefore, the pulse repetition rate of the accelerator has to be smaller than 500 kHz to ensure that all neutrons of the previous pulse have escaped the scintillator or are captured (§ 8). Then, most of the related background falls outside the time interval used for data evaluation.

In case of BaF_2 and BGO the number of true capture events is slightly larger than the total number of background events. This confirms again the >90% escape probability for the scattered neutrons that compensates for the ten times larger scattering cross section. Note also that there is a neutron energy interval from 100 to 60 keV, which is almost undisturbed by capture of sample scattered neutrons due to the additional 10 cm flightpath between sample and the inner radius of the spherical shell. This region of optimum signal to background ratio will be important for the normalization of the cross section (§ 8). The results for NaI(Tl) show a much larger background due to the capture cross section of iodine. As the binding energy of iodine is 6.8 MeV and thus very close to the isotopes to be investigated, there is no chance to reduce this background by cuts in the sum energy spectrum (see below).

As an additional information, the radial distribution of neutron captures in the BaF_2 scintillator was determined for the first 200 ns after scattering in the sample. The results are plotted in fig. 7 for three neutron energies. As most of these events are

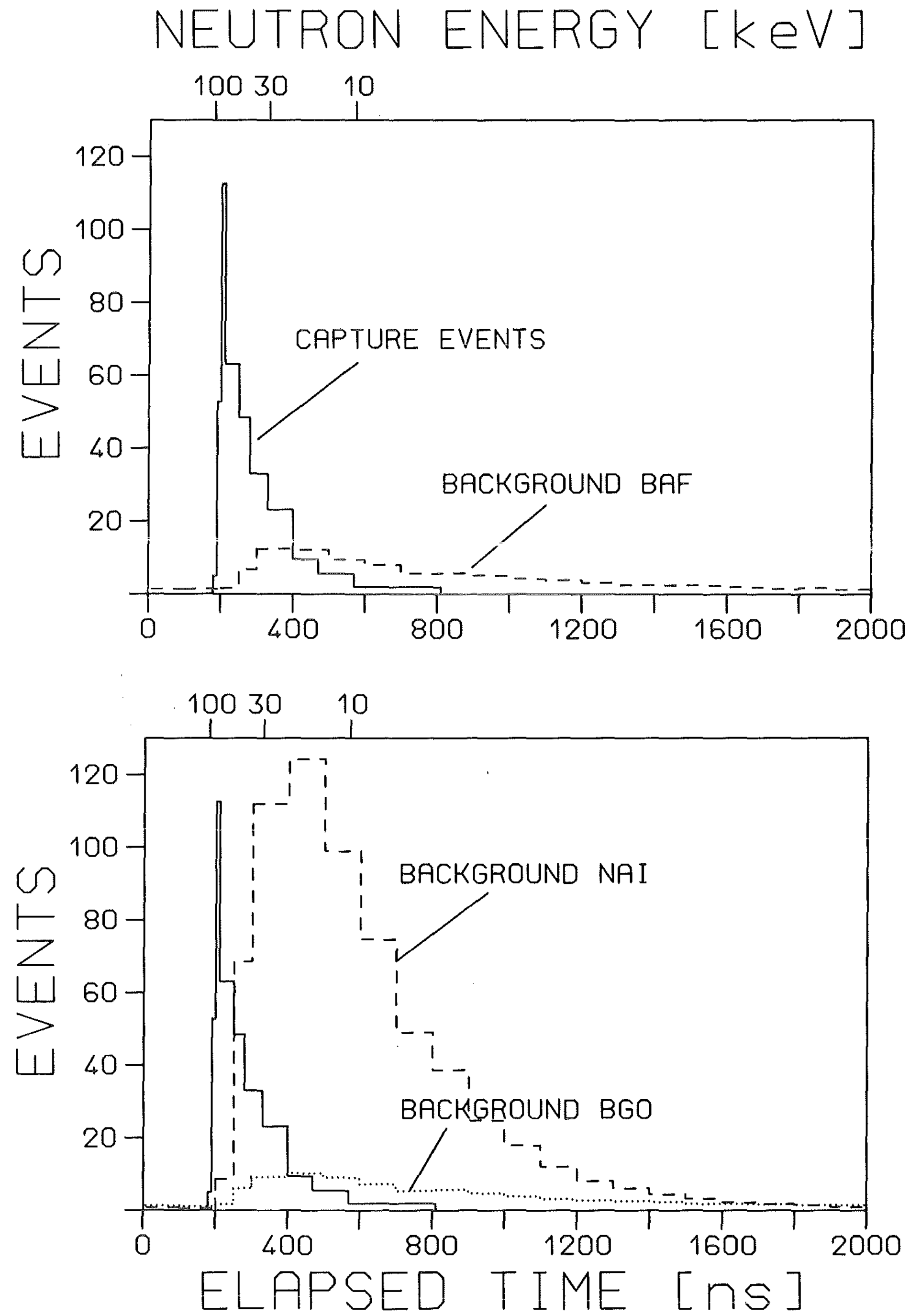

Fig. 6 Time distribution of capture events and background due to sample scattered neutrons, calculated for a neutron spectrum with 100 keV maximum energy, a flight path of 80 cm, a capture to scattering ratio of 1:10. The data are given for scintillator shells of about equal gamma-ray efficiency.

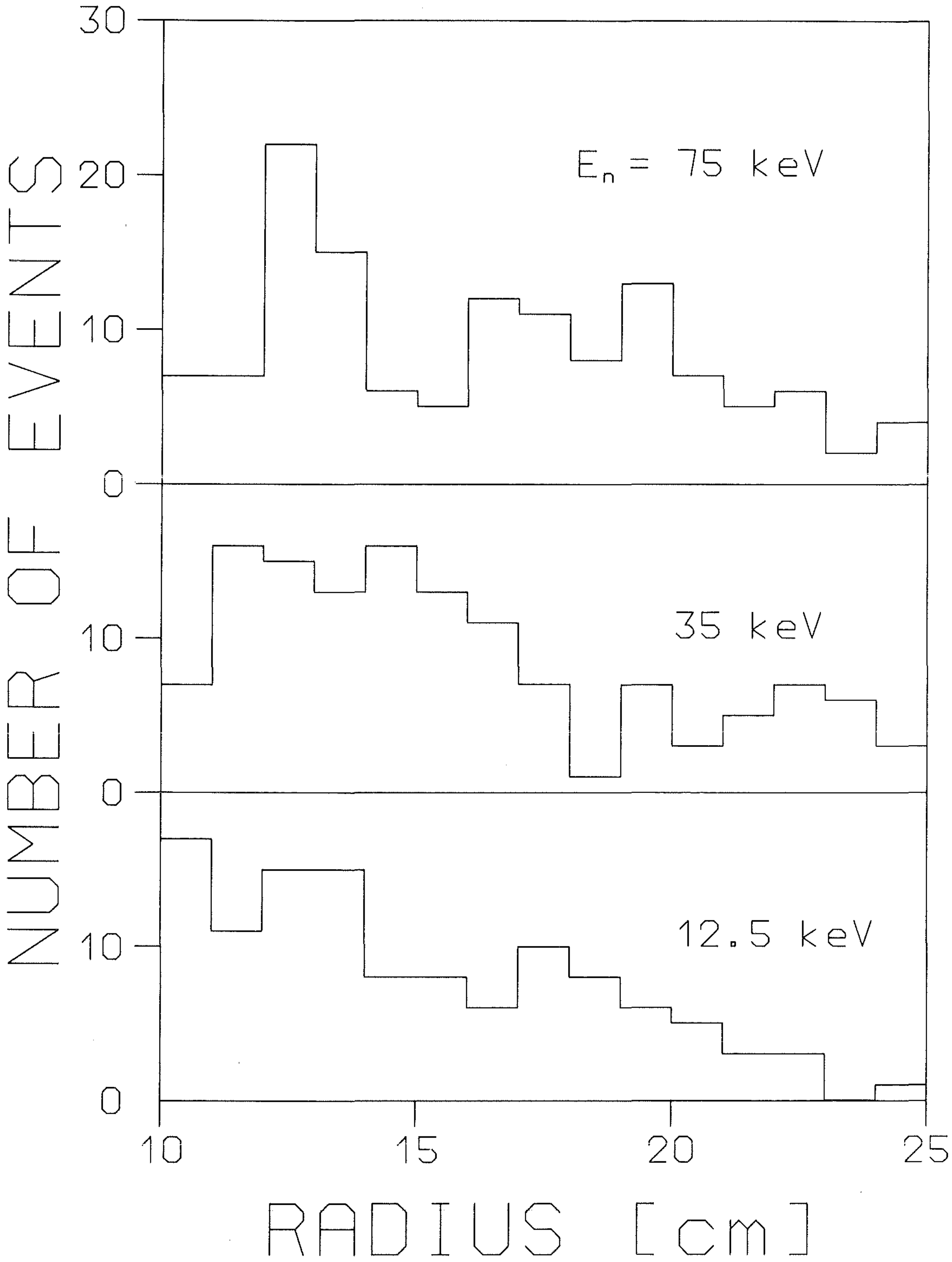

Fig. 7 Radial distribution of capture events in a spherical shell of BaF_2 caused by neutrons starting with different energies from the centre.

concentrated near the inner surface of the detector, there is a high probability for observing the full capture cascade. This offers the possibility to discriminate these events by selecting appropriate energy windows in the sum energy spectra if the binding energy of the measured isotope differs from that of ^{135}Ba and ^{137}Ba (§ 8).

The above calculations clearly reveal two restrictions for the suggested experimental setup:

(i) NaI(Tl) cannot be used as detector material for accurate measurements of neutron capture cross sections in the keV range.

(ii) The TOF discrimination of background from sample scattered neutrons is lost if the primary flight path between neutron source and sample is much longer than the inner radius of the detector. For example, in LINAC experiments the minimum primary flightpath is 10 m. Correspondingly, the above neutron spectrum between 10 and 100 keV covers a time interval of 5 μs in the primary beam. This means that the additional time spread of 2 μs for the sample scattered events does no longer allow to discriminate this type of background; the background spectrum has the same shape and the same size as the measured effect, resulting in a signal to background ratio of unity. The present design is therefore particularly suited for the short flight paths of Van de Graaff experiments.

2.4 SHIELDING OF SCATTERED NEUTRONS

The Monte Carlo code described above can also be used to calculate the effect of a neutron shield around the sample, if the cross sections for the scintillator are replaced by the respective values for the shielding materials. Efficient shieldings can be constructed using mixtures of boron and hydrogen in the atomic ratios 1:1 or 1:2. Calculations were made for $B_{10}H_{14}$ assuming 100% enrichment in ^{10}B (and neglecting that this compound is an explosive). The results for a spherical shell with 2 and 4 cm thickness are compiled in table 2. Even a thickness of 4 cm is found to reduce the flux at 100 keV only by a factor of 10. These results confirm again that NaI(Tl) is not a suited scintillator for the present setup even with the best shielding against scattered neutrons. Apart from the fact that the neutron flux at 100 keV is not sufficiently reduced, such shieldings around the sample are severely degrading the gamma-ray spectra by Compton scattering and cannot be used for this reason as well.

Table 2. Capture and escape probabilities for neutrons emitted from the centre of a spherical $B_{10}H_{14}$ shell enriched to 100% in ^{10}B. The fourth column denotes the probability for hitting the sample again.

Initial neutron energy (keV)	Probability (%) escape	capture	sample	Average number of interactions escape	capture	sample
$B_{10}H_{14}$ (inner radius 6 cm, thickness 4 cm)						
100	10.7	89.3	0.3	3.6	4.2	2.6
90	9.5	90.5	0.4	3.8	4.1	2.5
80	8.8	91.2	0.4	3.8	4.1	2.6
70	7.2	92.8	0.3	3.9	4.1	2.9
60	7.1	92.9	0.3	3.8	4.0	2.7
50	6.0	94.0	0.3	3.9	3.9	2.2
40	4.3	95.7	0.3	4.0	3.8	2.7
30	3.6	96.4	0.3	3.9	3.6	3.1
20	2.8	97.2	0.1	4.2	3.5	2.6
10	1.3	98.7	0.2	3.6	3.1	2.5
$B_{10}H_{14}$ (inner radius 8 cm, thickness 2 cm)						
100	40.0	60.0	0.4	2.5	3.7	2.5
90	37.1	62.9	0.2	2.6	3.7	2.9
80	35.5	64.5	0.2	2.6	3.7	2.7
70	34.6	65.4	0.3	2.7	3.6	2.6
60	32.9	67.1	0.2	2.7	3.6	3.0
50	29.6	70.4	0.2	2.7	3.5	2.4
40	26.2	73.8	0.1	2.8	3.4	3.7
30	23.0	77.0	0.2	2.8	3.3	2.6
20	21.3	78.7	0.2	2.8	3.2	2.8
10	15.3	84.7	0.1	2.7	2.9	2.8

3 DESIGN OF THE KARLSRUHE 4π BARIUM FLUORIDE DETECTOR

3.1 DETECTOR GEOMETRY

For the design of the detector geometry the following aspects have been considered:

(i) Maximum efficiency for capture gamma-rays with minimum scintillator volume.

(ii) The efficiency for gamma-rays should be sufficient to register 95 % of the capture events above a threshold energy of 2.5 MeV in the sum energy spectrum.

(iii) The distance between sample and scintillator should be as large as possible for optimum TOF discrimination of events due to sample scattered neutrons.

(iv) To minimize the number of modules, the detector should be built from the largest commercially available BaF_2 crystals; at the time of ordering these were rough crystals of 14 cm diameter and 17.5 cm length.

The first item stands for a maximum signal to background ratio with respect to background caused by natural radioactivity in the scintillator and its environment, as well as by moderated neutrons escaping from the collimator. The second feature can be satisfied by a BaF_2 thickness of 15 cm according to ref. [12]. The contradictory points (i) and (iii) were compromised by choosing an inner radius of 10 cm for the spherical shell. Then, the scintillator volume is about 60 l, four times larger than the minimum value for zero inner radius. On the other hand, an inner radius of 10 cm together with the minimum flightpath of 77 cm (§ 8) offers a sufficiently wide region in the TOF spectra free of events from scattered neutrons; this last feature is important for the success of the proposed method (§§ 2, 8).

The problem of subdividing a spherical shell into individual crystals has previously been studied for the 4π NaI(Tl) detectors, e.g. the spin spectrometer [34] or the Heidelberg Crystal Ball [35]. Under the constraints of symmetry, ease of construction and minimum cross talk between individual detector modules it was shown that the class of optimum polyhedra always has 12 pentagons and a varying number of hexagons. The configurations can be derived from the classical regular polyhedrons by subdividing the triangle of the icosahedron or the five triangles forming the pentagon of the dodecahedron in an increasing number of new triangles, which are then recombined to pentagons and hexagons. This yields new polyhedra with discrete "magic" numbers of elements, i.e. 32, 42, 72, 92, 122, 132, 162 etc.

A detector for neutron cross section measurements should consist of as few elements as possible, in order to avoid losses in gaps. For the investigation of individual capture cascades and angular distributions, the granularity should be ~5 times larger than the expected average cascade multiplicity of 3 to 4 with only a small fraction being above 6. While an array of 32 elements would be sufficient in this respect, the next "magic" number 42 had to be chosen because of the limited size of the available BaF_2 crystals.

As shown in fig. 8, this configuration is constructed by dividing each of the five triangles forming the pentagon of the dodecahedron into four new triangles. The upper of these triangles together with its neighbors form the new pentagon, while the three lower ones are combined with the respective three of the next triangle to the new hexagon. The arc lengths of the hexagons and pentagons inscribing a touching sphere of unity radius are also given in fig. 8. These values were calculated with the boundary condition that both elements cover the same solid angle. The coordinades of the centres, corners and mid points of the edges of all 42 hexagons and pentagons forming the spherical supporting structure of the detector with 430 mm radius (§ 3.2) are given in Cartesian and polar coordinates in appendix B.

3.2 MECHANICAL SETUP

The final shape of the two types of BaF_2 crystals ordered from the manufacturer (Merck, Darmstadt, Fed. Rep. of Germany) is shown in fig. 9. (A more detailed drawing can be found in appendix C). Each crystal is cut from a cylindrical rough slug of 14 cm diameter and 15 cm thickness, so that at the base about 6 % of the truncated pyramids are not filled with BaF_2; this part is used for fixing the crystals in the supporting structure. The volume of the real crystals is compared in table 3 with the volume of perfect truncated pyramids. It is shown that the real volume is practically the same as that of the intended spherical shell with 10 cm inner radius and 15 cm thickness.

Each crystal is wrapped in a reflector and supplied with an own photomultiplier, thus representing an independent gamma-ray detector. The mechanical construction is illustrated in fig. 10. The crystal is fixed in a cylindrical glass fibre tube by a metal ring lock. The front end of this tube is shaped such as to use that volume of the

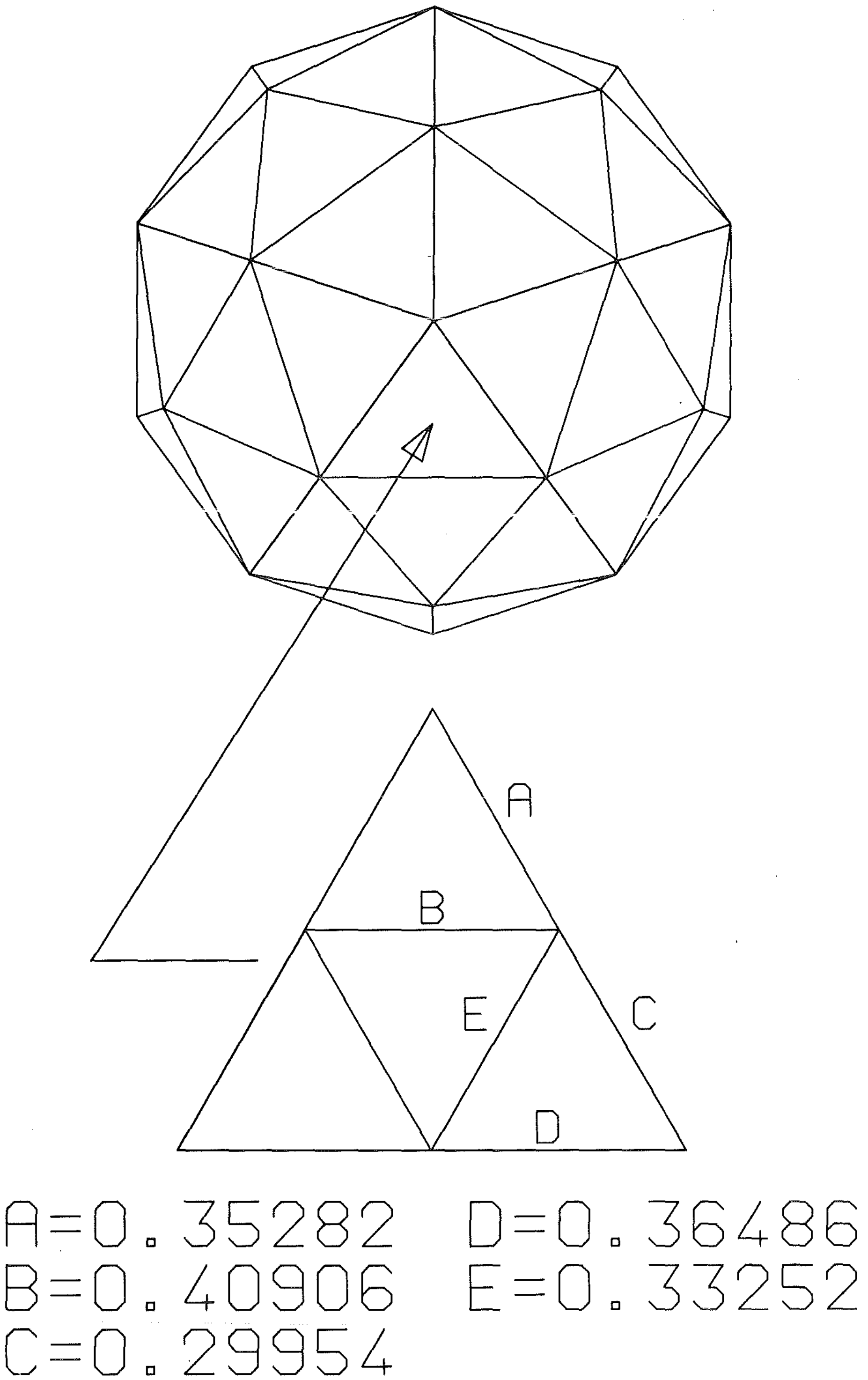

Fig. 8 Arclengths of hexagons and pentagons forming a polyhedron with 42 elements with an inscribed touching sphere of unit radius.

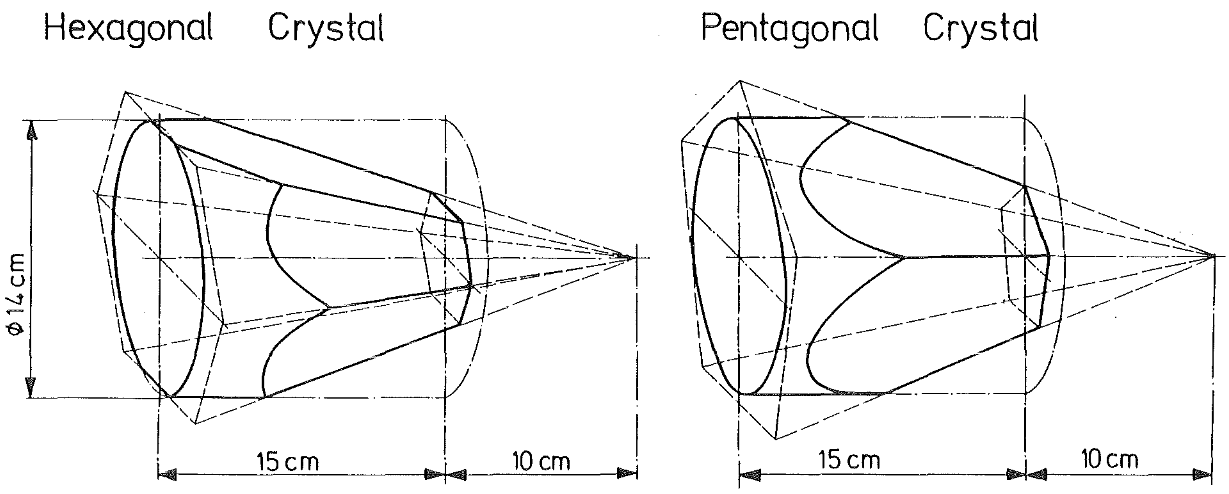

Fig. 9 Shape of the hexagonal and pentagonal BaF_2 crystals for the Karlsruhe 4π detector (for details see appendix B).

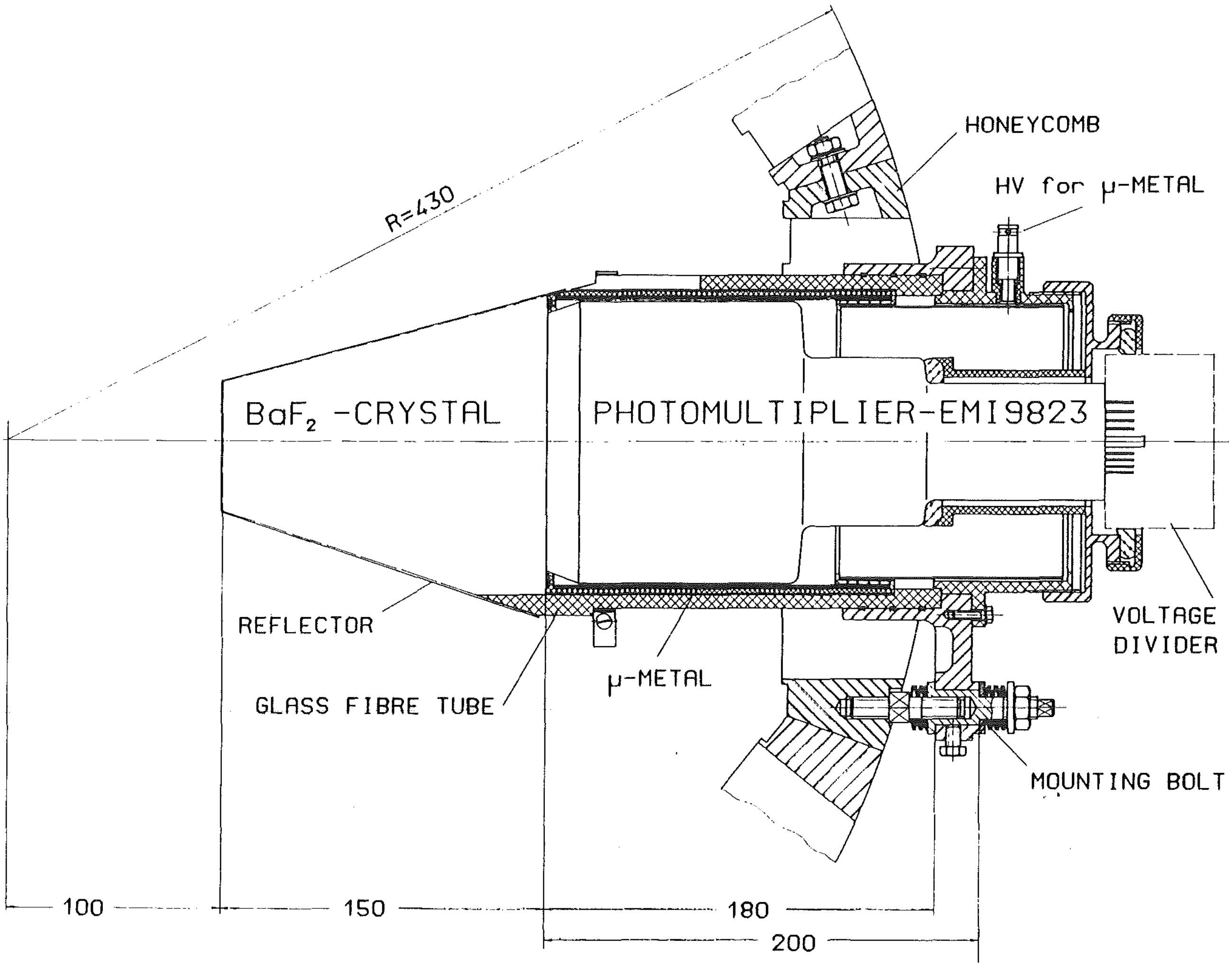

Fig. 10 Cut through one detector module and its mounting in the supporting structure.

truncated pyramid that is not covered by BaF_2 scintillator. The rear end of the tube is glued into a triangular aluminum flange, which is fixed and adjusted in the supporting honeycomb structure. The crystals are covered on all sides with a reflector for the scintillation light leaving only a circular hole of 12 cm diameter for connection of the photomultiplier.

The reflector consists of two layers of 0.1 mm thick unsintered PTFE tape followed by an 0.1 mm polished aluminum foil, and an outer layer of black tape. The photomultipliers (EMI 9823 QKA) are optically coupled to the crystal using silicon oil (Baisilone) with a viscosity of 500 000 cst. A rubber O-ring is used to prevent the silicon oil from creeping into the reflector. The photomultipliers are magnetically shielded by three layers of 0.1 mm thick μ-metal sheets; optionally this shield can be connected with the negative cathode potential to eliminate the influence of external electric fields. The cross hatched parts in fig. 10 are made from insulating synthetic material, while the hatched parts are from aluminum.

The individual detector modules are fixed in the spherical honeycomb structure consisting of aluminum frames by means of three bolts. A set of elastic springs on each side of the flange provides a flexible mounting. The bolts are subdivided into two parts connected by a thread; continuous variation of their length enables the accurate adjustment of the detector modules.

The hexagonal and pentagonal frames of the honeycomb structure form a sphere with 860 mm diameter. The construction of this sphere as well as of the mounting bolts followed closely the example of the Heidelberg Crystal Ball detector [36]. The sphere is subdivided into two parts with 25 and 17 modules, respectively, which are fixed in octagonal stands as shown in fig. 11. Each stand is mounted on a slide and can be moved separately on rails over a distance of ~1 m. This allows to change the experimental flight path between neutron target and sample and to open the detector for access to the samples. Details of the mechanical construction can be found in appendix C.

The neutron beam passes the detector horizontally through two opposite hexagonal frames. Perpendicular to the beam axis, a sample changer passes through a rectangular grove of 30 x 10 mm in two opposite crystals; it carries up to eight samples,

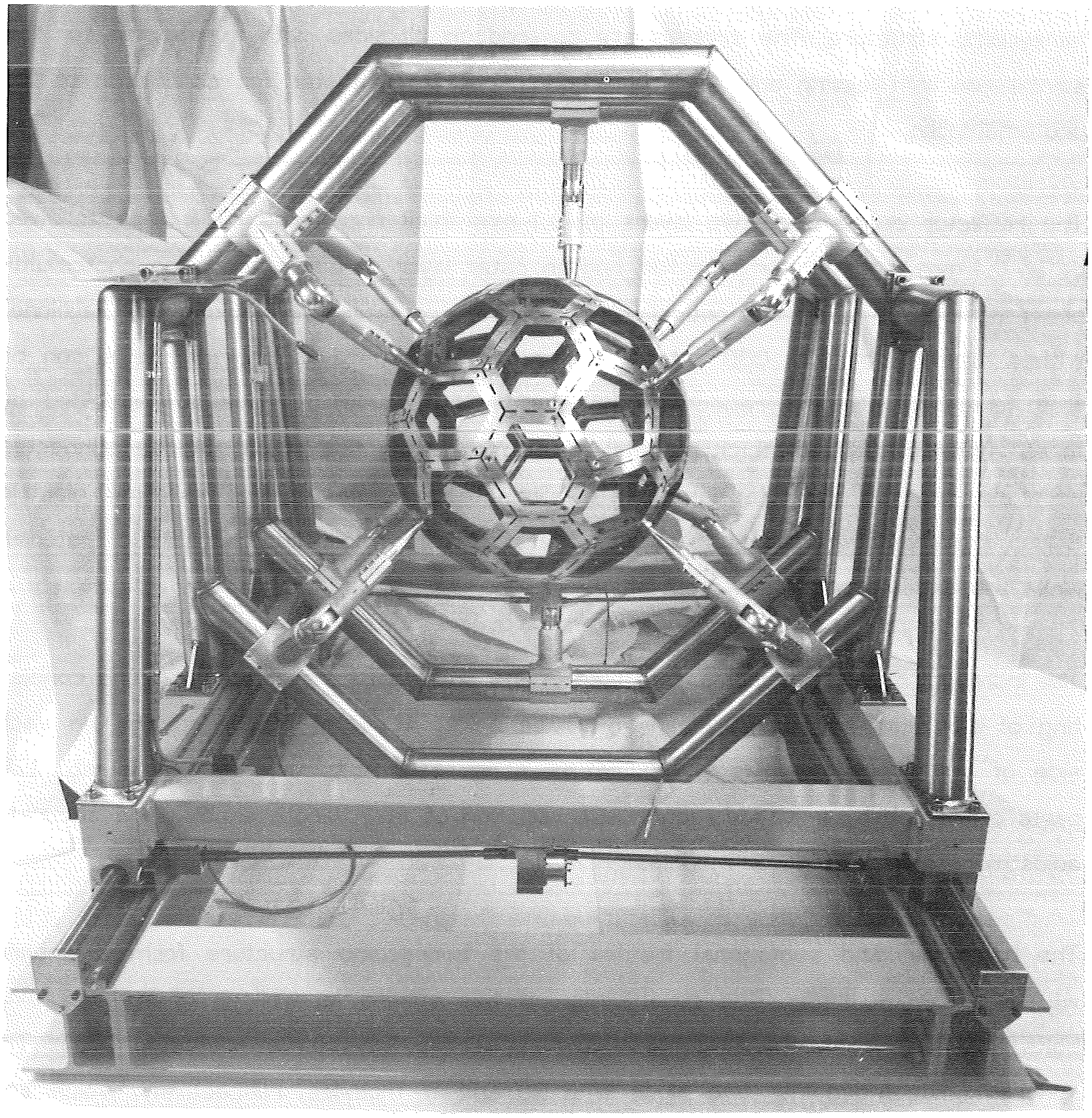

Fig. 11 The supporting honeycomb structure for the detector modules; the octagonal stands move on rails for opening the detector.

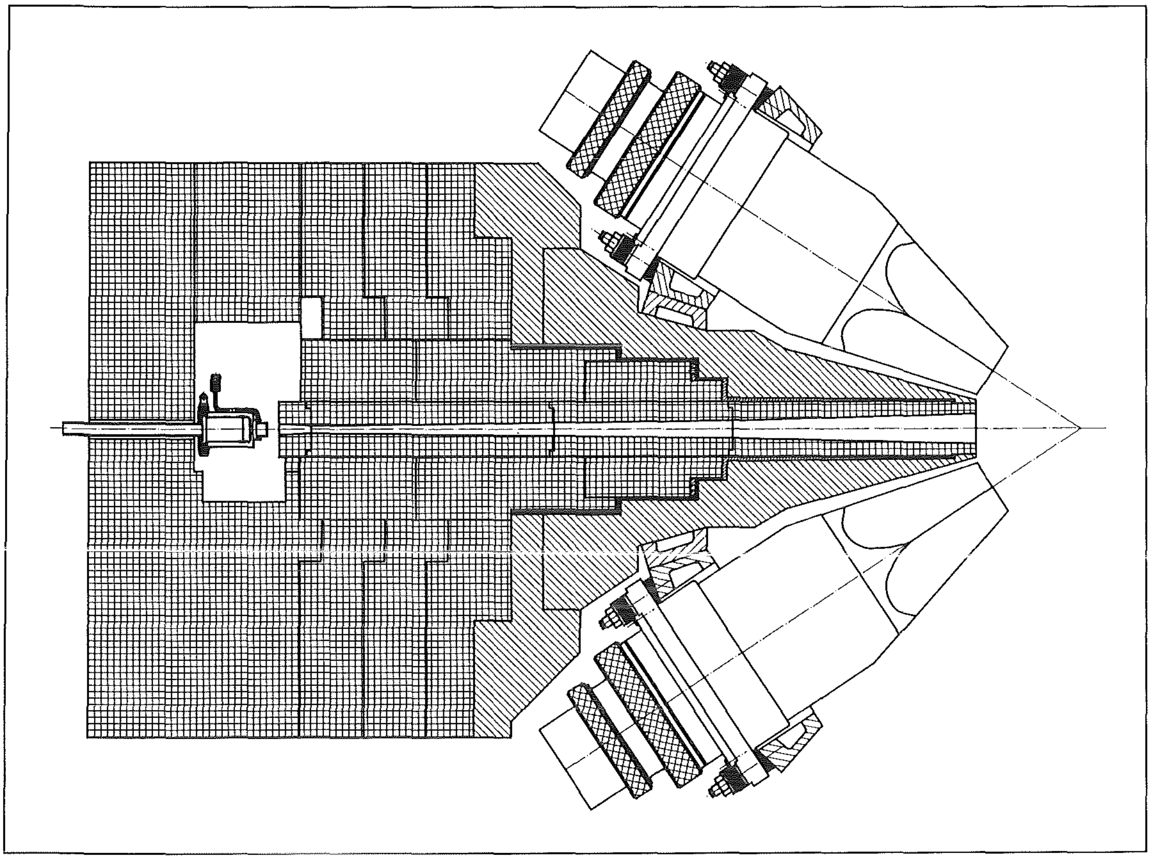

Fig. 12 The neutron target and the central part of the neutron collimator (hatched parts are made from lead and cross hatched parts from a mixture of boron carbide and araldite).

Table 3. Volume of the truncated hexagonal and pentagonal pyramids and the real crystals (liter).

	Hexagon	Pentagon
Truncated pyramid:	1.573	1.571
Real crystal:	1.472	1.484
Difference:	6.4 %	5.5 %

Volume of a spherical shell with $R_i = 10$ cm and $R_o = 25$ cm : 61.3 l

Volume of 12 pentagonal and 30 hexagonal truncated pyramids : 66.0 l

Volume of 12 pentagonal and 30 hexagonal crystals : 62.0 l which can be cycled into the measuring position by means of a computer controlled stepping motor. The samples are fixed on two 0.1 mm thick steel wires at selectable distances of up to 10 cm.

For the passage of the neutron beam two special crystals have been ordered with a central hole of 50 mm diameter. Each of these crystals will be equipped with six 1.5 inch photomultipliers (EMI 9902 QKA).

The water cooled lithium target for neutron production and the central part of the neutron collimator are shown in fig. 12. The first measurements will be performed with the minimum possible flightpath in order to obtain maximum neutron flux at the sample position. For this purpose the hexagonal crystal at the entrance of the neutron beam was removed using the free space for the collimator. The collimator is build in modular form using individual blocks made from natural boron carbide and araldite mixed in a ratio of 5:4 by weight. The inner cylinder can be replaced separately in order to change the beam diameter at the sample position, which is 24 mm in the present design. For the central part, collimator pieces from isotopically enriched ^{6}Li carbonate can optionally be used, offering radiationless neutron absorption and somewhat reduced neutron scattering. Towards the detector, the outer part of the collimator is made from antimony free lead to absorb the 478 keV gamma-rays from neutron capture in boron. On all other sides, the collimator is surrounded by at least 25 cm of boron loaded paraffin.

First measurements showed a significant background from neutrons scattered in the air along their flightpath through the detector. For the future it is planned to install an evacuated neutron flight tube with thin steel walls and windows from ~2.5 mg/cm^2 KAPTON foil.

Fig. 11 shows the supporting honeycomb structure for the detector modules fixed in the octagonal stands. The overall dimensions of the ground frame are 3.5 times 2 m. The completed detector opened for mounting of the samples is shown in fig. 13.

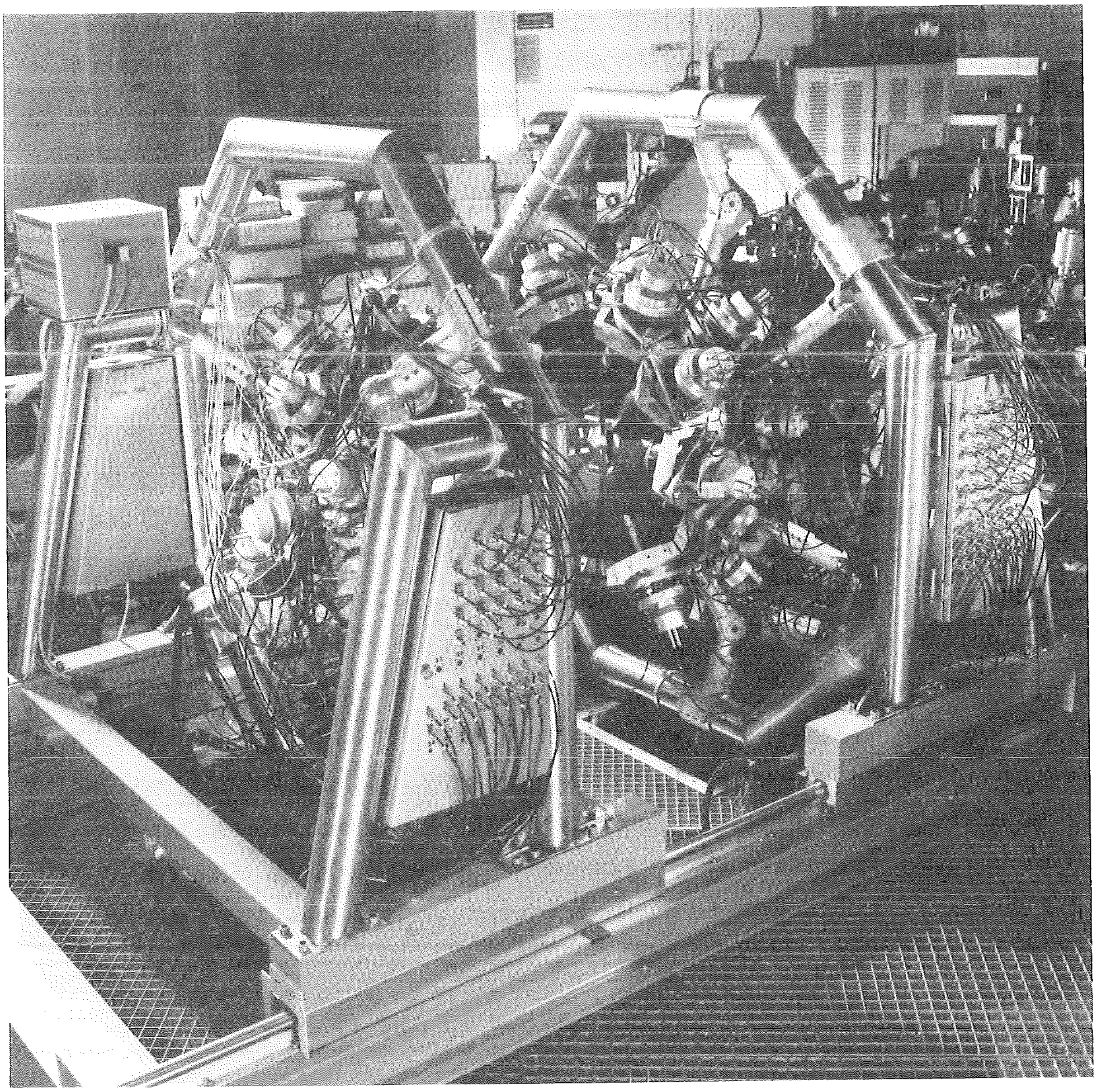

Fig. 13 The completed detector opened for mounting of the samples.

4 THE INDIVIDUAL DETECTOR MODULES

4.1 CRYSTAL HANDLING

The essential features of prototype crystals for the Karlsruhe 4π BaF_2 detector have been published elsewhere [14]. Here, we present more details and describe the modifications that have been made since as well as the properties of all 42 detector modules.

The ultraviolet scintillation light of BaF_2 at wavelengths between 190 and 410 nm is easily absorbed if the crystal surface is contaminated by grease. Therefore, it is strongly recommended to handle crystals with rubber gloves, which are carefully cleaned with ethanol or a compatible solvent. The crystals delivered by the manufacturer (Dr. Karl Korth, Am Jägersberg 9, 23 Kiel 17, Federal Republic of Germany) were reground by hand to remove possible absorbing impurities from the surface using grinding paper of increasing mesh numbers 350, 600, and 800. A significant amount of material was removed in this process using two sheets of the coarse and one sheet of the two fine mesh sizes for each crystal. Grinding was continued until the papers were saturated. The success of this procedure is demonstrated in fig. 14 showing an improvement in energy resolution for the ^{137}Cs line from 11.4 to 10.0 %. It has been argued by Anderson et al. [37] that for small BaF_2 crystals this improvement is achieved by simply removing adsorbed humidity from the surface, and that the resolution again deteriorates rapidly afterwards. Our experience is different: at least 2/3 of the observed improvement was permanent. As a general rule, we find that only about 0.5% energy resolution are lost during the first week after grinding.

In handling BaF_2 crystals one should keep in mind that fluorides in general are poisonous. In addition, the non negligible solubility of BaF_2 in water may facilitate the intake of the heavy metal barium. As informations about the real risk of ingested or inhalated BaF_2 are widely discrepant, all grinding was carried out in a chemistry laboratory under an exhaust.

4.2 REFLECTOR, PHOTOMULTIPLIER, AND VOLTAGE DIVIDER

Reflector and optical coupling between crystal and photomultiplier are as described in § 3.2 and ref. [14].

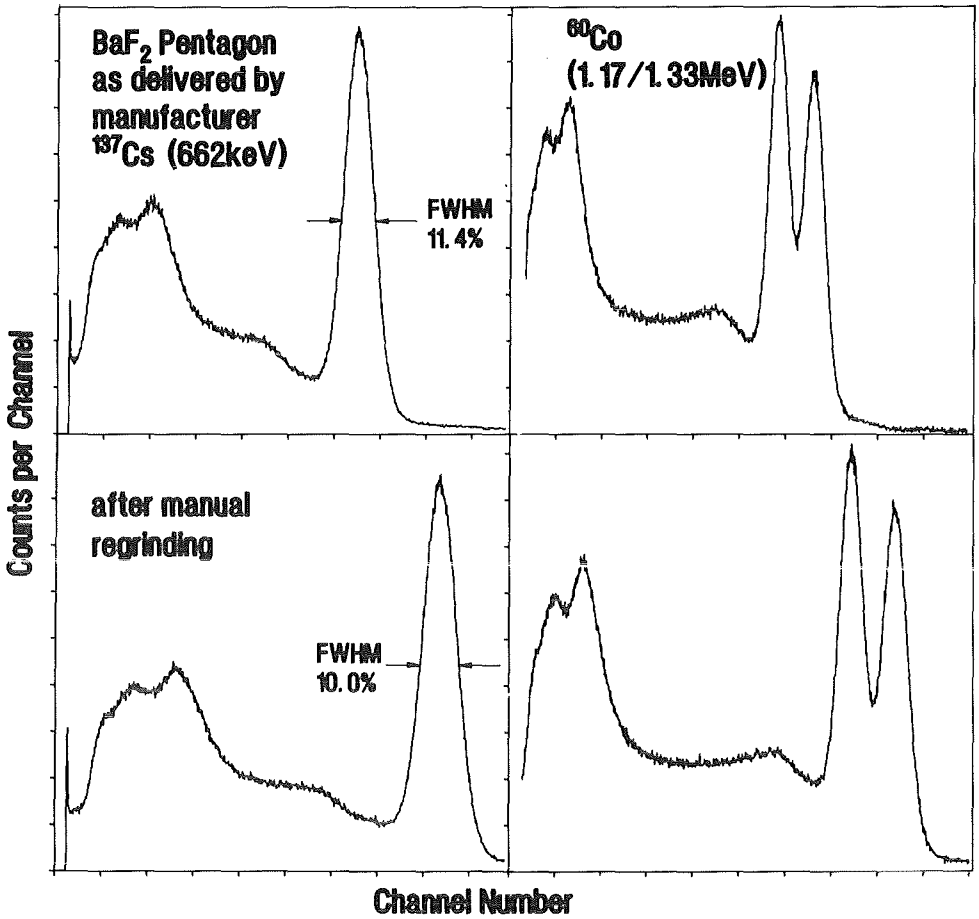

Fig. 14 Gamma-ray spectra from ^{137}Cs and ^{60}Co sources measured with a new BaF_2 crystal before and after manual regrinding.

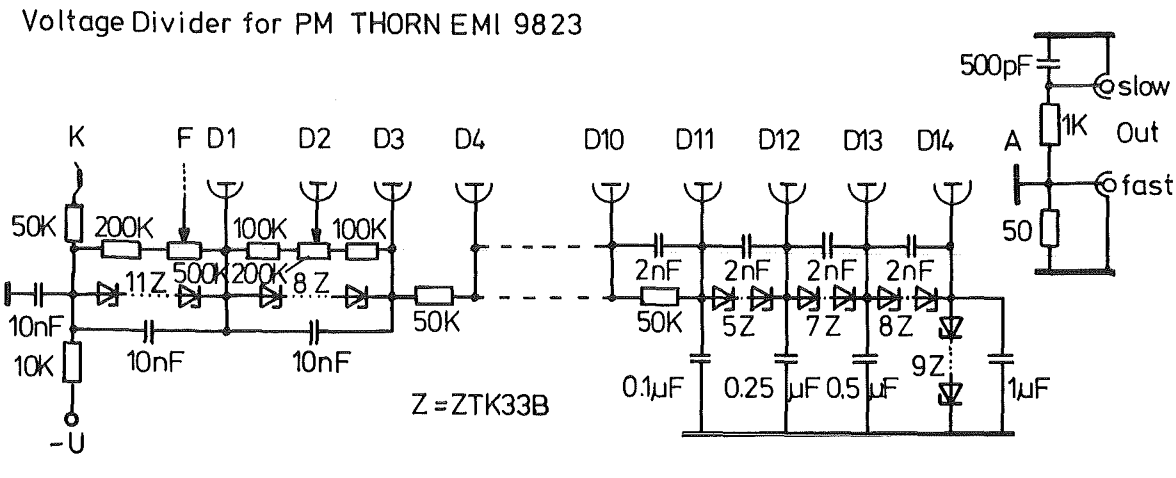

Fig. 15 Optimized voltage divider chain for the EMI 9823 QKA phototube.

To our knowledge, the EMI 9823 QKA is the only available photomultiplier by which good time and energy resolution can be obtained from large BaF_2 crystals simultaneously. Its relevant features are 5 inch diameter, fast rise time, and quartz window. Recently, however, the design of the tube was changed by replacing the conical edges of the quartz window by rectangular ones. These new tubes gave rather poor results with our oversize crystals, probably because the outer, less homogeneous part of the photocathode is more strongly illuminated in the modified version. Even with the outer regions of the cathode covered by inserting a thin ring of aluminum foil with an inner diameter of 12 cm between phototube and crystal, the energy resolution is degraded by at least 1% absolute (e.g. 11 instead of 10% for ^{137}Cs). Therefore, this new type of photomultipliers was not used in our detector.

For optimum energy and time resolution the voltage divider shown in fig. 15 was carefully adapted to the photomultiplier. Fast and slow outputs are provided for timing and energy measurements, respectively. The resistor chain is enclosed in an aluminum housing of 350 cm^3 and produces about 4 W at 2.3 kV cathode voltage. The potentials of the first and last dynodes are fixed by temperature compensated Zener diodes. As these diodes are available with a maximum voltage of only 33 V, each divider contains about 50 diodes. The potential of the focus electrode and the first dynode are adjustable to optimize signal output. All measurements were made with the slow energy signal adjusted for maximum pulse height. The inductances of the connections between dynodes are neutralized to reduce oscillations and to improve the signal rise time. All parts are on printed circuit and are arranged concentrically around the photomultiplier socket, thus minimizing the connection lengths. The voltage divider exhibits good temperature stability and resolution over long periods of time. The final design shown in fig. 15 was slightly modified compared to the version given in ref. [14] to obtain sufficient linearity for the fast component as well (see § 4.5); this improvement resulted in a reduction of the energy resolution, which amounts to ~0.4% absolute for the 662 keV line of ^{137}Cs.

4.3 PULSE SHAPE

The pulse shape of the fast signals from a detector module is shown in figs. 16, 17. Figure 16 has been recorded with a ^{137}Cs source using a fast digital oscilloscope (LeCroy model 4300) with pulse weighting option. As a criterion for the crystal

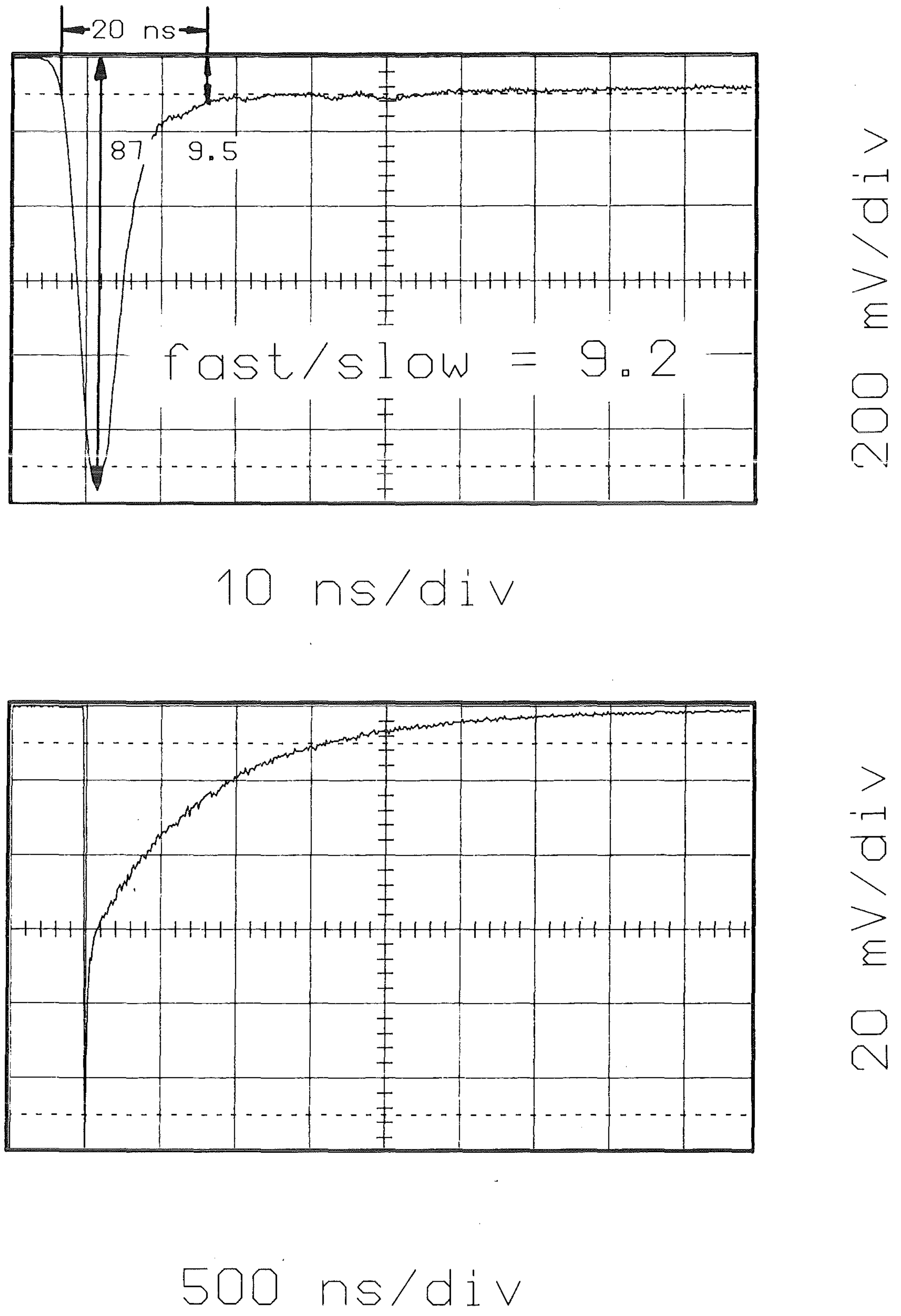

Fig. 16 Signal shape from a detector module for 662 keV gamma-rays from a ^{137}Cs source recorded by a digital oscilloscope with pulse averaging option.

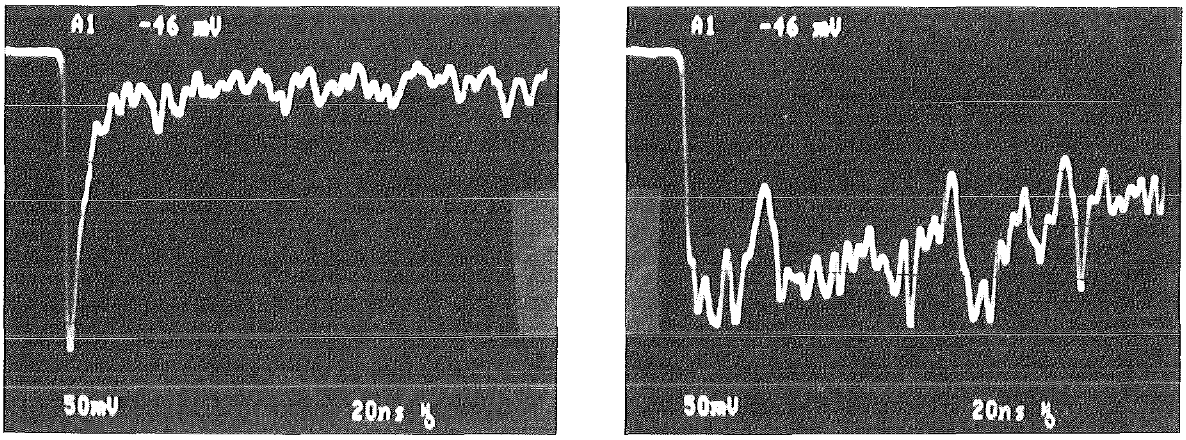

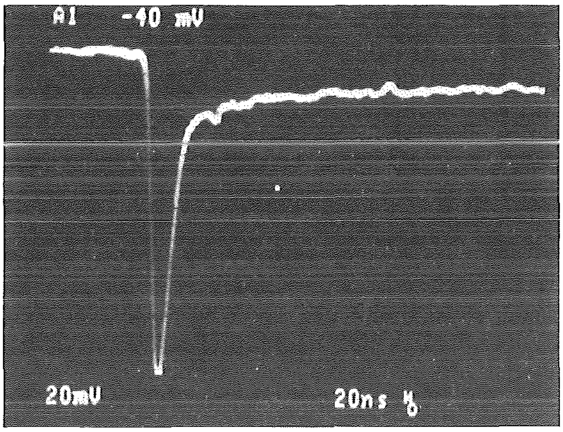

Fig. 17 Signals from a 1 l BaF_2 crystal from various sources recorded by a fast oscilloscope with channel plate amplification. The two upper pictures were taken at equal gain (662 keV gamma-rays (upper left), 7.7 MeV α-particles (upper right), cosmic μ-mesons (lower)).

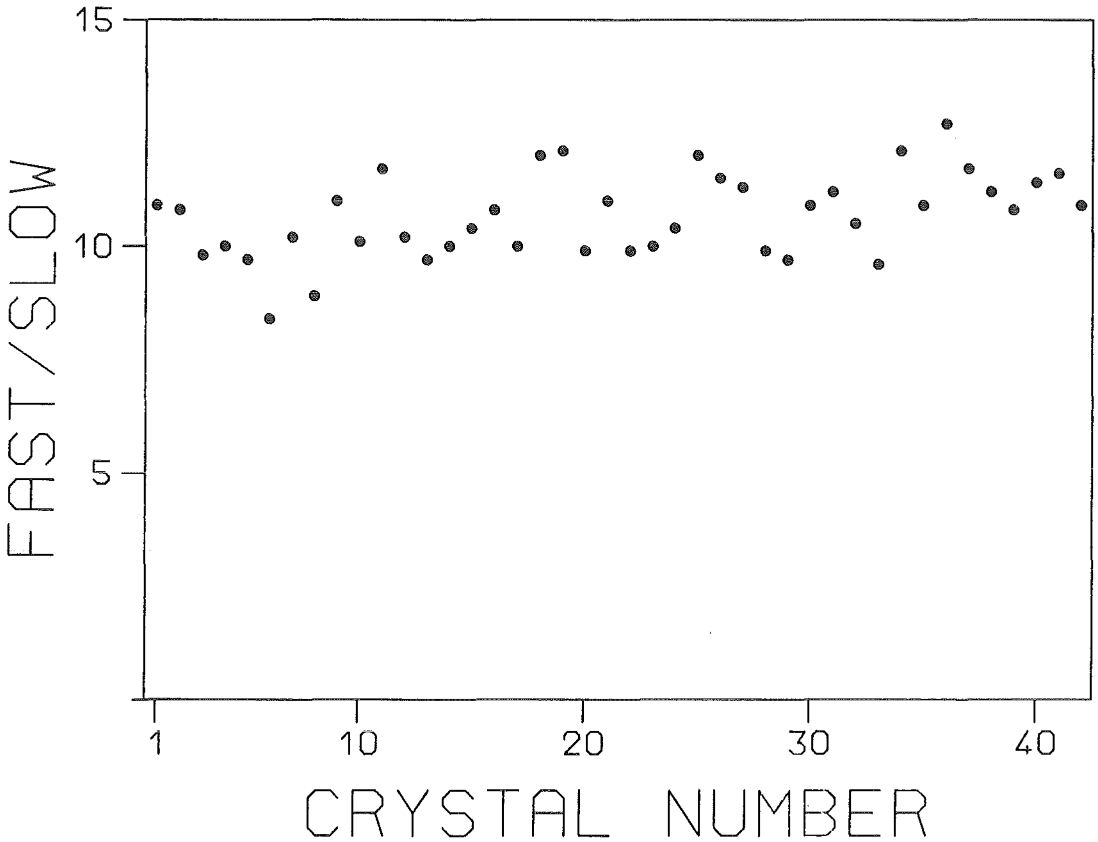

Fig. 18 The fast/slow ratio as defined in fig. 16 plotted for the 42 detector modules

quality a fast/slow ratio is defined by comparing the pulse height maximum with the respective value 20ns after the pulse has passed a threshold corresponding to the height of the slow component as indicated in fig. 16. This ratio was found to range between 8.4 and 12.0 for the 42 crystals of the 4π detector (fig. 18). The lower part of fig. 16 shows that the 600 ns decay time of the slow component requires an integration time of ≥ 3 μs for accurate energy determination.

Fig. 17 presents single pulses photographed from the screen of a fast oscilloscope with micro channel plate amplification (Tektronix model 2467) for 662 keV gamma rays, 7.7 MeV alpha particles, and cosmic μ-mesons deposing 7 MeV/cm in the crystal [38]. Note the absence of a fast component in the scintillation light induced by alpha particles. As the upper pictures were taken at equal bias voltage, the significant quenching of the alpha induced signals relative to those from gamma-rays can directly be estimated.

4.4 ENERGY AND TIME RESOLUTION

The energy resolution of all crystals was determined in a reference measurement using always the same photomultiplier and voltage divider. In a second series of measurements, the assembled detector modules were tested with the new voltage divider before mounting in the 4π detector. Fig. 19 shows the pulse height spectra from the best detector module for three gamma-ray energies. The measured energy resolution as a function of gamma-ray energy is given in the inset, indicating a clear correlation with photon statistics up to 6 MeV [14]. For all crystals, fig. 20 presents the energy resolution at 662 keV measured in the optimized reference setup and after assembling of the detector modules, the differences being mainly due to the quality of the photomultipliers, and the 0.4% degradation caused by the new voltage divider (§ 4.2). Recently, the energy resolution was remeasured after the modules were assembled for 1.5 to 2 y; only the eight crystals with the highest radium content had been exchanged 3 months before. Within the experimental accuracy, no changes in energy resolution were observed.

As a caveat it should be noted that the energy resolution of BaF_2 crystals is temperature dependent [15]. Therefore, values for the energy resolution should always be given together with the respective temperature. All measurements quoted in this work have been made between 20 and 25 ^{0}C.

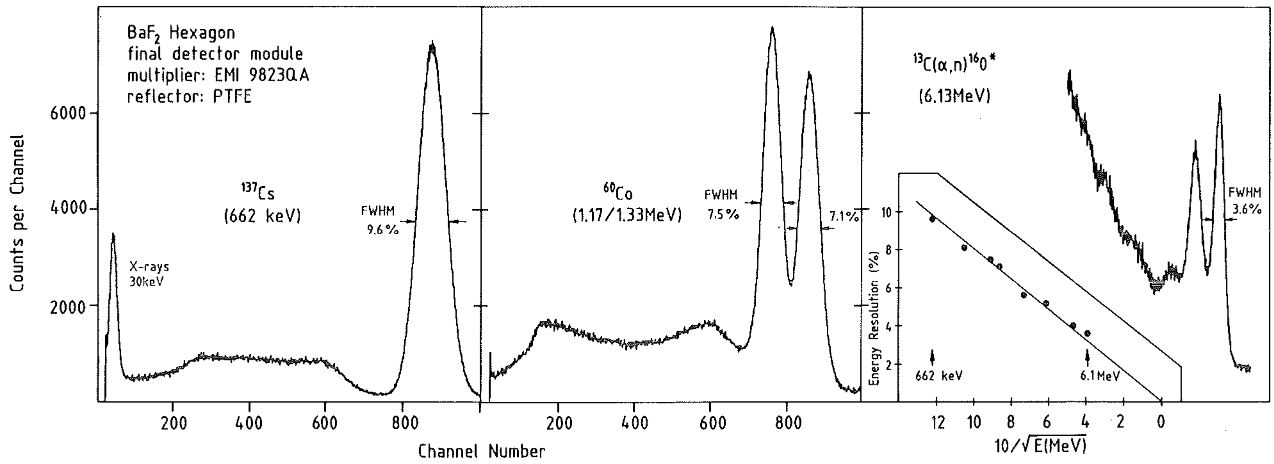

Fig. 19 The energy resolution of one detector module for gamma-rays in the range from 0.6 to 6.1 MeV.

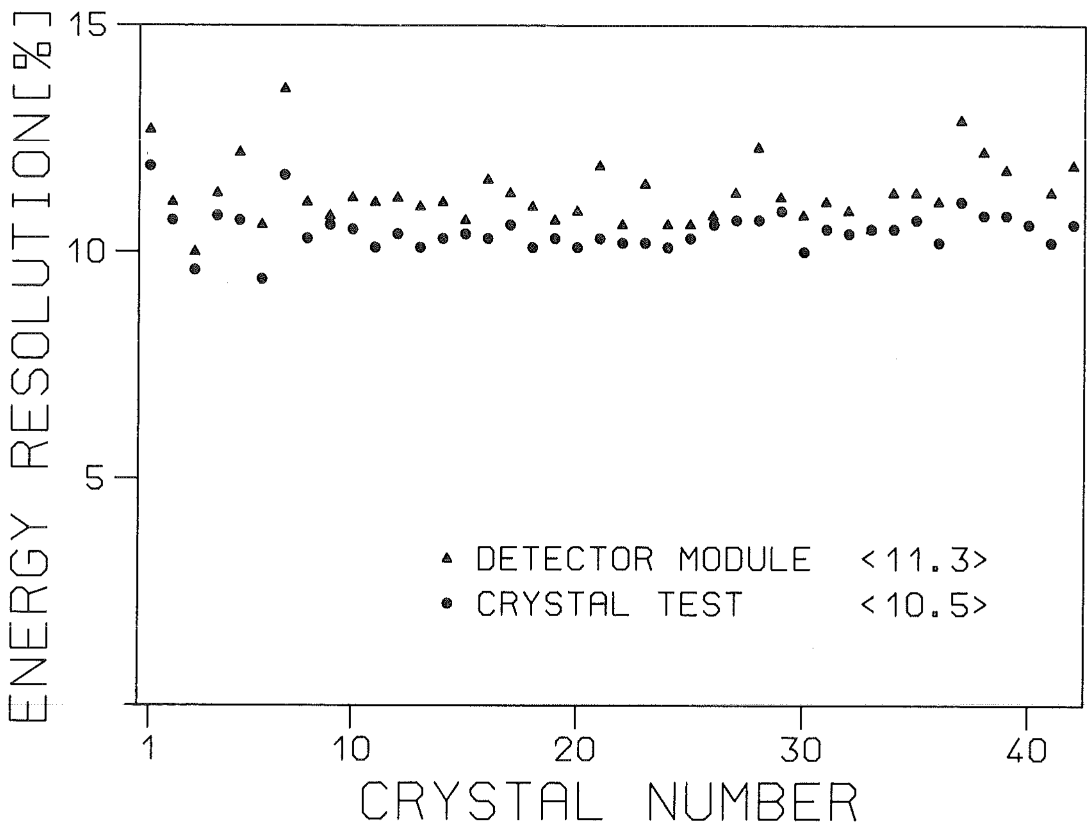

Fig. 20 Energy resolution measured for the 662 keV gamma-rays from a ^{137}Cs source during crystal testing and for the final detector modules. The difference is mainly due to the scatter of the photomultiplier quality.

The spectrum of fig. 21 shows the experimental time resolution relative to a fast plastic scintillator [14]. The results for 41 detector modules (fig. 22) have been determined from the completed 4π detector using one module as a start and all other modules as stop detectors. Both, start and stop detectors are connected to the electronics via 50 m long cables (see § 5); home made CAMAC controlled constant fraction discriminators (CFD) were used for the time signals. The so obtained results are slightly worse compared to the laboratory setup used for fig. 21 [14]. The values in fig. 22 represent the combined time resolutions of start and stop detectors, adjusted to the same threshold energy. All observed time peaks are symmetric as in fig. 21; hence, the full width at tenth of the maximum is also ~2 times larger than the FWHM.

4.5 LINEARITY

During the neutron capture experiments, a fast decision on the sum energy of an event is made by setting a threshold on a signal obtained by adding only the fast components of the scintillation light from all 42 modules (§ 5.2). This procedure requires a good linearity of the fast component at least up to energies of about 6 MeV. As described in § 4.2, the corresponding change of the voltage divider resulted in a slightly reduced energy resolution. In fig. 23 the energy calibrations for the fast and slow component are plotted for a typical bias voltage. At 6.1 MeV gamma-ray energy, the deviations from linearity are 2.6 and 7 % for slow and fast component, respectively.

4.6 BACKGROUND

The only essential drawback of BaF_2 crystals is the background caused by radium impurities, which are always present as radium and barium are homologuous elements. The contributions from the decay chains of ^{226}Ra and ^{228}Ra are indicated in the spectrum of fig. 24, which was taken with a test crystal cooled to −30 °C. At present, the ^{228}Ra contribution is ~4 times smaller than that of ^{226}Ra and decreases due to the short ^{228}Ra half-life of 5.8 y. The spectrum is dominated by the four alpha lines from the decay chain of ^{226}Ra. In the present application, however, these lines can easily be discriminated; according to fig. 17, a gamma-ray threshold of ~700 keV is sufficient to eliminate them completely, and in actual experiments a threshold of

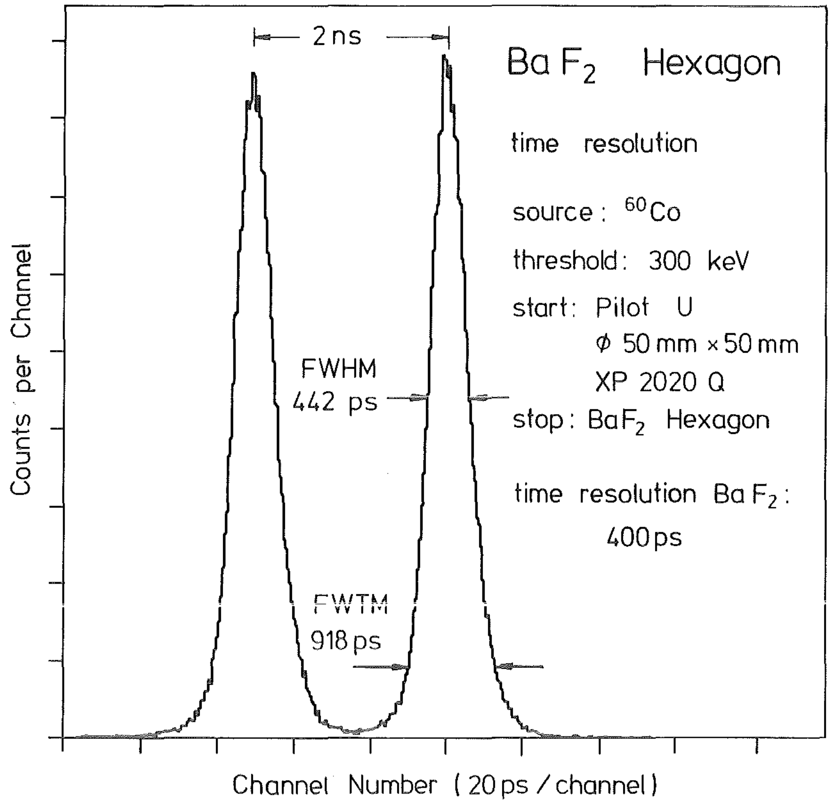

Fig. 21
Time resolution
measured with
one detector
module.

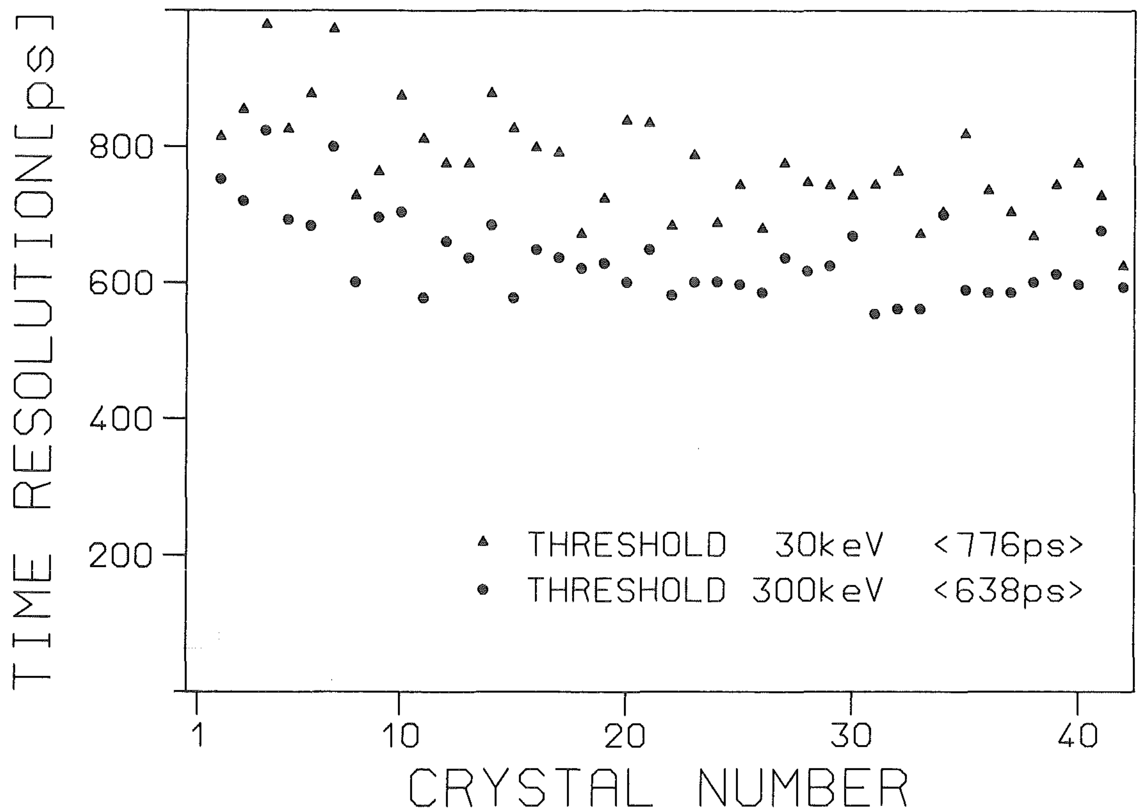

Fig. 22 Time resolution measured in a coincidence experiment with a ^{60}Co source using one fixed detector module as start detector and successively all other 41 detector modules as stop detectors. The quoted numbers represent the combined time resolution of start and stop detectors.

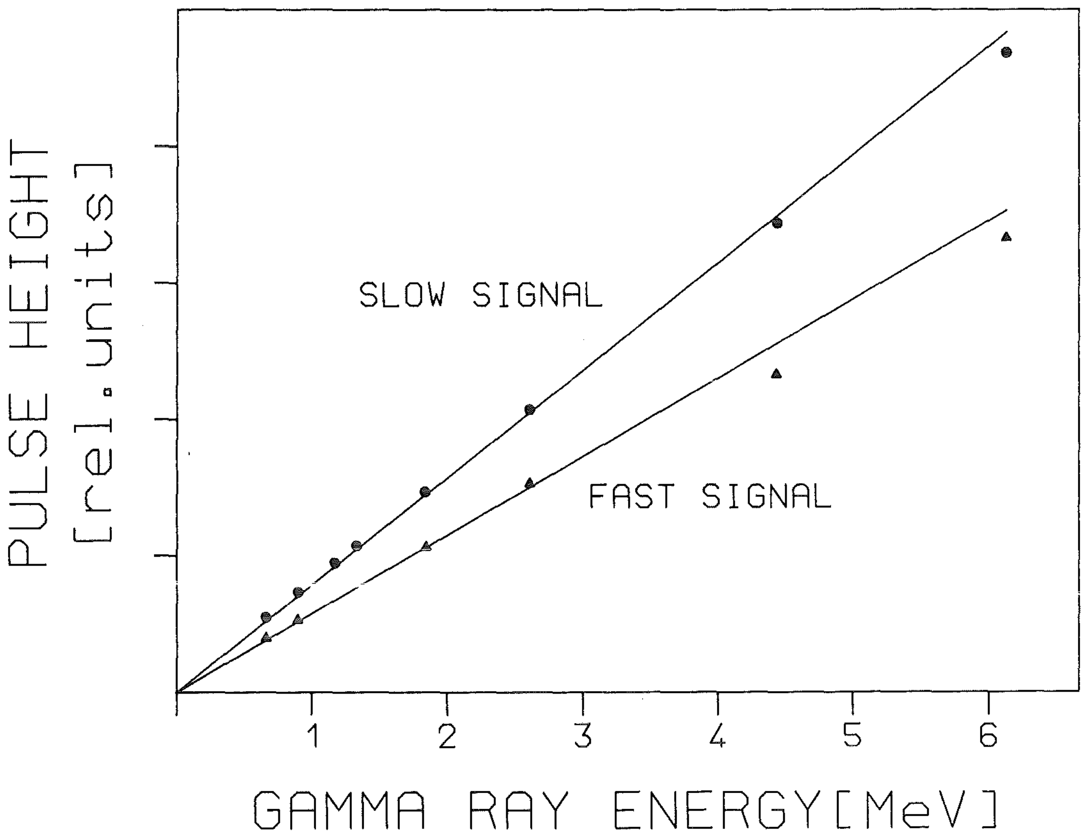

Fig. 23 Pulse heights of the fast and slow component in the scintillation light as a function of gamma-ray energy.

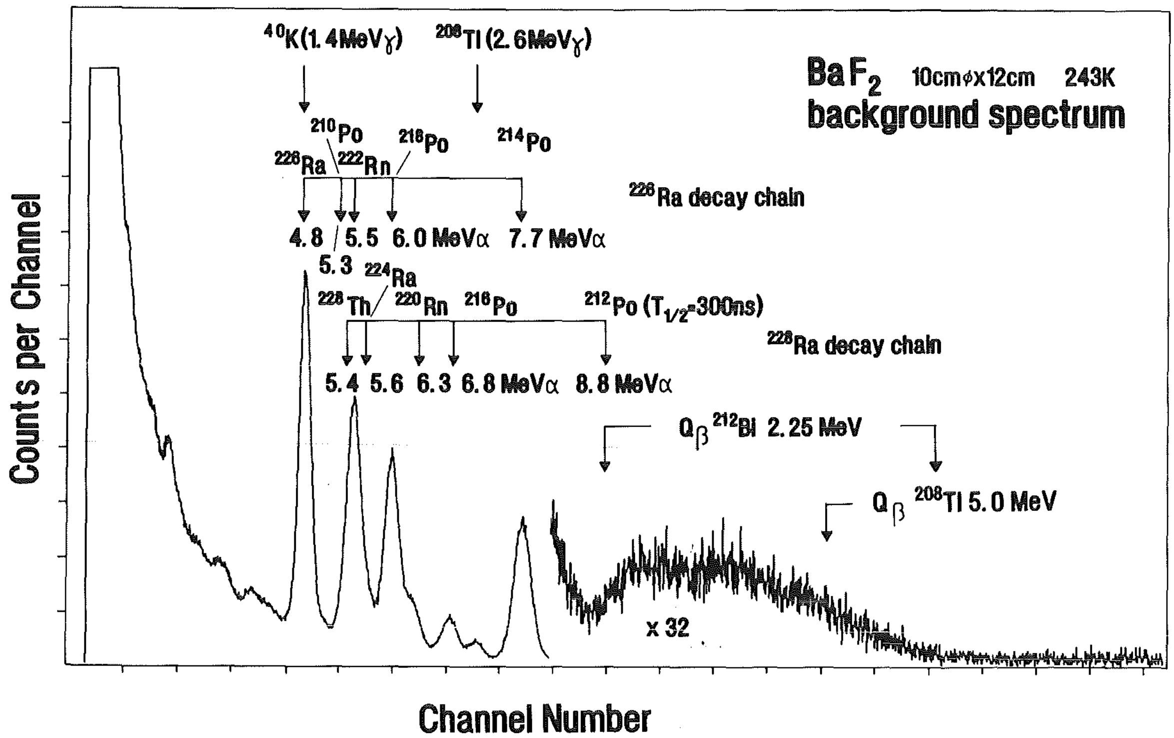

Fig. 24 Background spectrum measured with a cooled test crystal.

2.5 MeV will be used in the fast sum energy signal (§ 5.2). More disturbing is the background due to beta decay, giving rise to electrons and coincident gamma-rays (fig. 25). The decay chain of ^{226}Ra yields a contribution with a maximum energy of 3.2 MeV, while two components with a maximum energy of 5 and 5.6 MeV are related to the decay chain of ^{228}Ra. In the latter case, the decay of ^{208}Tl produces electrons and gamma-rays in prompt coincidence, whereas the decay of ^{212}Bi occurs as a delayed coincidence between an electron and an alpha particle from ^{212}Po. Consequently, the second background contribution can also be eliminated by a 2.5 MeV threshold on the fast sum energy, since the alpha induced signal is delayed in time and does not exhibit a fast component.

For characterizing the radium background, the integral count rate of the four strong alpha lines is plotted in fig. 26 for each crystal. The crystals are numbered according to their production date. After this problem was recognized by the manufacturer, the background rate could be reduced to ~200 s^{-1} per crystal (7.2 kg BaF_2).

In table 4, intrinsic and external background rates are compared for different threshold energies. For crystals with low radium content one finds that the countrate above 1 MeV is already dominated by room background. The values of table 4 were determined with the modules mounted in the completed 4π detector, and are representative for the experimental environment (including self-shielding of the modules by themselves against the room background from 2 m thick concrete walls).

4.7 LONG TERM STABILITY

The long term stability of the detector modules was followed over 2.5 y. The energy resolution of a module that was recently removed from the 4π detector was found almost unchanged since it was assembled 1.5 y ago (10.7 instead of 10.3 %). However, in the same time the fast component decreased by 20 %. After the phototube was disassembled, cleaned, and remounted, the original performance could be completely restored. Obviously, the UV transmission of the optical coupling between crystal and photomultiplier decreases with time so that it may be necessary to replace the silicon oil after several years of operation.

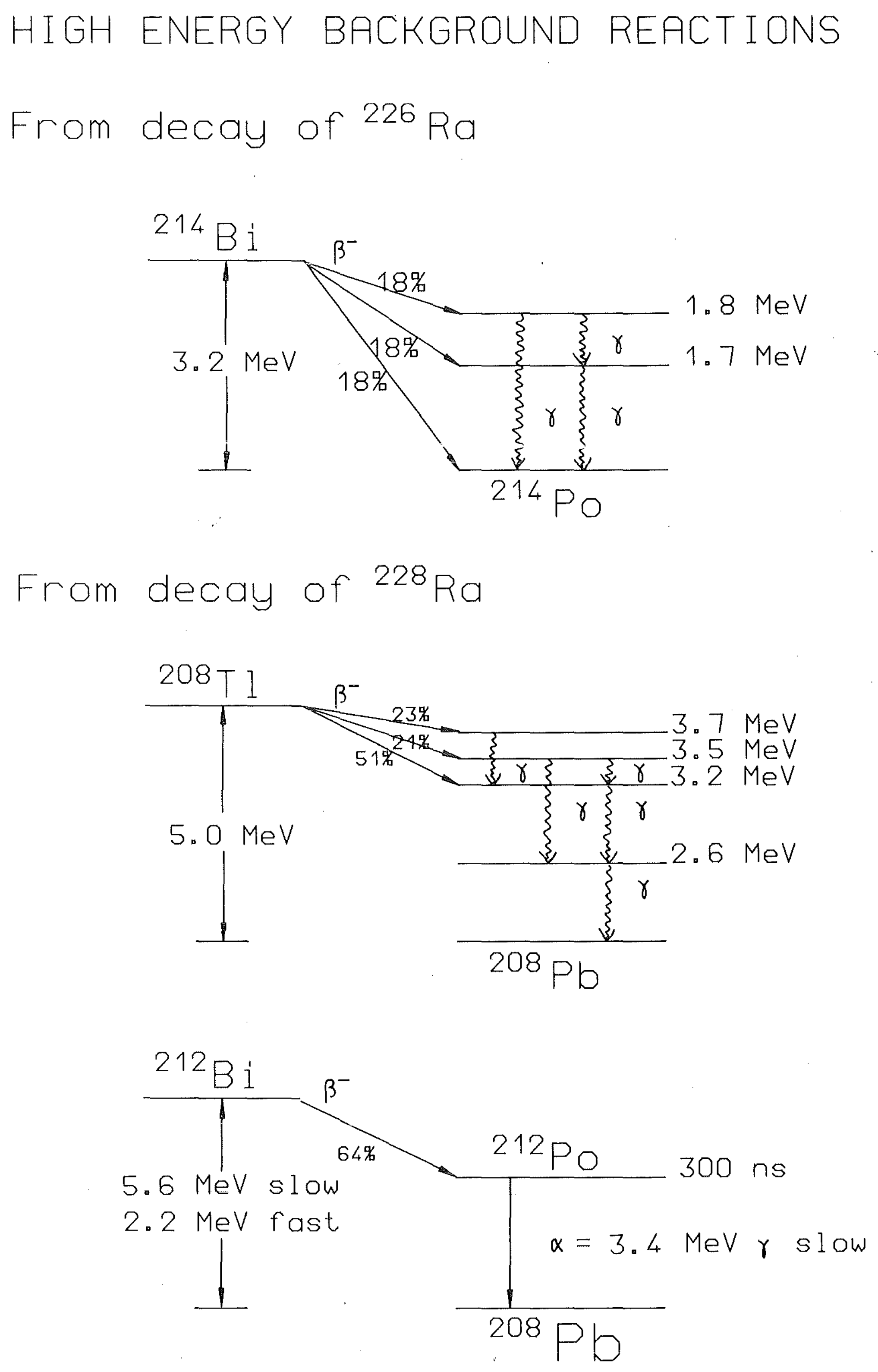

Fig. 25 The radium decay channels giving rise to energetic background.

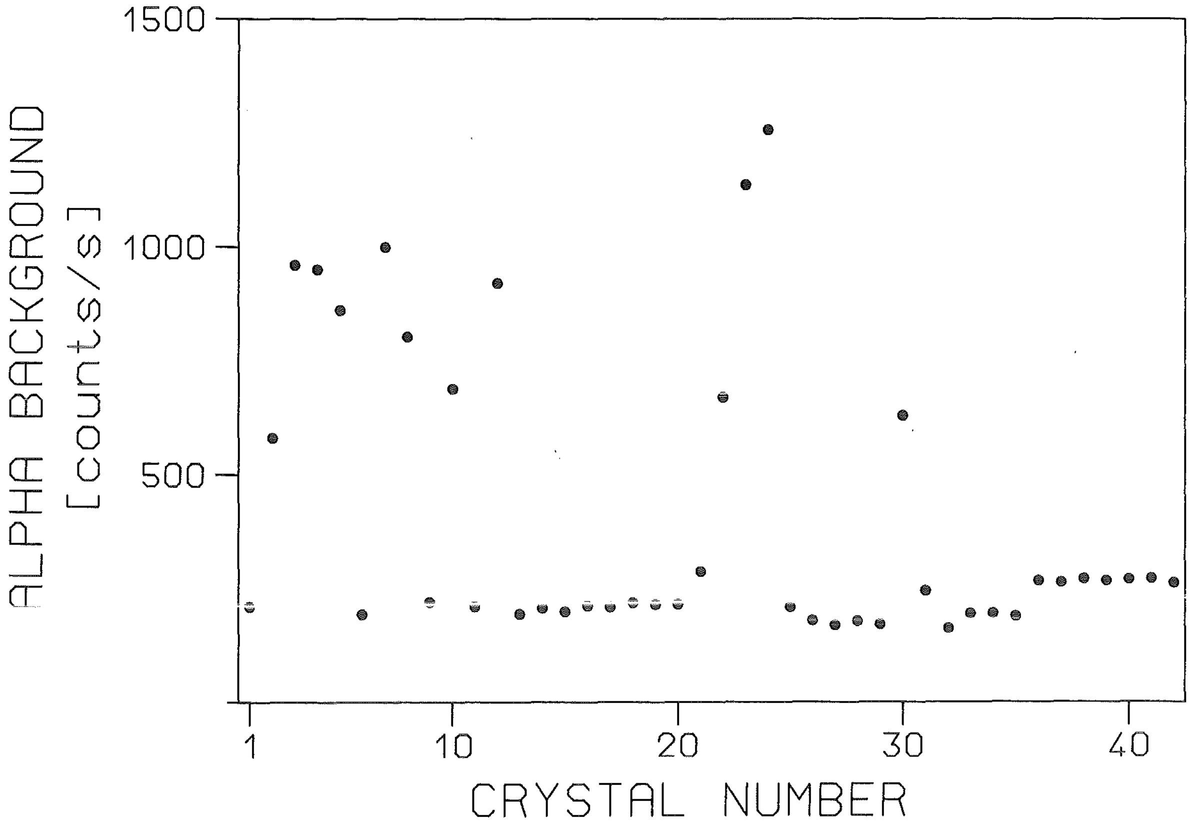

Fig. 26 Background countrate of the 42 crystals integrated over the four prominent alpha lines, and including the contribution from ^{40}K.

Table 4. Background countrates of crystals with high and low radium impurities.

Gamma-ray threshold (keV)		Room background gamma-rays (counts/s)	Radium impurities α-particles (counts/s)	Radium impurities β+γ (counts/s)
50	low	256	200	324
	high	256	1000	1620
1000	low	74	0	56
	high	74	0	280
2000	low	29	0	23
	high	29	0	110

5 DETECTOR ELECTRONICS

5.1 GENERAL ASPECTS

In the first stage of development the 4π detector is used as a calorimeter. For each accepted event the sum energy and the time of flight is stored together with the gamma-ray multiplicity. The multiplicity is determined by recording a 42 bit pattern indicating those detector modules that have fired. This three-dimensional information E x TOF x MULT is sufficient for the determination of neutron capture cross sections.

In a second stage a multi ADC/TDC system will be installed for recording pulse height and time of flight separately for each detector module. This will improve the gamma-ray energy resolution by eliminating small differences in the response of the individual modules, and will yield additional information on capture gamma-ray spectra and angular distributions.

As typical measuring periods of ~2 weeks per sample are expected, a reliable and stable long term operation of the complex 4π detector is required. At present, about 50 % of the electronics is used for this purpose. All relevant signals are doubled by fan-out units. Via multiplexers with 42 inputs and one output these signals can be displayed on oscilloscope, or can be used for determination of count rates and for automatic stabilization and adjustment procedures.

As, at present, the signals of the individual modules are added on-line for deriving the sum energy, it is important to maintain equal response for all modules, because later corrections are impossible. Therefore, gain shifts and day-night differences due to temperature changes have to be compensated. The required long term stability of the 42 modules is achieved via the outstanding 7.7 MeV alpha line in the background spectrum (fig. 24) which is used as an internal calibration standard.

Most of the electronics consist of commercial NIM and CAMAC units. The CAMAC discriminators and multiplexers have been copied from the Heidelberg Crystal Ball project. A CAMAC controlled linear gate, a programmable 16db attenuator, a fast 42-fold OR unit, as well as fast and slow preamplifiers for driving the relatively long cables between detector and electronics have been specifically developed for the present setup. A NOVA4 computer serves for adjustment, control, and permanent stabilization of the 4π detector, and a Data General MV4000 computer is used for data acquisition.

The electronics used with the 4π detector is described in the following subsections, separated according to the aspects of signal processing, detector control, and data acquisition.

5.2 SIGNAL PROCESSING

The electronics for signal processing is illustrated in the block diagram of fig. 27. From the voltage divider of each detector module a fast and a slow signal with a 500 ns time constant are derived. The slow signal is amplified by a factor of 2.5 using a cable driver circuit as shown in fig. 28. The amplifier is separated from the voltage divider by a 10 cm long cable in order to reduce the thermal load of the voltage divider. The signal amplitudes obtained with the 662 keV gamma-rays from a ^{137}Cs source are adjusted to 200 and 600 mV for slow and fast pulses, respectively. The detector in the strongly shielded experimental area is connected with the subsequent electronics by ~50 m long cables. On this way, fast signals loose ~20% in amplitude though cables with low damping (RG 213) are used, whereas slow signals (RG 58 cables) remain practically unchanged.

At present, fast and slow signals are not completely decoupled; this leads to an increase in the noise level of the slow signal from 2 to about 15 mV, changing the resolution for the 662 keV gamma line of ^{137}Cs from 10 to ~12%. This problem will be solved in the near future by a 1:1 cable driver for the fast signal.

The fast signals pass a CAMAC delay unit (SEN FE292C; 64 steps of 250 ps), by which differences in cable length and electronic transit times are compensated in order to obtain a well defined timing signal for the TOF measurement. The following CAMAC attenuator (16 steps from 0 to 15 db) adapts the pulse height to the input requirements of the following units, and adjusts the fast component of the signals to equal amplitude for all detector modules. By this attenuator, any variations of the fast component with time (see § 4.7) can be compensated.

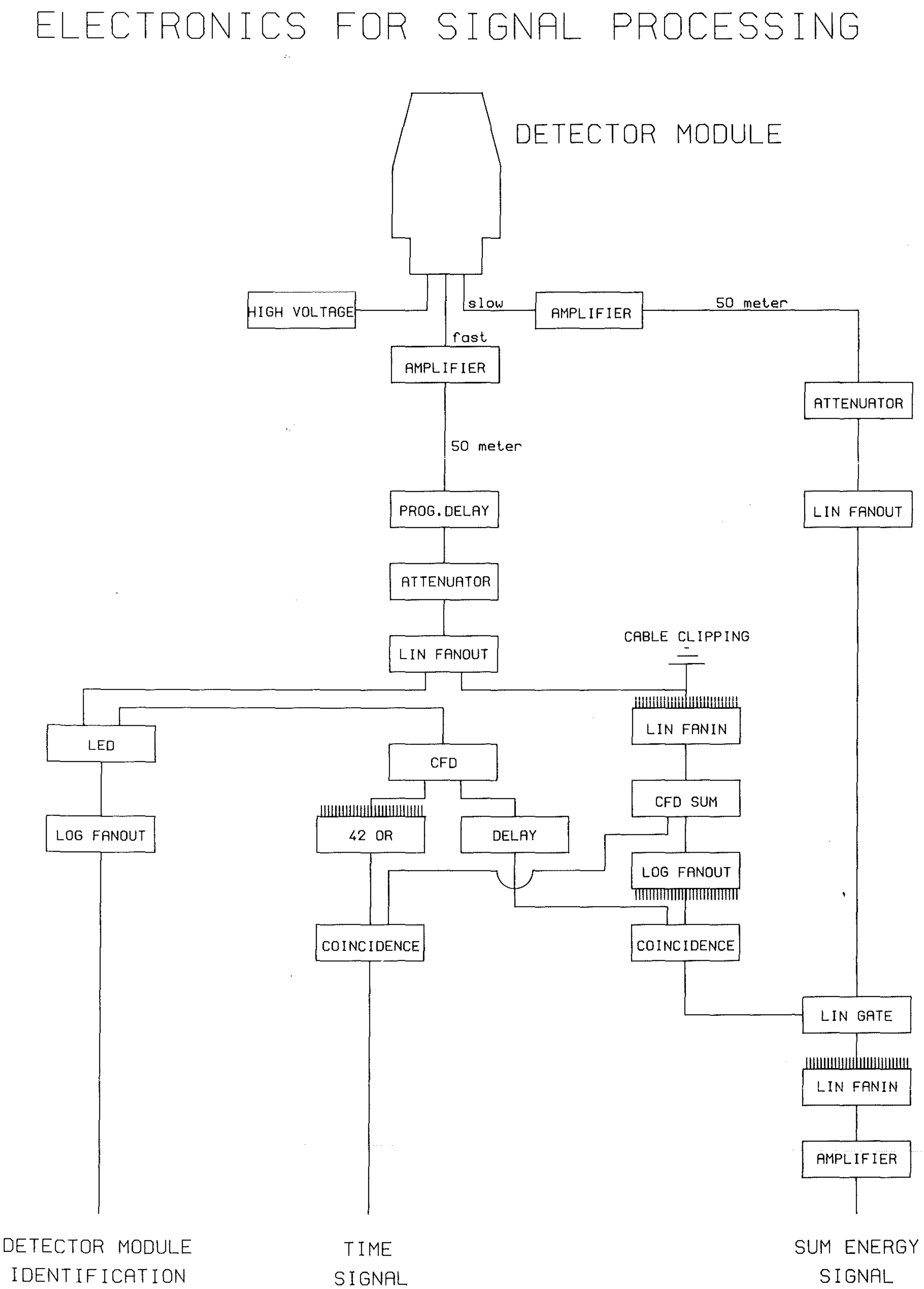

Fig. 27 Electronics for signal processing (modules with 42 inputs or outputs are marked accordingly).

The input of the following fan-out (LeCroy 429A) being limited to −2 V means that fast signals up to 6 MeV gamma-ray energy can be processed linearly in the fast branch of the electronics using attenuation factors of typically 10 db. The respective output signals are used to feed various branches:

(i) In the first branch, the signals are clipped by 2 m long delay cables to remove the slow component. The outputs of all 42 detector modules are then added (LeCroy 429A) to obtain a fast sum energy signal of only 10 ns width, which still yields an energy resolution of ~20 % at 1 MeV gamma energy. Only if this fast sum energy signal exeeds a certain threshold, the correlated event might be due to neutron capture and is processed further. In this way, background from low energy gamma-rays, alpha particles, and part of the background from beta decay of radium impurities (§ 4.6) is eliminated. In principle, this threshold should be kept as low as possible because the pulse height distribution of capture events reaches down to the 2 to 3 MeV range (§ 8). In practice, the accepted event rate is limited by the capacity of the magnetic tapes; this implies a threshold of ~2.5 MeV.

(ii) Another output is fed through the bridged input of a leading edge discriminator (LED) to a constant fraction discriminator (CFD), which creates the logic time signals for the TOF measurement; simultaneously, it is used (in coincidence with the main trigger signal) to open the linear gates for the slow energy signals. To avoid multiple triggering from the slow component of the scintillation light a dead time up to 3 µs can be selected. This can be tolerated in the present application where the integral countrates of the detector modules are well below 5 kHz. It is possible to block the output via CAMAC command, a feature that is important for adjusting the 4π detector (§ 6.2). The logic time signals of all detector modules are combined in a home made 42-fold OR to derive the final start signal for the time to amplitude converter (TAC). The OR unit is designed in SMD technique; it yields an output signal almost independent of the multiplicity pattern at the input (jitter less than 200 ps; see § 7.3). The stop signals for the TAC (Ortec 457) are derived from the accelerator pulses by a pickup electrode.

(iii) In a third branch of the fast signal, a 42 bit pattern is produced for the identification of those detector modules that have fired. The output signals of the LEDs are sent to a home made channel identifier, which adds the digitized information on the

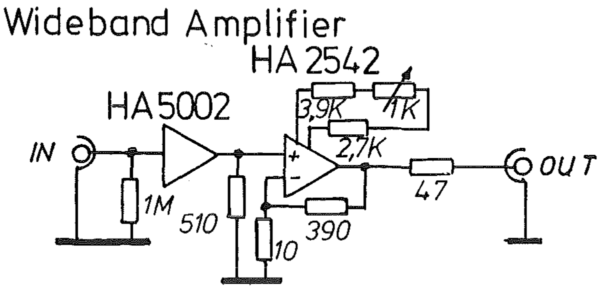

Fig. 28 Wideband amplifier for the slow energy signals.

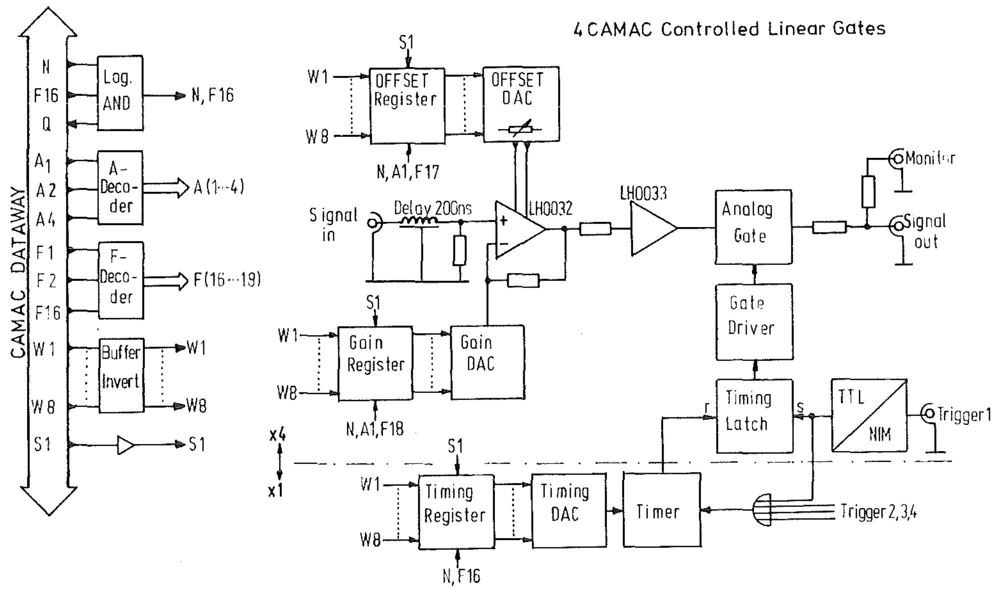

Fig. 29 Schematic diagram of the CAMAC controlled linear gates.

ELECTRONICS FOR S

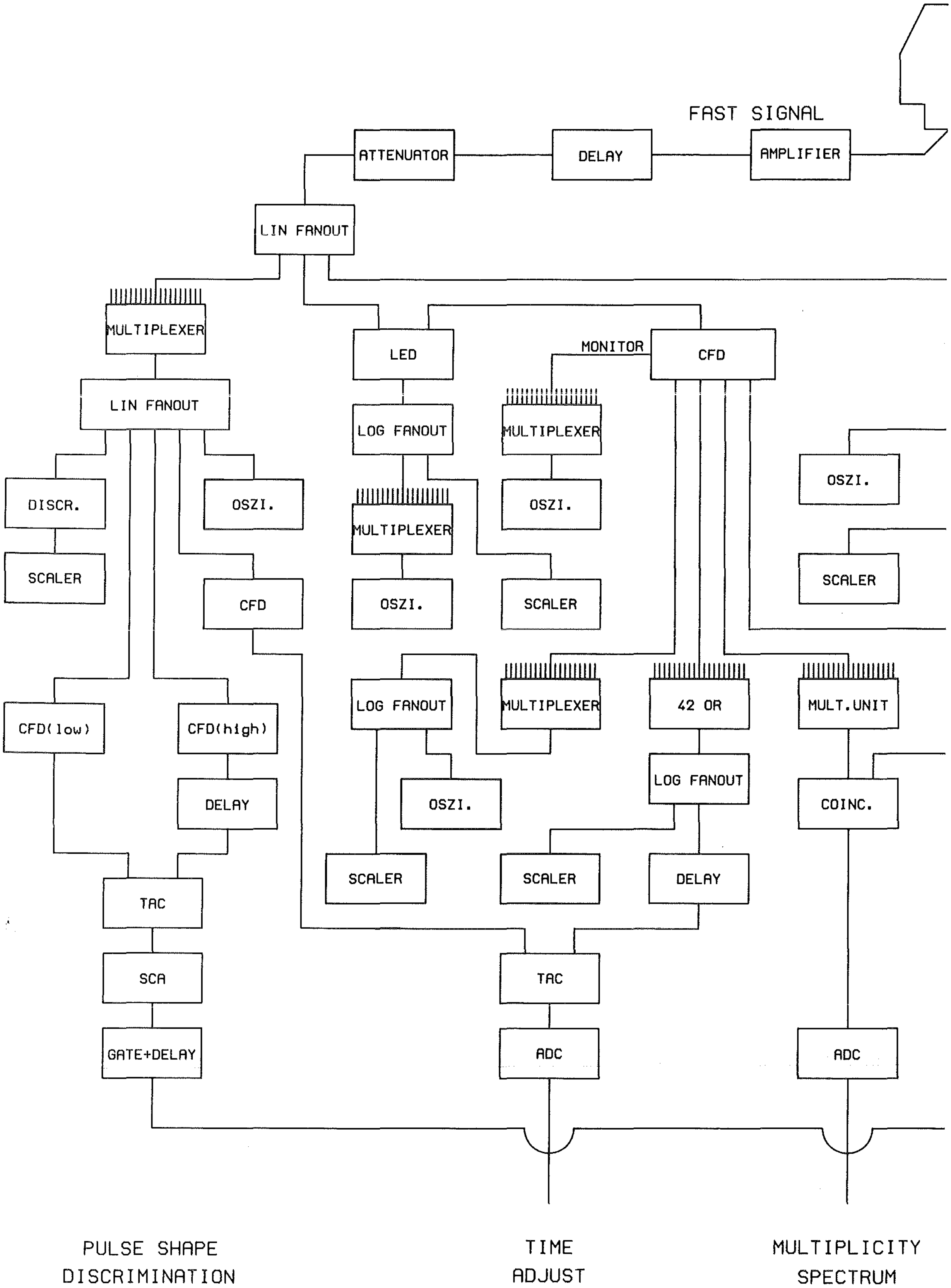

Fig. 30 Electronics for detector control (modules with 42 inputs or outputs are marked

URVEY OF OPERATION

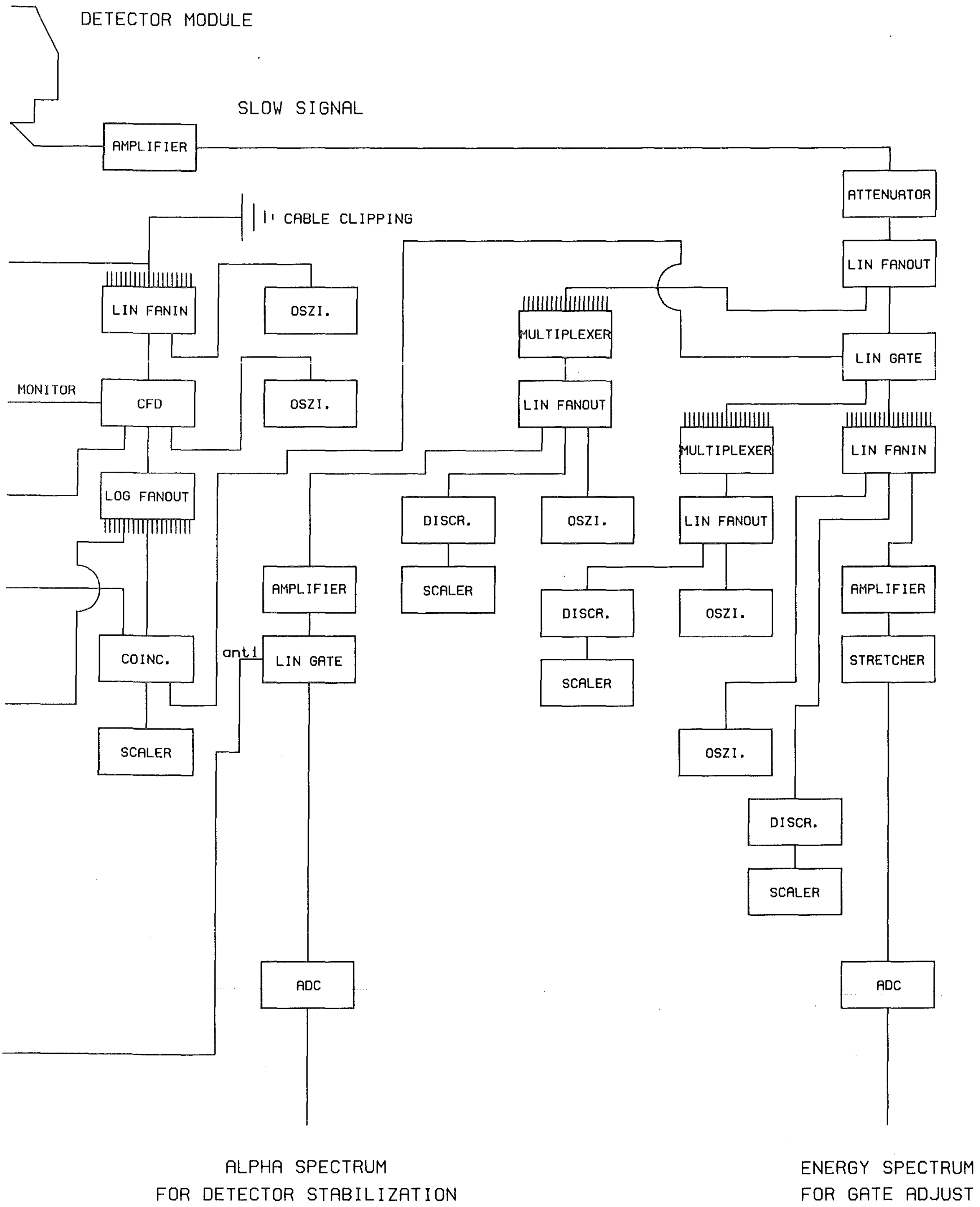

accordingly).

contributing modules to the bit pattern from pulse height and TOF analysis for final storage in the data acquisition computer. Note, that the use of separate discriminators allows to set different thresholds for the sum energy and the multiplicity pattern.

Processing of the slow signals is rather straightforward as indicated in fig. 27; after passing a fixed attenuator (6 db) they are multiplied in a linear fan-out (LeCroy 429A). The adjustments are such that gamma-ray signals up to 12 MeV can be accepted without saturation effects.

The following linear gates are home made CAMAC units (see fig. 29 for a schematic wiring diagram); apart from the possibility to select the gate width between 0.5 and 5 µs, these units allow to change the input pulse height by ±20% and the offset by ±10 mV via CAMAC commands. In this way, gain and offset of each detector module can be adjusted independently, without changing the bias voltage and thus the pulse height of the fast signal. This is an important feature as the fast/slow ratio can be different for different crystals (fig.18), and may also change with time (§ 4.7).

The output pulses of the 42 linear gates are added by means of linear fan-in modules (LeCroy 429A) to a sum signal with good energy resolution that is sent to an ADC for final data acquisition. The use of linear gates ensures that only those modules contribute to the final sum signal that have fired in the particular event, thus minimizing the effect of multiplier noise in the summation.

5.3 CONTROL ELECTRONICS

The large fan-out capacity together with a set of six multiplexer units allows to observe all important branches in the electronics on oscilloscope or to handle the respective pulses in further electronics. By means of the home made CAMAC multiplexers any one of the 42 input signals can be selected to appear on output by means of micro relais. As indicated in fig. 30, the following signals are accessible in this way: slow, fast, CFD output, CFD monitor output, LED output, and GATE output.

Two sets of 42 CAMAC scalers (LeCroy 2551) are used for continuous control of the output rate of coincidences and LED discriminators. Four additional scalers are used to monitor the multiplexer outputs; this allows to record the respective count rates of all 42 detector modules by a computer routine. Two other scalers serve for counting the integral rate of the 42-fold OR and of the CFD in the fast sum signal (fig.30). Other aspects will be discussed in § 6.

With these features, the operation of the 4π detector can be surveyed without disturbing data acquisition, even without removing a single cable connection.

5.4 ELECTRONICS FOR DATA ACQUISITION

The electronics for data acquisition is shown in fig. 31. Only events from an appropriate time window between successive accelerator pulses are accepted in the TOF measurement, and a common dead time for TOF and energy branch is introduced after each valid event. This is achieved by means of two gate generators in combination with two updating discriminators and suited delays. The output of the second updating discriminator is also used to ensure that an event is only recorded if both, TOF and sum energy signals are available, and to start the transfer of the 42 bit pattern for identification of the contributing detector modules.

The 64 bit word containing sum energy, TOF, and detector multiplicity is stored in list mode on magnetic tape. Simultaneously, two-dimensional spectra without multiplicity information are accumulated in a megastore in 128 energy times 2048 TOF channels. In addition, up to four single spectra for monitoring the neutron flux or the pulse width of the accelerator are recorded as well. Up to 8 samples are cycled into the neutron beam in intervals (typically 10 min), which are defined by integrating the proton beam current to a preselected charge. During each sample change, the two-dimensional spectrum is added to a respective sum file on magnetic disk. In this way, the accumulated sum spectra of all samples can be followed directly throughout the experiment.

Data acquisition is performed by a 32 bit multi-user computer (Data General MV4000) with 8 Mbyte memory, 760 Mbyte disk, and two high density tapes. A 1 Mbyte megastore and an increment unit with 3 independent 32 bit input channels selectable for list and increment mode is used for data input.

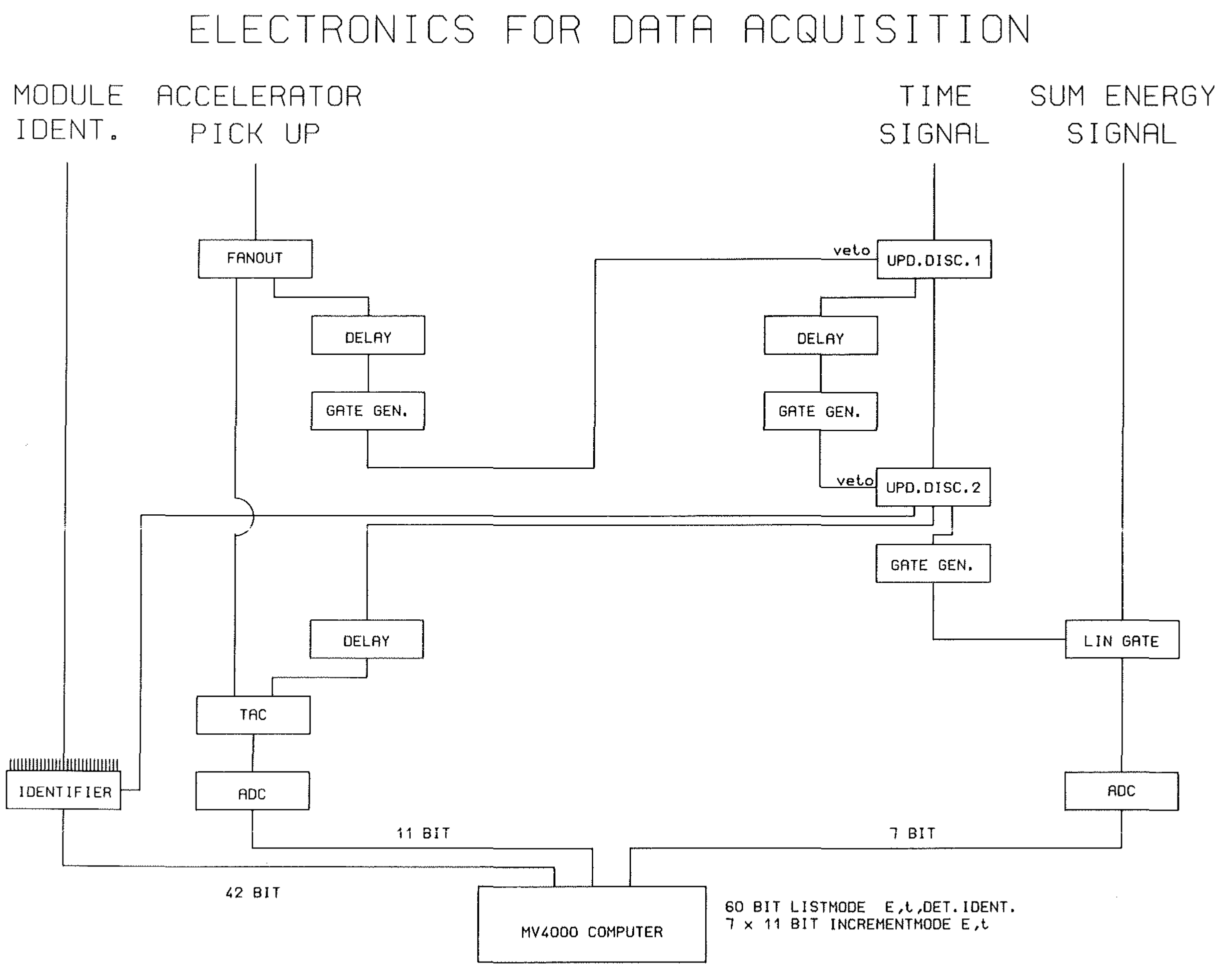

Fig. 31 Electronics for data acquisition.

6. SETTING, CONTROL, AND STABILIZATION OF THE 4π DETECTOR

6.1 SETTING OF INDIVIDUAL PARAMETERS

The detector electronics is controlled by a separate computer (Data General NOVA 4 with 1 Mbyte memory, 73 Mbyte disk, 1600 bpi magnetic tape, and an increment unit for acquisition of single spectra into 32 K of memory) via CAMAC branch driver. The main input-output device is a touch panel display (Kinetic systems). A Silent terminal with paper output is available for documentation. For each detector module a set of 256 parameters is stored on disk; an additional set contains the global parameters of the setup. For all relevant settings , i.e. bias voltage, delay, discriminator thresholds, gain, offset, and gate width, the actual value, a standard value as well as upper and lower limits can be stored simultaneously. This allows to exclude unphysical settings and offers an easy recall of old settings after unsuccessful readjustments. All inputs for individual detector modules are made via touch panel display. There are also routines to set one parameter for all 42 detector modules at a time; this is convenient for fast readjustments of the detector after a power failure or when CAMAC crates have to be modified. Fast changes in the parameter sets can also be made by special editing features.

6.2 AUTOMATIC ADJUSTMENT AND GAIN STABILIZATION

The time consuming energy calibration of the individual detector modules and the adjustments for optimum time resolution are performed by automatic routines.

(i) Adjustment of gain and offset of the linear gates: For obtaining a sum signal with good energy resolution it is important that all detector modules are calibrated to equal values for gain and offset. For this purpose, the sum energy spectrum is measured with a mixed gamma-ray source containing ^{60}Co and ^{137}Cs according to fig. 30. If all but one of the CFDs are blocked by CAMAC commands, the observed "sum" spectrum represents only the single spectrum of the unblocked detector module. After a preselected number of counts are accumulated, the positions of the three prominent gamma-ray lines are roughly obtained by a peaksearch routine, and the exact positions are determined by a gaussian fit of each peak. Fitting the three positions by a straight line according to their energies yields the energy calibration of the spectrum. By an automatic procedure, gain and offset of the linear gate are changed stepwise until the energy calibration agrees with a preselected standard within specified limits. This procedure can be repeated automatically either for all or for a selected number of detector modules.

(ii) Adjustment of the delay for the fast signals: For optimum time resolution, the fast signals have to be adjusted to equal transit times between detector and the 42-fold OR that defines the timing signal for the TOF measurement. This procedure is performed with a ^{60}Co source inside the detector. Via multiplexer, the fast signal of a selected reference module is switched to a separate CFD, which yields the start signal for a TAC; the stop signal is provided by the 42-fold OR. Blocking the CFDs of all 42 detector modules except of the reference module means that the TAC is started and stopped by pulses from the same origin; the position of the resulting peak in the time spectrum can be taken as a reference for all other detector modules. By an automatic procedure, each detector module can successively be combined with the reference module by blocking the CFDs of all other detectors. The position of the corresponding time peak is determined by a gaussian fit; it is then shifted to the correct position by an appropriate delay that can be derived from the known time calibration of the TAC.

(iii) Stabilization of the detector: Compensation for long term variations of the photomultiplier gain and for temperature dependent variations of the light output ($\Delta T = 1$ K changes the pulse height by ~2%) requires a stabilization procedure working on the time scale of hours. For this purpose, the alpha lines of the radium impurities are used as internal standards. The fact that signals from alpha particles do not show a fast component can be used for separating them by pulse shape discrimination. The fast and slow signals of a detector module are selected via multiplexer; the slow signal is transfered to a separate ADC, while the fast signal is fed into two CFDs with high and low threshold, respectively. The output of these discriminators are used to start and stop a TAC as shown in fig. 30. The upper threshold corresponds to the pulse height of the fast component for ~600 keV gamma-rays. Gamma-rays with higher energies exceed both thresholds with very short time difference, giving rise to a sharp peak in the observed time spectrum. The pulses from alpha particles either fall below the upper threshold or pass it with a significant time delay compared to gamma-rays. Hence, the sharp peak due to gamma-rays can be selected by a single-channel-analyser. If the energy spectrum of the detector module is observed in anticoincidence with these gamma-ray signals, an almost background-free alpha particle spectrum is obtained. This is illustrated in fig. 32 showing the spectrum of the mixed $^{60}Co + ^{137}Cs$ source with and without the anticoincidence condition.

From this alpha particle spectrum, the well isolated 7.7 MeV line from the decay of ^{214}Po is used for stabilisation of the 4π detector. Immediately after the settings for gain and offset are found for a particular detector module, the automatic routine described above also records the alpha spectrum for this module, and the position of the 7.7 MeV line is stored. In this way, a definite correlation between the correct gain adjust for the sum energy spectrum and the position of the 7.7 MeV alpha peak is established.

During neutron capture cross section measurements, the alpha spectra of the 42 detector modules are inspected sequentially. If the position of the 7.7 MeV alpha line starts to deviate by more than the shift corresponding to a change of 0.5 V in bias voltage, the setting is changed accordingly. The gain shift as a function of bias voltage has to be determined once by another automatic procedure, and is then stored as a detector parameter. If the determination of the alpha line fails, the change in bias voltage is limited to ± 5 V in order to avoid dangerous misadjustments. As a 1 V change of the bias voltage modifies the pulse height by approximately 2 % (§ 7.4), the energy resolution in the sum spectrum is slightly degraded by this procedure for gain stabilization; smaller voltage steps would require a modification of the respective CAMAC controlled power supplies. Counting times of 5 min are required per detector module to achieve sufficient statistical accuracy for a reliable analysis of the alpha spectra, so that each detector module can be checked every 4 hours.

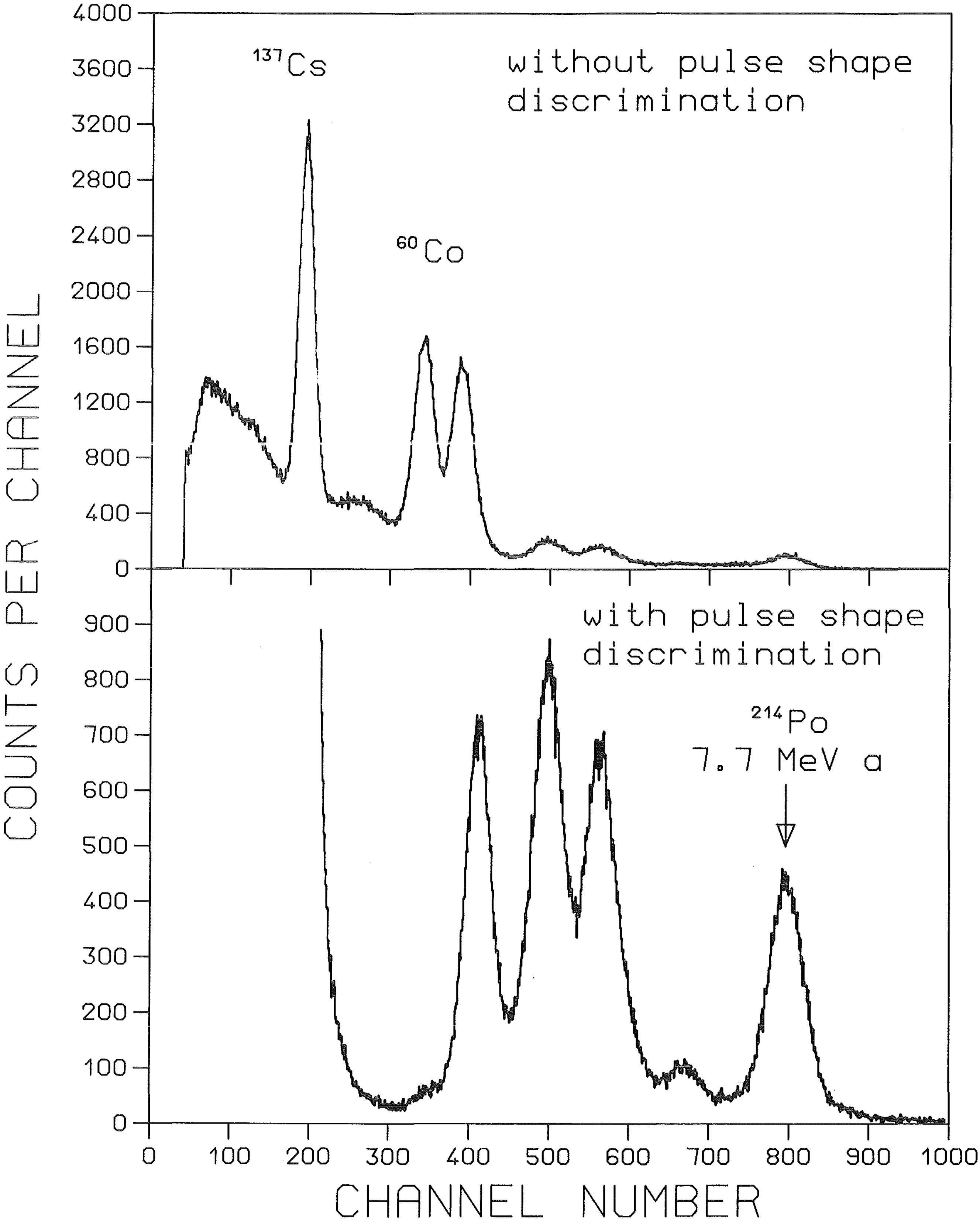

Fig. 32 Spectrum of a mixed $^{137}Cs + ^{60}Co$ source used for calibration of the linear gates (top); the same spectrum taken with pulse shape discrimination (bottom) illustrates the perfect separation of alpha particles.

7. PERFORMANCE OF THE 4π DETECTOR

7.1 ENERGY RESOLUTION

The energy resolution obtained in the sum spectra of the 4π detector including 42 detector modules is documented in fig. 33. Gamma-ray sources of ^{137}Cs, ^{54}Mn, ^{65}Zn, ^{60}Co, and ^{88}Y as well as the 6.1 MeV gamma-ray line from a (^{13}C+Pu) source were used in these measurements. The spectra were obtained by summation of the signals from all detector modules as described in § 5.2. The sum energy signal was amplified in a main amplifier (Ortec 572) that was modified by bridging the second differentiation stage and operating with a shaping time of 3 μs. A pulse stretcher is used to adapt the pulse shape to the ADC (Nuclear Data 582; fixed conversion time 5 μs).

The energy resolution is plotted in the insert of fig. 33, showing a linear $E^{-1/2}$ dependence with a small deviation at 6.1 MeV. In general, the resolution is worse compared to the mean of the individual detector modules (fig.20), where 11.3, 6, and ~5% were obtained at gamma-ray energies of 0.662, 2.5, and 6.1 MeV, respectively. This difference is due to the following reasons:

(i) In general, the linear gates tend to slightly degrade the energy resolution; this effect is enhanced because about 10% of the integrated slow signals are lost due to the gate width of only 3 μs (fig. 16).

(ii) The gated pulses are affected by the constant noise level of 10 mV due to the incomplete decoupling of fast and slow pulses (§ 5.2). This reduces the resolution for the ^{137}Cs line by ~2%, while it is of minor importance at higher energies.

(iii) The detector stabilization operates by changing the bias voltage in steps of ±1 V; this implies a minimum pulse height change of 1.5% on average.

(iv) The energy resolution at high gamma-ray energies suffers also from nonlinearities in the energy calibration, which can be different for individual detector modules. In general, the nonlinearity increases with increasing voltage, and values between 2100 and 2400 V are necessary for achieving equal pulse heights.

(v) The high overall detector efficiency results in high count rates even if relatively weak gamma-ray sources are used. Therefore, pile-up effects start to deteriorate the energy resolution.

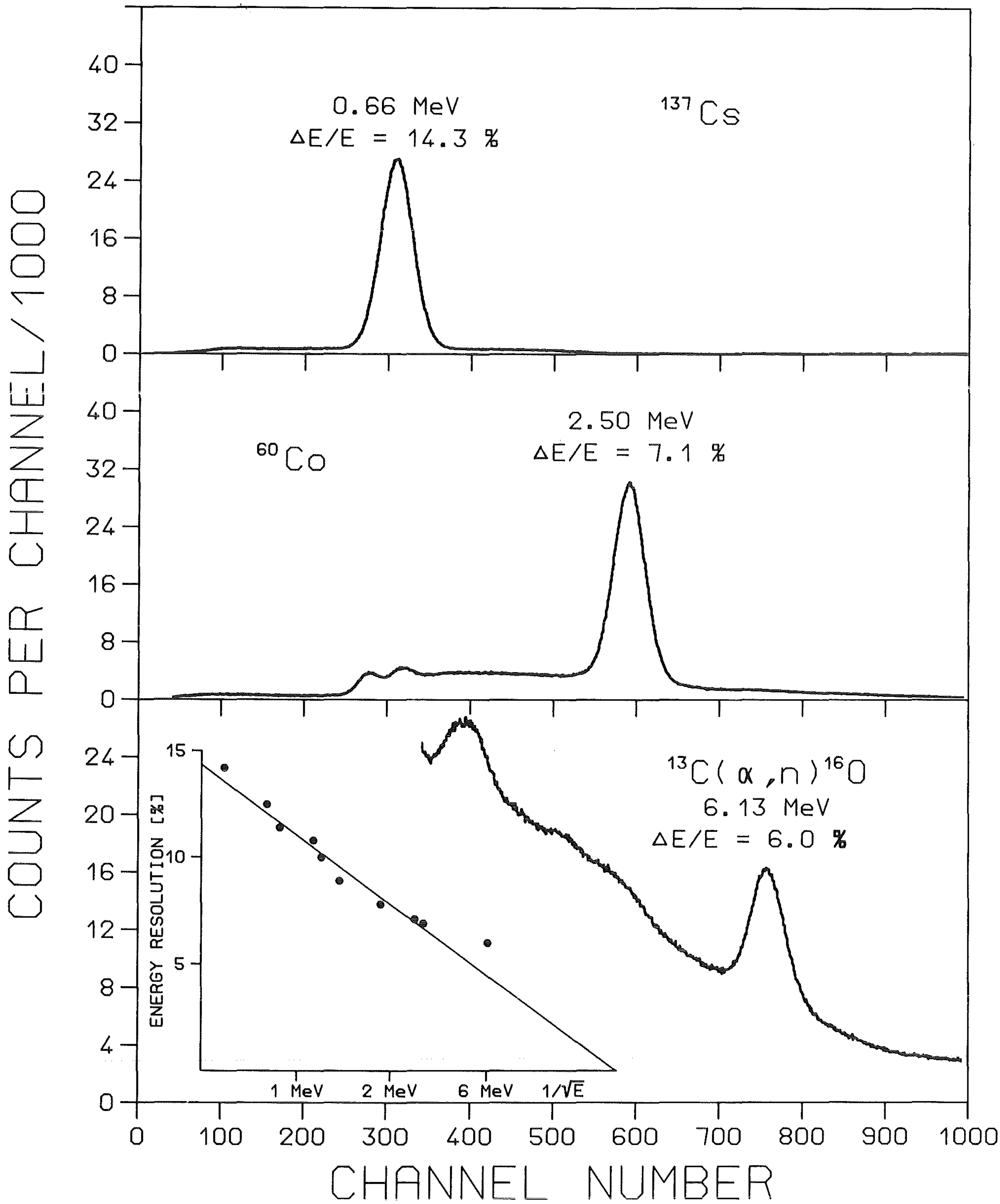

Fig. 33 Energy resolution of the 4π detector in the range from 0.6 to 6.1 MeV (the large background in the lower spectrum is caused by neutrons from the (α,n) reaction).

Further improvements of the energy resolution are expected by decoupling fast and slow signals with additional amplifiers, and by introducing an ADC system for individual pulse height analysis of all detector modules. It is also planned to improve the stability by tuning the gain of the linear gates instead of the bias voltage. A significantly better resolution could finally be achieved by cooling the entire detector to temperatures around 5 °C.

7.2 DETECTOR EFFICIENCY

As all capture cross sections are measured relative to the standard gold cross section, only cross section ratios have to be determined experimentally. Therefore, the absolute detector efficiency is not required with high precision. An absolute calibration of the efficiency were possible, e.g. by observing the gamma-ray lines of very weak sources in coincidence with a well calibrated Ge detector. With the present setup, this would be complicated as long as a single ADC is used for analysing all events from the 4π detector. As low thresholds have to be used for the sum energy, alpha particles cannot not be discriminated, leading to a background rate of about 20 kHz.

Sufficiently precise information on the absolute efficiency could be obtained by means of calibrated gamma-ray sources. The spectra shown in fig. 34 were measured with ^{65}Zn and ^{88}Y sources of about 4 kBq, and with a ^{60}Co source of 37 kBq, all located in the centre of the 4π detector. Starting with the ^{60}Co spectrum, one finds significant pile-up due to the higher activity. Assuming that all events above the sum energy peak at 2.50 MeV are due to pile-up of full energy signals, a 68 % probability for detecting the sum energy of the ^{60}Co cascade is achieved. This corresponds to a peak efficiency of about 82 % for 1.25 MeV photons (which is the mean of the two ^{60}Co energies). The full energy peaks of the individual gamma-rays are observed with an intensity of 1.8 %, corresponding to a probability of 2 % for detecting only one of the transitions. Hence, there is a 2 % probability for photons of 1.17 and 1.33 MeV for leaving the detector without interaction. Assuming the same escape probability for the ^{65}Zn source, the upper spectrum of fig. 34 yields a peak efficiency of 89 %. In the same way, a peak efficiency of 93 % was obtained for 0.66 and 0.83 MeV gamma-rays via ^{137}Cs and ^{54}Mn sources.

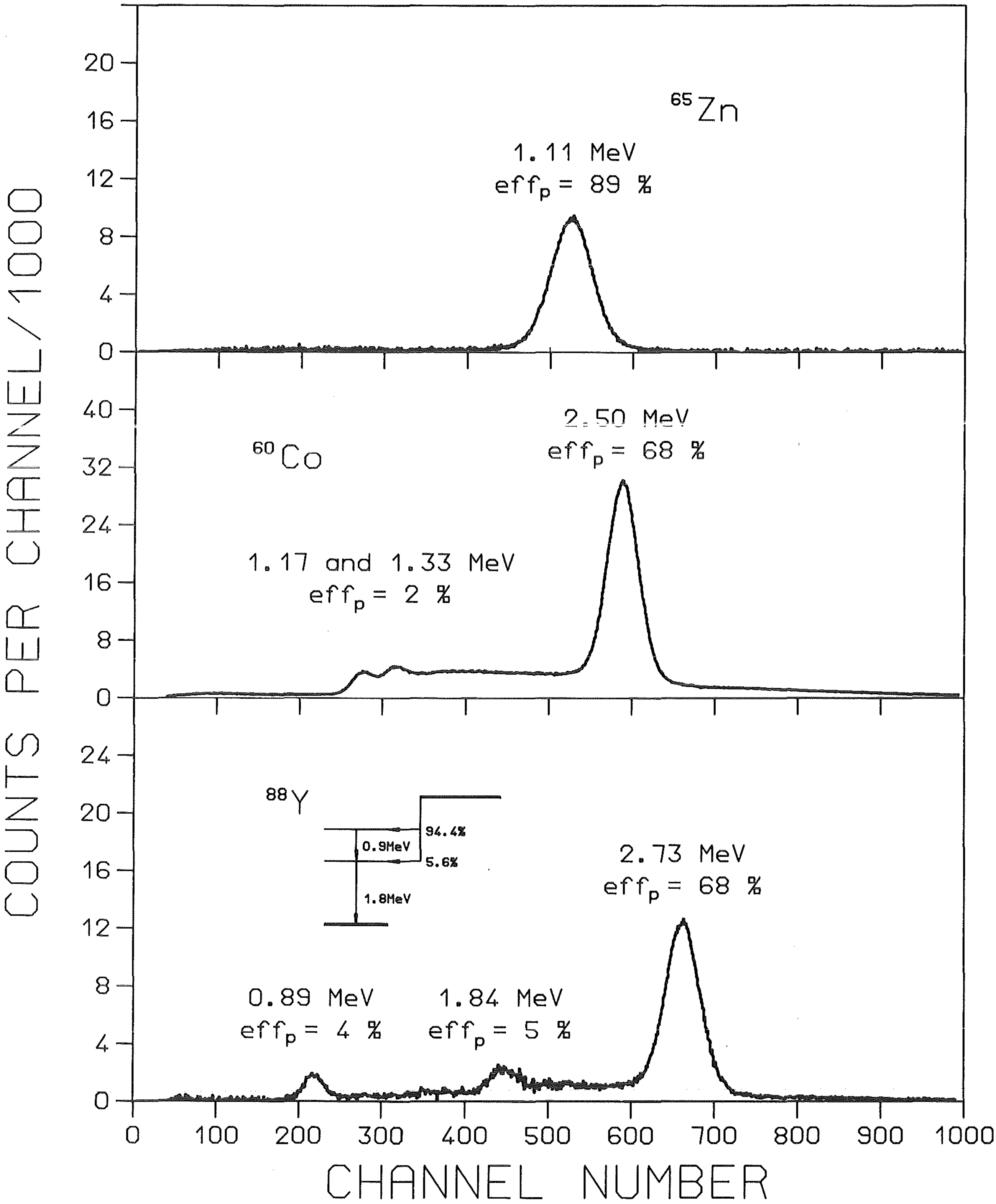

Fig. 34 Pulse height spectra of various gamma-ray sources taken with the 4π detector for determination of the efficiency (the spectra were measured with 42 detector modules covering the full solid angle of 4π).

The sum energy peak in the ^{88}Y spectrum has an intensity of 68 %, corresponding to a 74 % peak efficiency for 1.84 MeV photons. According to the decay scheme indicated in the insert of fig. 34 [39], 5.6 % of all ^{88}Y decays feed the level at 1.84 MeV. The related gamma-rays being not part of a cascade means that they are expected to contribute 4.1% to the 1.84 MeV peak in the spectrum. The observed intensity of 5 % then implies an escape probability of 1 % for the 0.89 MeV photons in the cascade. Finally, the observed 4 % intensity of the 0.89 MeV peak yields directly a 4 % escape probability for the 1.8 MeV photons.

These results are plotted in fig. 35 together with the calculated efficiency values from the design studies (§ 2.3). The peak efficiency was calculated [32] with an optimistic and a pessimistic assumption for treating triple compton scattering events (open circles and triangles in fig. 35). The present results fall between these extremes, but are closer to the optimistic case. The escape probabilities are plotted in the lower part of the figure.

More detailed investigations of the absolute efficiency and the line shape for mono-energetic gamma-rays are planned with a germanium detector for coincidence measurements and using gamma-ray cascades from (p,γ) reactions, which cover a larger energy range.

7.3 TIME RESOLUTION

The time resolution of the detector has been measured with a ^{60}Co source as described in § 6.2 using two different versions of the 42-fold OR. Our first design gave optimal results for two-fold coincidences, but events of higher multiplicity appeared to be systematically shifted in time. As the event multiplicity is recorded as well, this constant shift could later be corrected off-line. In practice, however, it is more convenient to avoid this shift, which was practically eliminated in a second version of the 42-fold OR.

The measured time spectrum is shown in fig. 36, and the measured time resolution is plotted in fig. 37 as a function of the gamma-ray threshold. An optimum resolution of about 650 ps is obtained for threshold energies above 300 keV (fig. 37). The 650 ps represent the total time resolution of the experiment. If the time resolution of

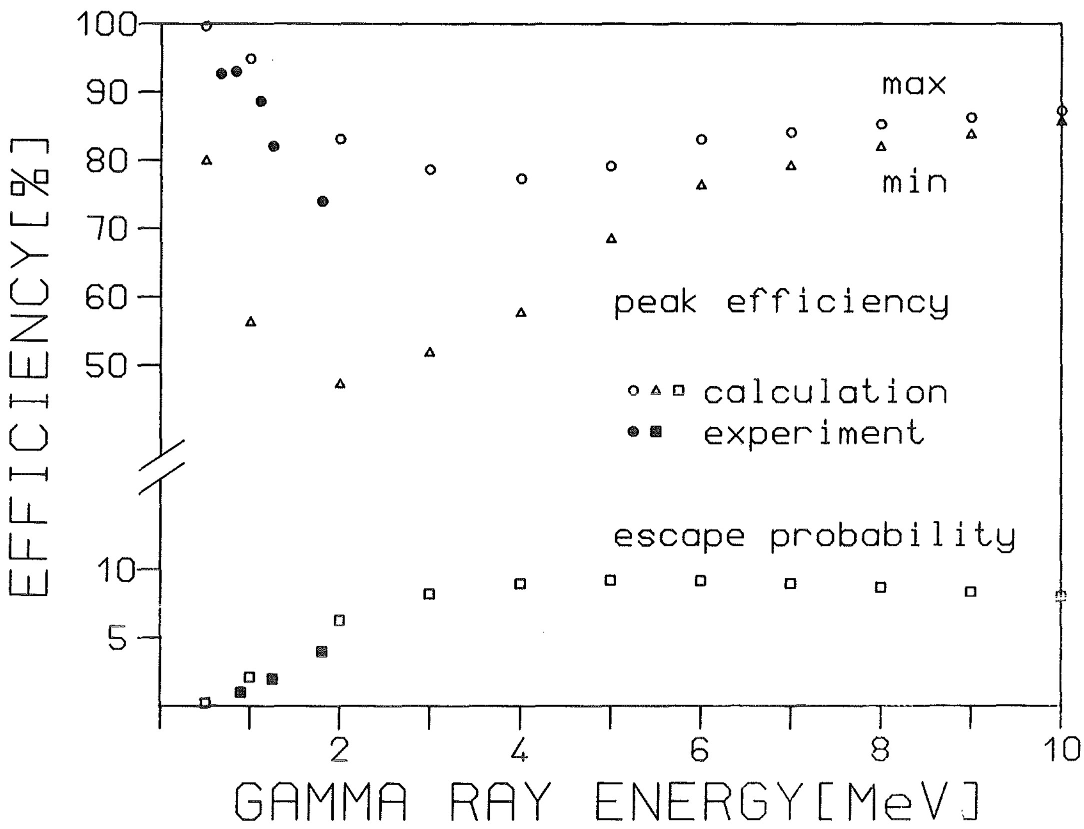

Fig. 35 Measured peak efficiencies and escape probabilities of the 4π detector compared to the calculations of ref.[32]; for details see text.

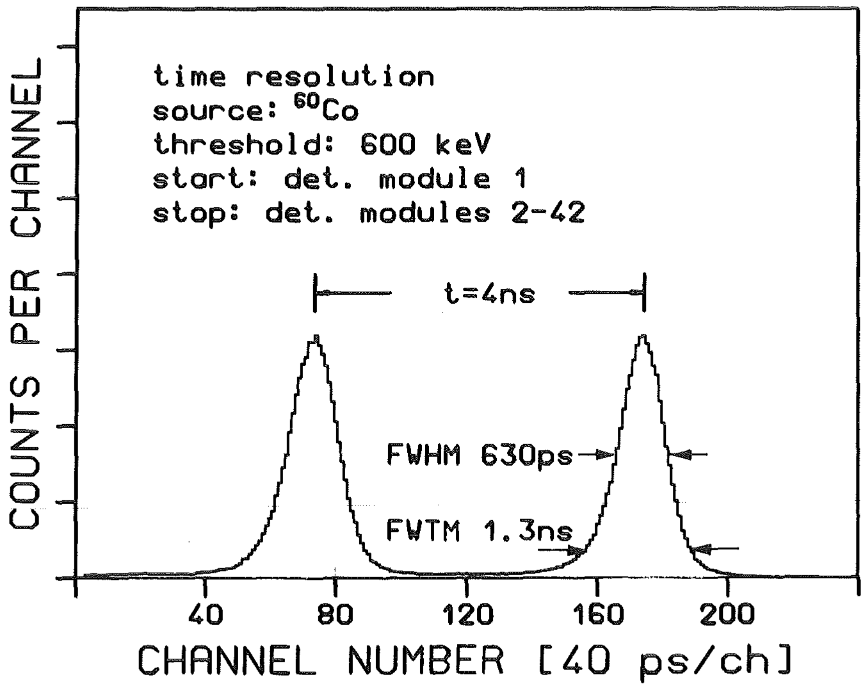

Fig. 36 Optimum time resolution of the 4π detector for two-fold coincidences measured with a ^{60}Co source (start: detector module 1, stop: detector modules 2-42 combined via 42-fold OR).

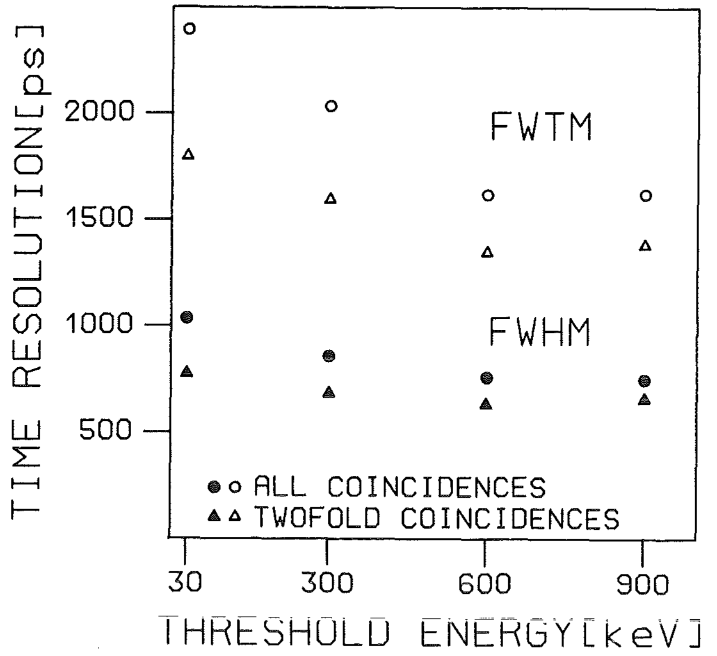

Fig. 37 Time resolution of the 4π detector for two-fold coincidences as well as for all possible multiplicities measured with a ^{60}Co source for different threshold energies in the same way as in fig. 36.

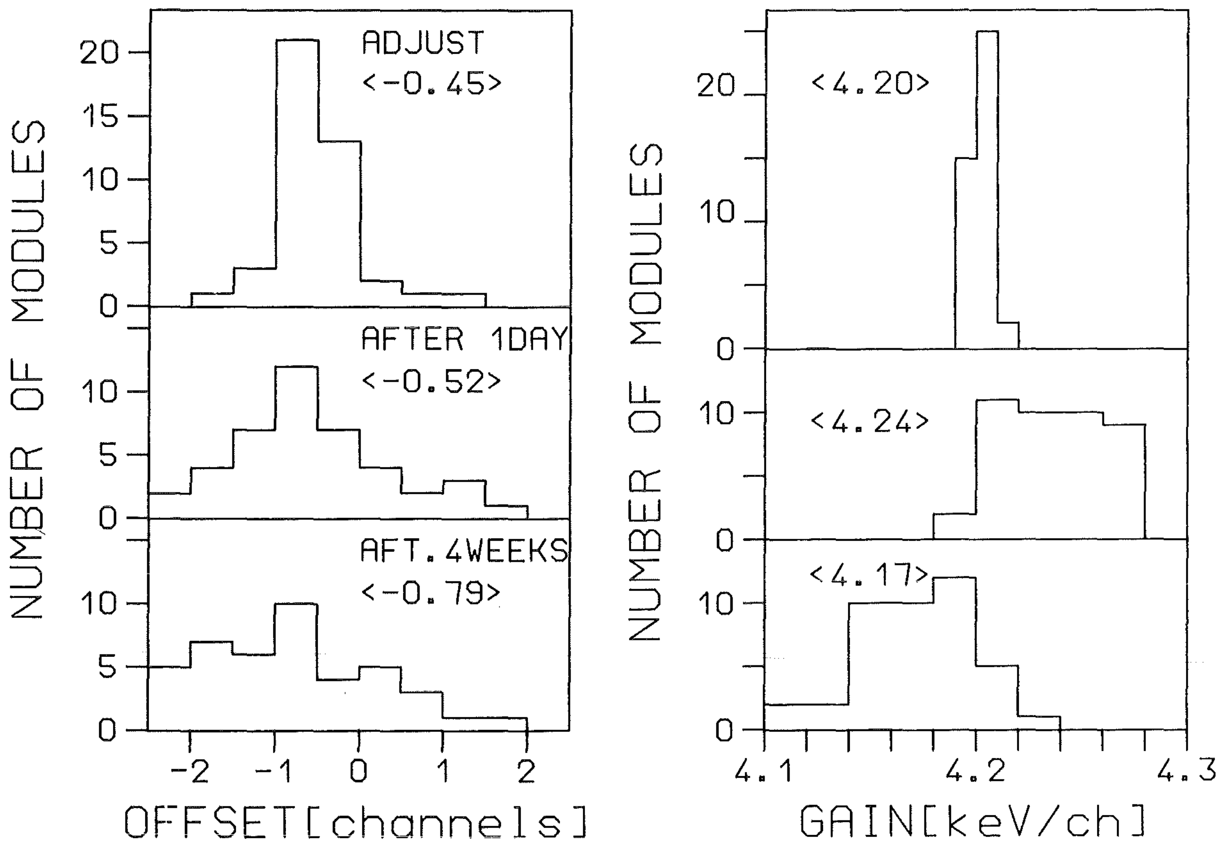

Fig. 38 Offset and gain of the linear gates immediately after adjustment, after a stabilization period of 1 day, and after a measuring period of 1 month; during that time the detector was stabilized via the 7.7 MeV alpha line from radium decay.

the start detector is unfolded, one obtains an overall time resolution of less than 500 ps for the remaining 41 detector modules, an impressive result in view of the 60 l BaF_2 volume.

The results presented in this section demonstrate the attractive features of BaF_2 for gamma-ray detection. For the first time, a 4π detector could be built that combines 7% energy resolution at 2.5 MeV, 500 ps time resolution, and nearly 100% efficiency for gamma-rays up to 10 MeV.

7.4 STABILITY

The stability of the detector settings is demonstrated in fig. 38 showing offset and gain of the 42 detector modules immediately after adjustment, after a stabilization time of 1 day, and after a measuring period of 1 month. During this time, the detector was stabilized by changing the bias voltage as to maintain the position of the 7.7 MeV alpha line (§ 6.2). The gain changes during the first day are due to the fact that the bias voltage can only be changed in steps of ± 1 V. The additional spread during the four weeks of experiment caused only a small reduction in energy resolution (e.g. from 7.3 to 7.8% for the 2.50 MeV ^{60}Co sum peak), which can easily be tolerated.

Table 5. Energy range of continuous neutron spectra produced via the $^7Li(p,n)^7Be$ reaction as a function of proton energy above the reaction threshold at $E_p = 1881$ keV, and related informations.

Proton energy above threshold [keV]	Range of neutron spectrum [keV]	Opening angle of neutron cone [deg]	Energy range undisturbed by scattered neutrons [keV]
0	31	0	31
1	20 - 40	< 5	31 - 40
10	8 - 68	30	53 - 68
20	5 - 88	45	69 - 88
30	5 - 105	60	82 - 105
60	5 - 150	4π	117 - 150
100	5 - 210	4π	164 - 210

8. REGISTRATION OF NEUTRON CAPTURE EVENTS

8.1 NEUTRON SOURCE

The setup for the determination of neutron capture cross sections is briefly described in § 2.1, and a schematic view is given in fig. 2. Neutrons are produced via the $^7Li(p,n)^7Be$ reaction, which indeed is well suited for s-process studies. At the reaction threshold of $E_p = 1.881$ MeV almost monoenergetic neutrons are emitted with an energy of 31 keV, corresponding to the velocity of the compound nucleus. In the centre of mass system, neutrons with practically zero energy are emitted isotropically. Consequently, in the laboratory system all neutrons are emitted in a very narrow forward cone. Rising the proton energy above the reaction threshold yields continuous neutron spectra in an increasingly broader energy range around 31 keV (table 5). Simultaneously, the opening angle of the neutron cone increases, reaching 4π when the proton energy exceeds the reaction threshold by 40 keV.

Energies around 30 keV are also characteristic of the neutron spectrum prevailing during the s-process, which occurs in the helium burning zones of red giant stars. Typical temperatures of these regions are between 200 and 300 million K, corresponding to thermal energies around 25 keV. Neutrons are easily thermalized in the stellar plasma, exhibiting a Maxwellian energy distribution ranging from zero to ~200 keV. Capture cross section measurements should cover this entire range; folding with the stellar spectrum then yields the effective stellar cross section [4]. With the $^7Li(p,n)^7Be$ reaction it is possible to produce neutron spectra in exactly that energy range.

As was shown in § 2.3, the additional 10 cm flight path from the sample to the inner radius of the BaF_2 shell always provides a region at the high energy end of the neutron spectrum that is completely undisturbed by background from sample scattered neutrons. For a flightpath of 77 cm (the minimal flight path that can be presently used) this part of the spectrum is given in the last column of table 5. Obviously, it is possible to move this region over the full spectrum range from 30 to 200 keV by repeated runs at different proton energies. In practice, proton energies should be kept 10 keV above threshold as the neutron yield drops rapidly for lower proton energies, and measurements would be too time consuming.

The possibility to taylor the shape of the neutron spectrum in exactly the energy range that is needed for s-process studies (5-200 keV) is a considerable advantage compared to LINAC sources, where most neutrons are produced at lower and higher energies, so that the related backgrounds disturb the energy range of interest. Moreover, the TOF discrimination of sample scattered neutrons is not possible, as primary flight paths of at least 10 m have to be used in LINAC experiments due to the heavy shield around the neutron target. Hence, the combination of favorable background conditions, short flight paths, and the suited time structure available at Van de Graaff accelerators more than compensate for the lower integral neutron yield. This holds in particular if neutron capture cross sections are to be measured with high precision.

The main parameters of the accelerator are compiled in table 6. The repetition rate of 250 kHz is required to avoid overlap of delayed background events with subsequent pulses.

8.2. MEASUREMENTS AND DATA EVALUATION

Data evaluation and the determination of neutron capture cross sections will be discussed in detail in a forthcoming paper on first measurements with the 4π detector. Here, the relevant features will be presented briefly.

For the determination of neutron capture cross sections relative to a standard, at least four "samples" have to be used in the measurements:

(i) The isotope under investigation: As the neutron capture cross section is characteristic for each isotope, isotopically enriched samples have to be used in order to achieve good accuracy.

(ii) The gold sample: In most cases, the well known neutron capture cross section of gold is used as a standard. However, for some astrophysical problems, it is sufficient to measure the cross section ratio of two neighboring isotopes, e.g. for ^{148}Sm and ^{150}Sm.

(iii) The carbon sample: As neutron capture in carbon is negligible, this sample can be used to simulate the effect of sample scattered neutrons.

(iv) No sample: With an empty sample position, the time independent background due to the radium impurities in BaF_2 and from natural radioactivity is determined together with the backgrounds caused by the neutron beam and by neutrons escaping from the target shield.

The samples are mounted on a sample changer and cycled automatically into the measuring position by a computer controlled stepping motor. Up to 8 samples are fixed on two 0.1 mm thick steel wires to minimize disturbing materials in the neutron beam. The distance between the samples is not fixed, but values between 5 and 10 cm are most appropriate. During the experiments, the samples are changed in intervals of ~10 min, defined by integration of the proton beam current to a preselected charge.

As a rule of thumb, a sample mass of 1 g is required if the 30 keV cross section is ~500 mb; this is considerably less than is normally used in comparable TOF measurements. Correspondingly, sample related uncertainties, e.g. neutron multiple scattering and self-shielding or gamma-ray self-absorption are significantly reduced. Further improvements of the 4π detector (§ 9) will probably allow to use about two times smaller samples.

In the measurements, each event is characterized by a 64 bit data word, containing sum energy, flight time and the detector identification, and is stored in list mode on magnetic tape. Simultaneously, a two-dimensional spectrum of 2048 TOF versus 128 pulse height channels is accumulated in a megastore (without multiplicity information), and up to 4 different control spectra are recorded by a separate increment unit. During the sample change, a new file for the list mode data of the next sample is created on the magnetic tape, and the two-dimensional spectrum is added to a sum file that is stored on disk for each sample separately. The control spectra are also stored on disk for later evaluation. In this way, a two-dimensional spectrum is available for each sample that represents the actual status and that can be used for inspection and control of the ongoing experiment.

Sufficient statistical accuracy is achieved within about 1 to 2 weeks of measuring time for a particular proton energy. The definition of the sample changer intervals by integration of the proton beam current may cause a systematic effect if the neutron yield decreases with time. Then, the first sample in the cycle receives a higher exposure than the last one. This effect can be corrected by means of two control spectra recorded with ^{6}Li glass neutron detectors:

(i) The pulse height spectrum of the first ^{6}Li glass detector (located at a distance of about 20 cm from the lithium target perpendicular to the beam axis) monitors the total neutron yield.

(ii) The second ^{6}Li glass detector (located in the neutron beam behind the 4π detector at a flight path of 2.5 m) is used for taking a TOF spectrum. As this detector is looking at the neutron target through the sample, the recorded spectra have to be corrected for the respective sample transmissions, which are usually larger than 98 %. By this spectrum, neutrons in the direct beam can be distinguished from moderated ones.

The two spectra offer a completely independent normalization for the neutron exposure per sample. The respective corrections are typically ~1 % and can be determined with an accuracy of better than 0.2 %.

For each sample, the list mode data are sorted off-line into two-dimensional spectra according to multiplicity. In general, five spectra per sample containing multiplicities 1 to 4 and ≥5 were found to be sufficient; these spectra differ widely in their signal to background ratios. If necessary, also higher multiplicities can be treated, at the expense of increasing computing time and storage requirements.

The different steps of background subtraction are illustrated in fig. 39. The spectrum on top shows the uncorrected data obtained with a gold sample containing only events with multiplicities larger than two. At low sum energies, the time independent background is mainly due to the radium impurities of the BaF_2 crystals. Capture events in the gold sample are concentrated around 6.5 MeV, while the background due to sample scattered neutrons, which are ultimately captured in barium is mainly located at sum energies of 9 MeV. It is easy to see that the latter component is more strongly spread in time compared to capture events in the gold peak; even after 3 μs this background is still significant. Consequently, accelerator repetition rates of 250 kHz or even lower should be used in actual experiments.

The background from scattered neutrons falls into three components, a constant part due to moderated neutrons escaping from the shield around the target, and two

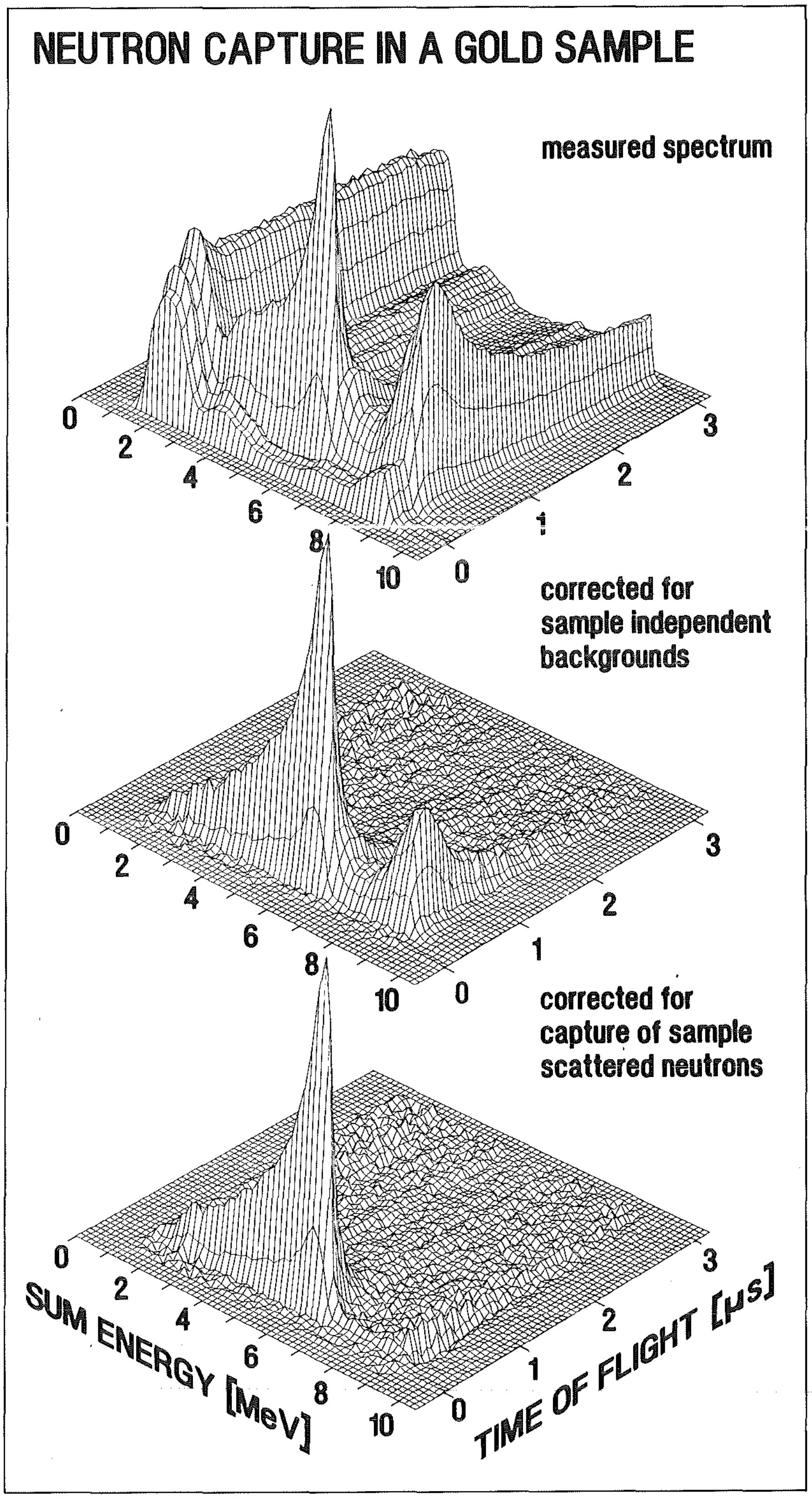

Fig. 39 Two-dimensional spectra of sum energy versus time of flight measured with a gold sample; the various steps of background subtraction are illustrated from top to bottom.

time-dependent parts due to neutrons scattered from the sample or in the air along the flight path through the detector.

The spectrum in the mid part of fig. 39 is obtained after subtraction of background measured without sample, containing only events that are correlated with the sample, i.e. the true capture events around 6.5 MeV sum energy and background due to sample scattered neutrons. The latter component can be accounted for by the properly normalized spectrum measured with the carbon sample, that has been subtracted in the lower part of fig. 39. There, only the true capture events at the 6.5 MeV binding energy of gold are left, which fall in a TOF interval of about 500 ns according to the investigated neutron energy range from 10 to 200 keV (for 77 cm flight path).

The difference in background due to scattered neutrons around 9 MeV, that is observed between the upper and the mid part of fig. 39, indicates that the contributions from scattering in air and in the sample are about equal. Therefore, in future experiments the neutron beam will be guided through the detector in an evacuated flight tube, in order to eliminate air scattering.

The projected sum energy spectrum obtained with the carbon sample is shown in fig. 40. Neutron capture in BaF_2 is dominated by ^{137}Ba and ^{135}Ba with binding energies of 8.6 and 9.1 MeV, respectively. A smaller part due to capture in ^{134}Ba and ^{136}Ba peaks at 6.9 MeV, whereas capture in ^{138}Ba and ^{19}F is almost negligible due to the low capture cross sections of both isotopes. The latter components are problematic as they fall in a sum energy range, where one expects the capture events of gold and of most isotopes of astrophysical interest.

The TOF spectrum of fig. 41 was obtained from the two-dimensional distribution of the gold sample (bottom part of fig. 39) by summation over the energy range around the maximum at 6.5 MeV. The corresponding background due to sample scattered neutrons is included for comparison. Fig. 41 verifies two important features:

(i) The energy range from 150 to 200 keV is free of background (see § 2.3 and table 5).

(ii) Sample scattered background is strongly spread in time, confirming the previous calculation (fig.6).

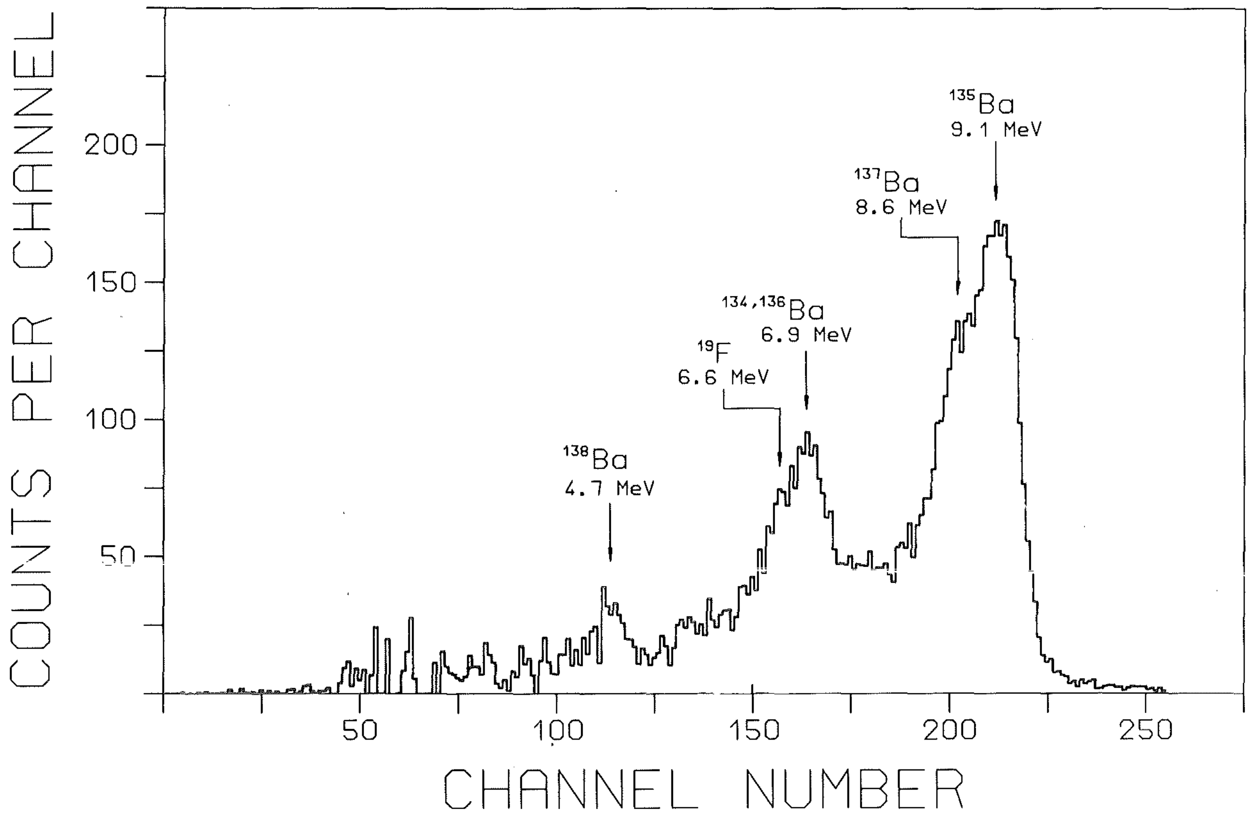

Fig. 40 Sum energy spectrum due to neutron captures in the BaF_2 crystals as measured with a carbon sample. The various components are easily attributed to capture in different barium isotopes.

Table 6. Parameters of the neutron source.

Accelerator:	3.75 MV Van de Graaff
Proton energy:	10 - 100 keV above ^{7}Li(p,n)^{7}Be threshold
Repetition rate:	250 kHz
Pulse width:	$<$1 ns
Beam intensity:	2 µA
Neutron target:	~1.8 mg/cm^2 metallic lithium on water cooled copper or silver backing
Neutron spectrum:	continuous, ranging in energy from 5 keV to an upper limit between 70 and ~210 keV.
Flight path:	77 cm

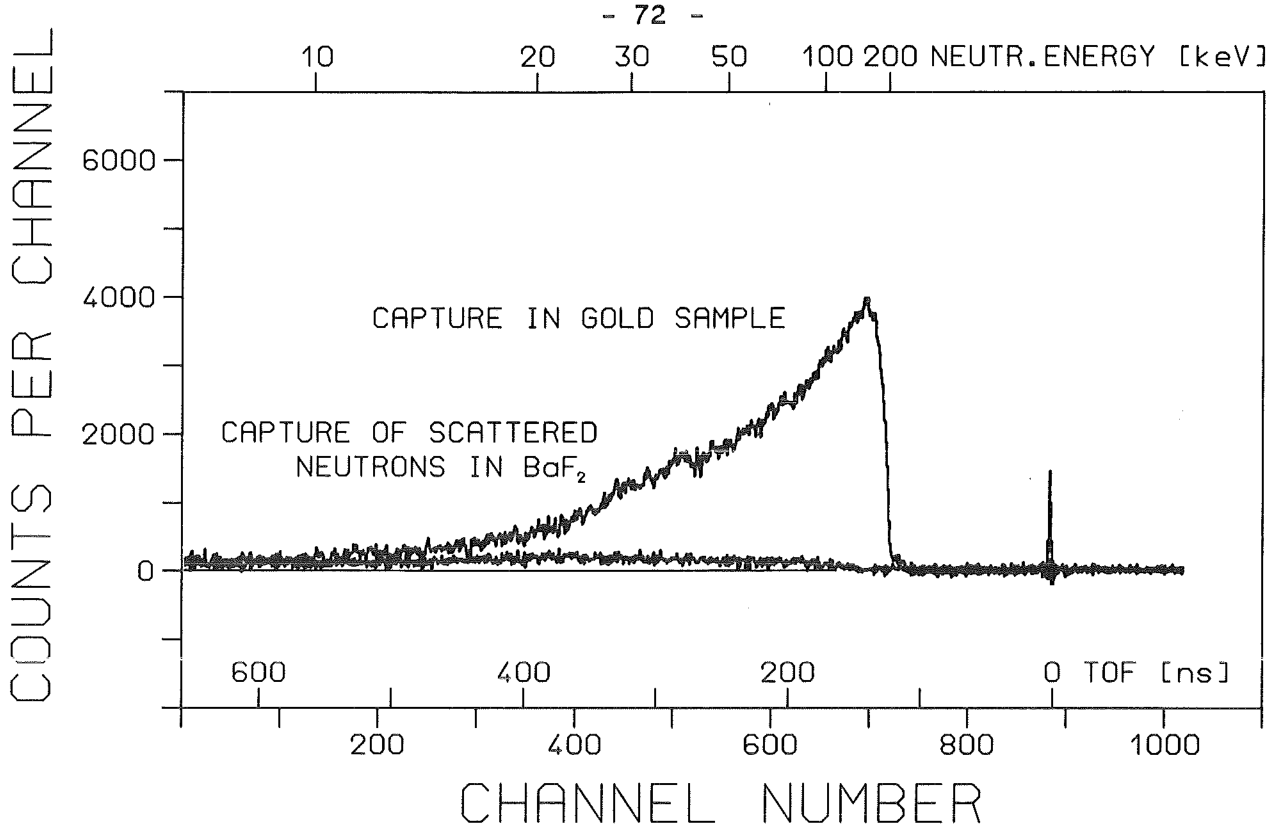

Fig. 41 The net TOF spectrum recorded with a 2 g gold sample in a neutron spectrum ranging from 5 to 200 keV. The background due to sample scattered neutrons that was subtracted before is shown separately. The spectrum was obtained by summation of the pulse height channels around the binding energy (see fig. 42).

(iii) Selecting distinct channels in the sum energy spectrum around the binding energy eliminates most of the background (the calculation in fig. 6 was performed without such selection).

Despite the fact that the cross section ratio for capture and scattering in gold is ~1:20, the measured signal to background ratio is very favorable; even at 10 keV it is still 2:1. Nevertheless, only the energy range above 20 keV will be evaluated from this spectrum, as better signal to background ratios can be obtained at low energies in runs where the maximum neutron energy is restricted to $\leq$ 100 keV.

From the spectrum of fig. 41 only the cross section shape can be evaluated. For normalization, sum energy spectra are calculated by adding the TOF channels in the neutron energy range from 150 to 200 keV, the region with the best signal to background ratio. The resulting spectra for gold and rhodium are shown in fig. 42. In both spectra about 95 % of all capture events are observed above the experimental

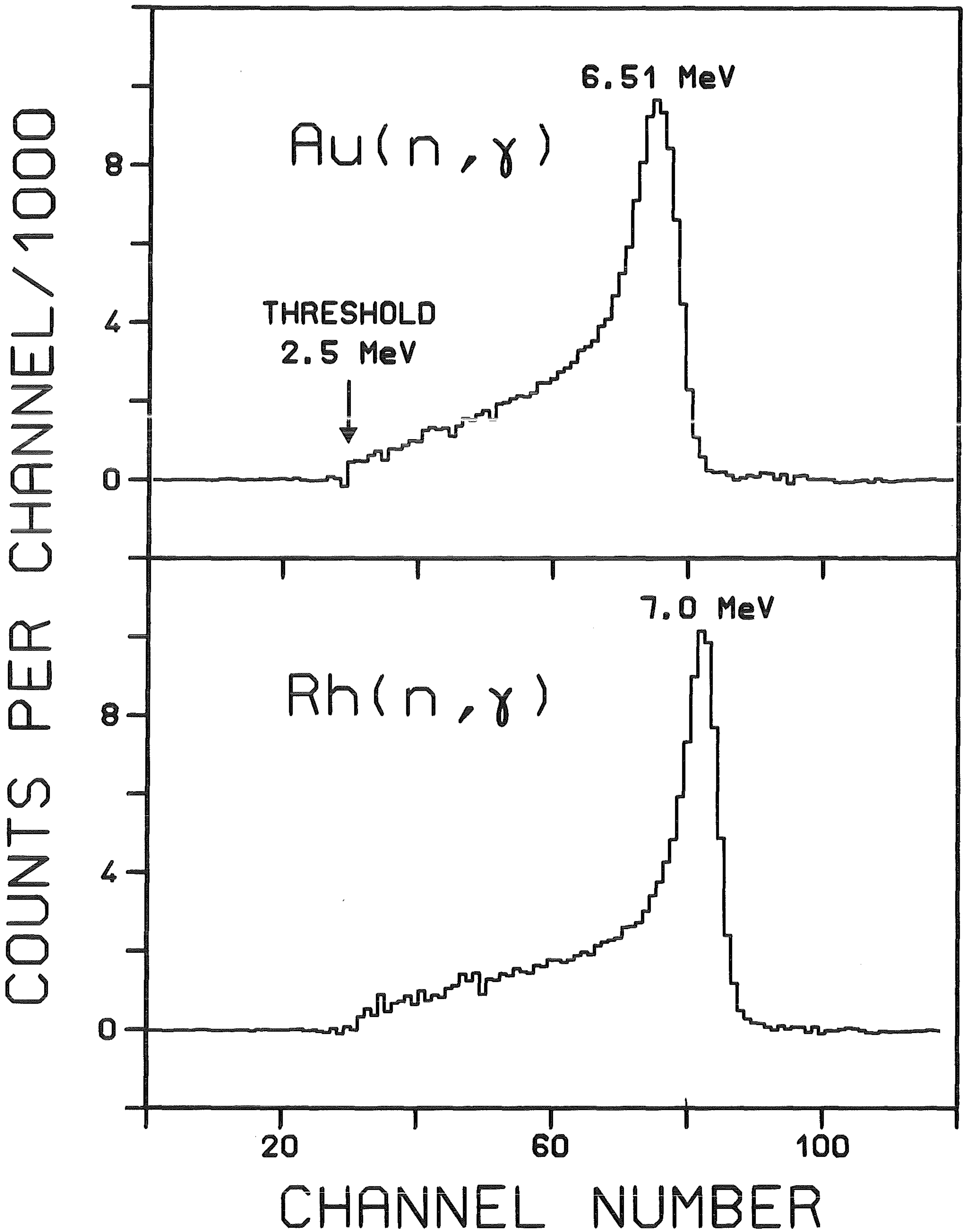

Fig. 42 Sum energy spectra for neutron capture in gold and rhodium. The spectra were obtained by adding the time of flight channels in the neutron energy range from 150 to 200 keV (see fig. 41).

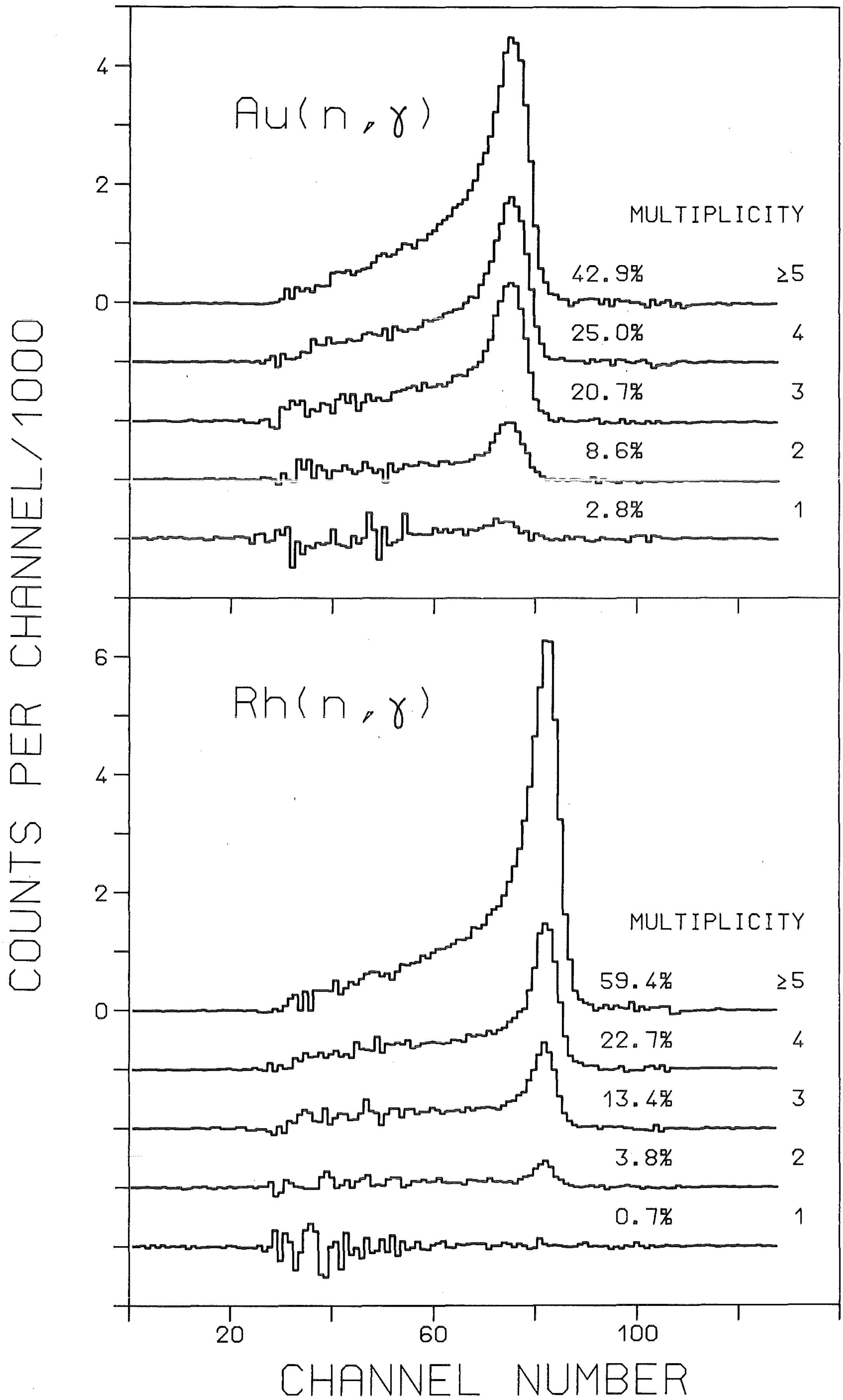

Fig. 43 Sum energy spectra for neutron capture in gold and rhodium for different multiplicities.

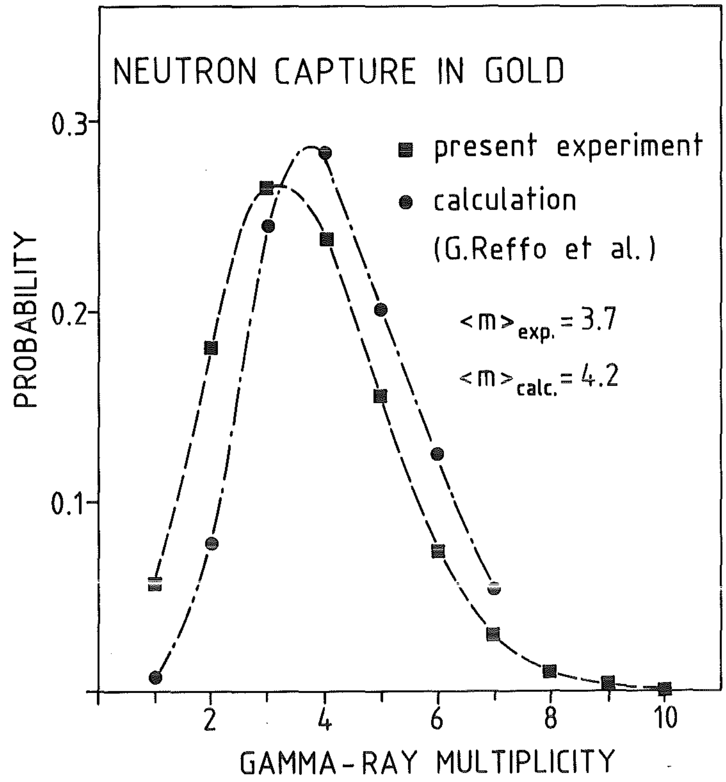

Fig. 44 The uncorrected experimental multiplicity distribution for neutron capture in gold (squares) compared to a previous calculation [16].

threshold of 2.5 MeV. The correction for the cross section ratio σ(Rh)/σ(Au), which results from extrapolation to lower energies is 0.98 with an absolute uncertainty of ± 0.6 %.

The dependence of the observed effect on event multiplicity is shown in fig. 43 for gold and rhodium. About 50 % of all events exhibit multiplicities of five or more, while only 1 to 2 % are observed with multiplicity one. For the gold sample, the measured neutron capture multiplicities are compared in fig. 44 to a theoretical calculation [16]. Reasonable agreement is found if one considers that the experimental results are not yet corrected for detector-detector scattering, for the limited solid angle of that experiment (95 % of 4π), and for the threshold energy of about 60 keV in the gamma-ray detectors that cuts off transitions between the first excited states in gold frequently populated in the calculations.

As discussed in detail [40], the overall accuracy obtained in first cross section measurements on samples of niobium, tantalum, and rhodium is about ± 1.2 %. Several improvements (§ 9) that are realized meanwhile or are under development will allow to exceed this result in the future.

9. CONCLUSIONS

9.1 IMPROVEMENTS

During the first capture cross section measurements on samples of niobium, tantalum, and rhodium relative to a gold standard, the experimental method was studied in detail and several possible improvements were persued for future implementation.

At present, the achieved uncertainty of ± 1.2 % is mainly due to the absolute normalization of the cross section shape. In this step of data analysis, the number of events above the experimental threshold of 2.5 MeV has to be determined including all multiplicities, e.g. from the spectra shown in fig. 43. Although the number of true events with multiplicities 1 or 2 is small, an exact analysis is difficult because of significant statistical fluctuations; these are due to the subtraction of sizeable background from radium impurities in the BaF_2 crystals.

In view of this situation, the following improvements are planned or already realized:
(i) The spectra shown in fig. 43 have been measured with 40 detector modules covering 95% of the full solid angle; two positions were left open for the neutron beam to pass. This means for a capture cascade of multiplicity 4 that there is already a 20% probability that one of the gamma-rays escapes from the detector without hitting a BaF_2 crystal at all. Hence, the number of events in the full energy peak is reduced and the average multiplicity appears too low. A significant fraction of the missing solid angle presently not filled with BaF_2 will be covered in the future by crystals with a central hole of 50 mm diameter for the neutron beam.
(ii) The background from radium impurities was reduced meanwhile by 40% as the eight crystals with the largest radium content were replaced. These new crystals are already included in fig. 26; the two modules with decay rates above 1000 s^{-1} shown there will not be used furtheron.
(iii) The pulsing system of our accelerator is presently modified with the aim to improve the intensity per pulse in the extracted proton beam. Any such improvement will translate linearly in an improved signal to background ratio for that component which is not correlated with the neutron beam.
(iv) Neutron scattering in the air along the 50 cm flight path through the detector will be eliminated by evacuated flight tubes for the neutron beam, thus reducing the respective background significantly.

9.2 SUMMARY

After 30 years of neutron capture cross section measurements with liquid scintillator tanks, Moxon-Rae detectors, and total energy detectors, the potential of these methods seems to be exhausted. Any further improvement can only be achieved by new techniques. An attempt for establishing such a technique was made with the 4π BaF_2 detector using the impressive features of BaF_2 for gamma-ray detection discovered six years ago.

The favorable combination of a Van de Graaff accelerator and the 4π BaF_2 detector for measurements in the keV neutron energy range was discussed in detail. With the $^7Li(p,n)^7Be$ reaction as an efficient source of keV neutrons and with flight paths of less than 1 m, it is well suited for the intended application as neutron production can be restricted exactly to the energy range of astrophysical interest. The setup offers a number of possibilities for background suppression, and the remaining backgrounds can be studied quantitatively. Barium fluoride proved to be the best available scintillator, combining high efficiency, good energy resolution, and excellent timing with a low sensitivity to capture of keV neutrons.

The new method required significant investments for scintillator, electronics, and computers; large amounts of data have to be handled, and painstaking procedures had to be worked out in order to verify each step of data analysis. However, already the first results confirmed that it was worth this effort, and that data with significantly improved accuracy can be expected in the near future.

REFERENCES

[1] C. Chiosi and A. Renzini, eds., Stellar Nucleosynthesis, Proc. of the Third Workshop of the Advanced School of Astronomy of the Ettore Majorana Centre Erice, Italy, May 11-21, 1983 (Reidel, Dordrecht, 1983).

[2] A. Faessler, ed., The Early Universe and its Evolution, Proc. of the Int. School of Nuclear Physics, Erice, Italy, April 2-14, 1986, Progress in Particle and Nuclear Physics, Vol. 17 (Pergamon Press, Oxford, 1986).

[3] C.E.Rolfs and W.S.Rodney, Cauldrons in the Cosmos (University of Chicago Press, Chicago, 1988).

[4] F. Käppeler, H. Beer and K.Wisshak, Rep. Prog. Phys. 52 (1989) 945.

[5] M. Laval, M. Moszynski, R. Allemand, E. Cormoreche, P. Guinet, R. Odru and J. Vacher, Nucl. Instr. and Meth. 206 (1983) 169.

[6] F. A. Beck, Proc. of the Int. Conf. on Instrumentation for Heavy Ion Nuclear Research, Oak Ridge,TN, October 22-25, 1984, D. Shapira, ed. (Harwood Academic,1985) p. 129.

[7] G. V. Muradyan, Yu. V. Adamchuk, Yu. G. Shchepkin and M. A. Voskanyan, Nucl. Sci. Eng. 90 (1985) 60 .

[8] R. C. Block, P. J. Marano, N. J. Drindak, F. Feiner, K. W. Seeman and R. E. Slovacek, Proc. Int. Conf. on Nuclear Data for Science and Technology, May 30-June 3, 1988, Mito, Japan, S. Igarasi, ed. (Saikon, Tokyo, 1988) p. 383.

[9] S. Yamamoto, K. Kobayashi and Y. Fujita, Proc. Int. Conf. on Nuclear Data for Science and Technology, May 30-June 3 , 1988, Mito, Japan, S. Igarasi, ed. (Saikon, Tokyo, 1988) p. 375. and S. Yamamoto, Y. Fujita, T. Shibata and S. Selvi, Nucl. Instr. Meth. A249 (1986) 484.

[10] P. E. Koehler and H. A. O'Brien, Proc. Int. Conf. on Nuclear Data for Science and Technology May 30-June 3, 1988, Mito, Japan, S. Igarasi, ed. (Saikon, Tokyo, 1988) p. 1101.

[11] F. Käppeler, G. Schatz and K. Wisshak, Vorschlag zum Bau eines Wismuth-Germanat-Detektors für Präzisionsmessungen zur Elementsynthese im s-Prozess, report KfK-3472, Kernforschungszentrum Karlsruhe (1983) .

[12] K. Wisshak, F. Käppeler and G. Schatz, Nucl. Instr. and Meth. 221 (1984) 385, and K. Wisshak, F. Käppeler and G. Schatz, Calculated Efficiency of a 4π Detector of BGO or BaF_2 for Monoenergetic Gamma-Rays and Gamma Cascades Following Neutron Capture, report KfK-3580, Kernforschungszentrum Karlsruhe (1983).

[13] K. Wisshak and F. Käppeler, Nucl. Instr. and Meth. 227 (1984) 91.

[14] K. Wisshak, F. Käppeler and H. Müller, Nucl. Instr. and Meth. A251 (1986) 101.

[15] K. Wisshak, K. Guber and F. Käppeler, Nucl. Instr. and Meth. A259 (1987) 583.

[16] G. Reffo, F. Fabbri, K. Wisshak and F. Käppeler, Nucl. Sci. Eng. 80 (1982) 630.

[17] K. Wisshak, F. Käppeler, G. Reffo and F. Fabbri, Nucl. Sci. Eng. 86 (1984) 168.

[18] B. C. Diven, J. Terrell and A. Hemmendinger, Phys. Rev. 120 (1960) 556.

[19] D. Kompe, Nucl. Phys. A133 (1969) 513.

[20] M. C. Moxon and E. R. Rae, Nucl. Instr. and Meth. 24 (1963) 445.

[21] F. Corvi, C. Bastian and K. Wisshak, Nucl. Sci. Eng. 93 (1986) 348.

[22] R. L. Macklin and J. H. Gibbons, Phys. Rev. 159 (1967) 1007.

[23] F. Käppeler, K. Wisshak and L. D. Hong, Nucl. Sci. Eng. 84 (1983) 234.

[24] F. Corvi, A. Prevignano, H. Liskien and P. B. Smith, Nucl. Instr. and Meth. A265 (1988) 475.

[25] R. L. Macklin, Nucl. Sci. Eng. 83 (1983) 309.

[26] R. L. Macklin, Nucl. Sci. Eng. 95 (1987) 200.

[27] Z. Y. Bao and F. Käppeler, Atomic Data and Nuclear Data Tables 36 (1987) 411.

[28] M. Yoshimori, H. Watanabe and F. Shiraishi, Nucl. Instr. and Meth. A245 (1986) 191.

[29] D. J. Wagenaar, N. R. Roberson, H. R. Weller and D. R. Tilley, Nucl. Instr. and Meth. A234 (1985) 109.

[30] P. E. Koehler, S. A. Wender and J. S. Kapustinsky, Nucl. Instr. and Meth. A242 (1986) 369.

[31] D. J. Morrissey, S. H. Wernig and R. A. Blue, Nucl. Instr. and Meth. 221 (1984) 641.

[32] G. Schatz and J. Oehlschläger, Ein Programm zur Berechnung der Ansprechwahrscheinlichkeit eines 4π-Szintillationszählers, report KfK-3710, Kernforschungszentrum Karlsruhe (1984).

[33] K. Wisshak, J. Wickenhauser, F. Käppeler, G. Reffo and F. Fabbri, Nucl. Sci. Eng. 81 (1982) 396 .

[34] M. Jääskeläinen, D. G. Sarantites, R. Woodward, F. A. Dilmanian, J. T. Hood, R. Jääskeläinen, D. C. Hensley, M. L. Halbert and J. H. Barker, Nucl. Instr. and Meth. 204 (1983) 385.

[35] D. Habs, F. S. Stephens and R. M. Diamond, A proposal for a Crystal-Ball Detector System, report LBL-8945, Lawrence Berkeley Laboratory (1979).

[36] E. Malwitz, Crystalball-Trägerkugel Konstruktion und Fertigung, report GSI 80-6, Gesellschaft für Schwerionenforschung, Darmstadt (1980).

[37] D. F. Anderson and D. C. Lamb, Nucl. Instr. and Meth. A260 (1987) 377.

[38] R. Novotny, R. Riess, R. Hingmann, H. Ströhner, R.D. Fischer, G. Koch, W. Kühn, V. Metag, R. Mühlhans, U. Kneissl, W. Wilke, B. Hans, J.P. Vivien, R. Beck, B. Schoch and Y. Schulz, Nucl. Instr. and Meth. A262 (1987) 340.

[39] H.-W. Müller, Nuclear Data Sheets 54 (1988) 1.

[40] K. Wisshak et al., in preparation.

APPENDIX A

A FORTRAN code for Monte Carlo simulation of neutron scattering from the capture sample

```
//IAK554F4 JOB (0554,145,POAOB),WISSHAK,NOTIFY=IAK554,TIME=5
// EXEC F7CLG,PLOT=VERSATEC
//C.SYSPRINT DD DUMMY
//C.SYSIN DD DISP=SHR,DSN=TSO554.WBALL4.FORT
// DD DISP=SHR,DSN=TSO554.PLOT2.CNTL
//L.SYSPRINT DD DUMMY
//L.SYSIN DD *
 ENTRY MAIN
//G.SYSIN DD *
         9     10000           0           0
10.        25.       1.
0.         1.
 1.680E+22137.       19.0       0.        1.         2.          0.
25.        19.       0.
80.
70.        80.       5.         1.126     10.
60.        70.       50.        1.209     10.
50.        60.       100.       1.314     10.
40.        50.       100.       1.453     10.
30.        40.       100.       1.647     10.
20.        30.       83.        1.949     10.
15.        20.       57.        2.330     10.
10.        15.       40.        2.757     10.
5.         10.       26.        3.559     10.
```

```
0.1        1.535     6.5
0.103      1.535     100.
0.106      1.535     6.5
0.273      0.82      6.4
0.283      0.80      50.
0.293      0.78      6.4
0.40       0.64      7.0
0.419      0.62      40.
0.437      0.60      8.0
1.0        0.36      8.0
5.0        0.13      7.7
10.0       0.086     7.4
15.0       0.067     7.0
20.0       0.060     6.8
31.6       0.049     5.5
32.4       0.048     20.
33.2       0.047     8.0
50.        0.039     5.0
51.8       0.038     15.
52.7       0.037     7.0
70.        0.0325    6.5
71.7       0.032     15.
73.4       0.0315    6.5
100.       0.027     6.0
120.       0.025     5.5
0.1        0.001     3.9
0.5        0.0006    3.75
1.0        0.0003    3.7
5.0        0.0002    3.6
10.0       0.0001    3.5
20.0       0.0004    3.5
25.0       0.002     4.0
27.5       0.200     50.0
30.0       0.001     4.0
40.0       0.0005    3.5
42.5       0.03      4.0
45.0       0.002     4.5
50.0       0.04      40.0
55.0       0.0007    4.5
60.0       0.0005    3.3
75.0       0.0005    3.3
90.0       0.002     10.
100.0      0.006     25.0
115.0      0.001     7.0
0.1        0.0       0.0
//PLOTPARM DD *
 &PLOT MODE=0,IOMASK=10 &END
//PL EXEC SVPLOT
```

```
C
C   PROGRAMM ZUM BERECHNEN DER NEUTRONENEMPFINDLICHKEIT
C   VON BGO BAF NAJ
C
      COMMON NUNT,NOB,N,M,IY,DENSTY,ESIG,SIGC,SIGN,AI1,AI2,AI3
      DIMENSION NOUT(100),NCAP(100),NIN(100),
     1ESIG(3,100),SIGC(3,100),SIGN(3,100),
     2E(100),XX(100),YY(100),ZZ(100),TT(100),SS(100),
     3STETA(100),SPHI(100),R(100),
     4RMATRX(3,3),SIGANZ(3),
     5NTIMEI(200),NTIMEO(200),NTIMEC(200),NENOUT(100),NENIN(100),
     6NENCAP(100),IFELD(10,12),OFELD(20,5),ENEIN(200)
      DIMENSION ENECAP(1000),ENEOUT(1000),UNTCAP(200),EFFEKT(200),
     1ELOWER(20),EUPPER(20),FLUSS(20),SIGMAG(20),FAKTOR(20),
     2TIMELO(20),TIMEUP(20),UNTOUT(200),
     3MTIMEO(20,200),MTIMEC(20,200),MENOUT(20,100),MENCAP(20,100)
      DIMENSION XXX(200),IBUF(8000),YYY(200)
C.... DIMENSION PPS2(100),PPTETA(100),PPPHI(100),PPAAA(100)
C
C     EINLESEN DER ANFANGSWERTE
C
      READ(5,400)NENER,NEUTRS,NUNT,NOB
      READ(5,401)RIN,ROUT,RPROB
      READ(5,401)GRENZ1,GRENZ2
      READ(5,402)DENSTY,AA1,AA2,AA3,AI1,AI2,AI3
      READ(5,401)SIGANZ(1),SIGANZ(2),SIGANZ(3)
      WRITE(6,403)NENER,NEUTRS,NUNT,NOB
      WRITE(6,404)RIN,ROUT,RPROB
      WRITE(6,405)GRENZ1,GRENZ2
      WRITE(6,406)DENSTY,AA1,AA2,AA3,AI1,AI2,AI3
      WRITE(6,407)SIGANZ(1),SIGANZ(2),SIGANZ(3)
  400 FORMAT(4I10)
  401 FORMAT(3F10.5)
  402 FORMAT(E10.3,6F10.2)
  403 FORMAT('1 ANZENERGIE,ANZNEUTRONEN,FLAGN,FLAGM',4I10)
  404 FORMAT('  RIN,ROUT,RPROB  ',3F10.2)
  405 FORMAT('  GRENZE FUER ZUFALLSZAHLEN    ',2F10.4)
  406 FORMAT('  MOLEK/CM3,MASSE1,2,3,HAUFIGKEIT1,2,3  ',E10.3,6F10.2)
  407 FORMAT('  ANZAHL DES STUETZSTELLEN FUER SIGMA  ',3F10.2)
C
C     EINLESEN DER ENERGIEBEREICHE ETC
C
      DO 124 I=1,10
      TIMELO(I)=0.
      TIMEUP(I)=0.
      ELOWER(I)=0.
      EUPPER(I)=0.
      FLUSS(I)=0.
      FAKTOR(I)=0.
      SIGMAG(I)=0.
  124 CONTINUE
      READ(5,401)FLUGW
      WRITE(6,513)FLUGW
  513 FORMAT(' FLUGWEG IN CM  ',F10.5)
      DO110 K=1,NENER
      READ(5,510)ELOWER(K),EUPPER(K),FLUSS(K),SIGMAG(K),FAKTOR(K)
```

```
  510 FORMAT(5F10.5)
      WRITE(6,511)ELOWER(K),EUPPER(K),FLUSS(K),SIGMAG(K),FAKTOR(K)
  511 FORMAT(' ELOWER,EUPPER,FLUSS,SIGMAG,FAKTOR  ',5F10.5)
  110 CONTINUE
C
C     ANFANGSWERTE SETZEN UND FELDER NULLEN
C
      IY=37
      PIPI=3.14159
      TTT=22.861
      QRIN=RIN**2
      QROUT=ROUT**2
      QRPROB=RPROB**2
C.....TEST FUER ZUFALLSZAHLEN
C     DO 100 K=1,100
C     NOUT(K)=0
C 100 CONTINUE
C     DO 102 K=1,1000000
C     PPP=RANDOM(0.)
C     IPPP=PPP*100.
C     IPPP=IPPP+1
C     IF(IPPP.GT.100)IPPP=100
C     NOUT(IPPP)=NOUT(IPPP)+1
C 102 CONTINUE
C     WRITE(6,408)(NOUT(K),K=1,100)
C 408 FORMAT(' ',10I10)
C.....TEST ENDE
C
C     FELDER FUER BERECHNUNG DER UNTERGRUNDSPEKTREN NULLEN
C
      DO111 I=1,10
      DO111 K=1,100
      MTIMEO(I,K)=0
      MTIMEC(I,K)=0
      MTIMEO(I,100+K)=0
      MTIMEC(I,100+K)=0
      MENOUT(I,K)=0
  111 MENOUT(I,K)=0
      DO 116 K=1,200
      UNTCAP(K)=0.
      EFFEKT(K)=0.
  116 UNTOUT(K)=0.
      DO 122 K=1,1000
      ENECAP(K)=0.
  122 ENEOUT(K)=0.
C
C     EINLESEN DER WIRKUNGSQUERSCHNITTE
C
      DO 2 I=1,3
      ISIG=SIGANZ(I)
      DO 4 K=1,ISIG
      READ(5,501)ESIG(I,K),SIGC(I,K),SIGN(I,K)
      WRITE(6,501)ESIG(I,K),SIGC(I,K),SIGN(I,K)
    4 CONTINUE
    2 CONTINUE
  501 FORMAT(7F10.4)
C.....
```

```
C
C     EINLESEN DER ZUFALLSZAHLEN
C
C     READ(5,502)(PPS2(K),K=1,10)
C     READ(5,502)(PPTETA(K),K=1,10)
C     READ(5,502)(PPPHI(K),K=1,10)
C     READ(5,502)(PPAAA(K),K=1,10)
C 502 FORMAT(10F7.5)
C     WRITE(6,504)
C 504 FORMAT(' EINGEGEBENE ZUFALLSZAHLEN   ')
C     WRITE(6,503)(PPS2(K),K=1,10)
C     WRITE(6,503)(PPTETA(K),K=1,10)
C     WRITE(6,503)(PPPHI(K),K=1,10)
C     WRITE(6,503)(PPAAA(K),K=1,10)
C 503 FORMAT(' ',10F10.5)
C.....
C
C     BEGINN EINER DO SCHLEIFE UEBER ANZAHL DER ENERGIEPUNKTE
C
      DO 4444 L=1,NENER
      EN0=(ELOWER(L)+EUPPER(L))/2.
      WRITE(6,512)L,EN0
  512 FORMAT('1'/' L NEUTRONENENERGIE   ',I10,F10.5)
      NNN=0
      DO1 K=1,100
      NOUT(K)=0
      NCAP(K)=0
      NIN(K)=0
      NTIMEO(K)=0
      NTIMEC(K)=0
      NTIMEI(K)=0
      NTIMEO(100+K)=0
      NTIMEC(100+K)=0
      NTIMEI(100+K)=0
      NENOUT(K)=0
      NENCAP(K)=0
    1 NENIN(K)=0
C
C     BEGINN DER DO SCHLEIFE UBER DIE ANZAHL DER NEUTRONEN
C
      DO 1000 N=1,NEUTRS
      KCC=0
      KKK=0
      KPP=0
      MMM=0
      DO 5 K=1,100
      E(K)=0.
      XX(K)=0.
      YY(K)=0.
      ZZ(K)=0.
      TT(K)=0.
      SS(K)=0.
      STETA(K)=0.
      SPHI(K)=0.
    5 R(K)=0.
C
C     INTERPOLIEREN DER QUERSCHNITTE UND BERECHNEN DER FREIEN WEGLAENGE
```

```
C       UND WECHSELWIRKUNGSWARSCHEINLICHKEITEN FUER DIE ERSTE WW
C
        CALL B10H14(EN0,PATH0,PS1,PS2,PS3)
CC....FUER TESTZWECKE FREIE WEGLAENGE FIX
CC      PATH0=2.
CC.....
        IF(N.LE.NOB.AND.N.GE.NUNT)WRITE(6,671)EN0,PATH0,PS1,PS2,PS3
  671 FORMAT('  EN0,PATH0,PS1,PS2,PS3  ',5F10.3)
C
C       BERECHNUNG DES ORTES DER ERSTEN WW
C
C.....TEST OB S2 WIRKLICH EXPONENTIELL VERTEILT IST
C       DO 6 K=1,100
C       E(K)=-PATH0*ALOG(RANDOM(0.))
C     6 CONTINUE
C       WRITE(6,410)(E(K),K=1,100)
C 410 FORMAT(' ',10F10.5)
C       DO 7 K=1,100
C     7 E(K)=0.
C.....TEST ENDE
        PPP=RANDOM(0.)
CC..    PPP=PPS2(1)
        IF(PPP.LT.GRENZ1)PPP=GRENZ1
        IF(PPP.GT.GRENZ2)PPP=GRENZ2
        S2=-PATH0*ALOG(PPP)
        IF(N.GE.NUNT.AND.N.LE.NOB)WRITE(6,411)PPP,S2
  411 FORMAT(' ZUFALLSZAHL UND ERSTES S2  ',2F10.5)
        X2=0.
        Y2=0.
        Z2=RIN+S2
        E(1)=EN0
        XX(1)=0.
        YY(1)=0.
        ZZ(1)=RIN+S2
        TT(1)=TTT*ZZ(1)/SQRT(E(1))
        R(1)=RIN+S2
        SS(1)=S2
        STETA(1)=0.
        SPHI(1)=0.
        IF(S2.LE.(ROUT-RIN))GOTO 12
C
C       UBERHAUPT KEINE WW IN KUGEL
C
        NOUT(1)=NOUT(1)+1
        TT(1)=TTT*ROUT/SQRT(E(1))
        M=1
        KKK=1
        MMM=1
        IF(N.GE.NUNT.AND.N.LE.NOB)WRITE(6,409)TT(1)
  409 FORMAT(' NEUTRON HAT KUGEL VERLASSEN VOR ERSTER WW,ZEIT:',F10.5)
        GOTO 1111
C
C       AUSWUERFELN OB ERSTE WW STREUUNG ODER CAPTURE
C
   12 PPP=RANDOM(0.)
        IF(PPP.LT.GRENZ1)PPP=GRENZ1
```

```
      IF(PPP.GT.GRENZ2)PPP=GRENZ2
CC.12 PPP=PPAAA(1)
      IF(N.GE.NUNT.AND.N.LE.NOB)WRITE(6,412)PPP
  412 FORMAT(' ZUFALLSZAHL FUER ERSTE WW  ',F10.5)
      IF(PPP.LE.PS1)GOTO 15
      IF(PPP.LE.PS2)GOTO 16
      IF(PPP.LE.PS3)GOTO 17
C
C     EINFANG NACH ERSTER WW
C
      NCAP(1)=NCAP(1)+1
      KCC=1
      MMM=1
      M=1
      GOTO 1111
   15 AAA=AA1
      GOTO 20
   16 AAA=AA2
      GOTO 20
   17 AAA=AA3
   20 DO 31 I=1,3
      DO 31 J=1,3
   31 RMATRX(I,J)=0.
      DO 32 I=1,3
   32 RMATRX(I,I)=1.
C
C     BEGIN DER DOSCHLEIFE UBER BIS ZU 100 STREUUNGEN
C
      DO 2222 M=2,100
      X1=XX(M-1)
      Y1=YY(M-1)
      Z1=ZZ(M-1)
      PPP=RANDOM(0.)
      IF(PPP.LT.GRENZ1)PPP=GRENZ1
      IF(PPP.GT.GRENZ2)PPP=GRENZ2
CC... PPP=PPTETA(M)
      THETA=PIPI*PPP
      IF(N.GE.NUNT.AND.N.LE.NOB)WRITE(6,413)N,M,PPP,THETA
  413 FORMAT(' ',2I10,'  ZUFALLSZAHL UND THETA  ',2F10.5)
      PPP=RANDOM(0.)
      IF(PPP.LT.GRENZ1)PPP=GRENZ1
      IF(PPP.GT.GRENZ2)PPP=GRENZ2
CC... PPP=PPPHI(M)
      PHI=2.*PIPI*PPP
      IF(N.GE.NUNT.AND.N.LE.NOB)WRITE(6,414)N,M,PPP,PHI
  414 FORMAT(' ',2I10,'  ZUFALLSZAHL UND PHI  ',2F10.5)
      EN=E(M-1)
C
C     BERECHNUNG DER ENERGIE NACH DEM STOSS UND THETA IM LAB SYSTHEM
C
      CALL CMLAB(EN,THETA,AAA)
C
C     INTERPOLATION DER QUERSCHNITTE UND FREIEN WEGLAENGE FUER NAECHSTE
C     WW
      CALL B10H14(EN,PATH0,PS1,PS2,PS3)
CC....
CC    FESTLEGEN DER FREIEN WEGLAENGE
```

```
CC    PATH0=2.0
CC....
      IF(N.GE.NUNT.AND.N.LE.NOB)WRITE(6,671)EN,PATH0,PS1,PS2,PS3
C
C     BERECHNUNG DES WEGES BIS ZUR NAECHSTEN WW
C
   39 PPP=RANDOM(0.)
      IF(PPP.EQ.0.)GOTO 39
      IF(PPP.LT.GRENZ1)PPP=GRENZ1
      IF(PPP.GT.GRENZ2)PPP=GRENZ2
CC... PPP=PPS2(M)
      S2=-PATH0*ALOG(PPP)
      IF(N.GE.NUNT.AND.N.LE.NOB)WRITE(6,415)N,M,PPP,S2
  415 FORMAT(' ',2I10,'  ZUFALLSZAHL,S2   ',2F10.5)
C
C     BERECHNEN DER KOORDINATEN DER M-TEN WW
C
      CALL EULER(X1,Y1,Z1,RMATRX,S2,THETA,PHI,X2,Y2,Z2,R2SQR)
      XX(M)=X2
      YY(M)=Y2
      ZZ(M)=Z2
      E(M)=EN
      SS(M)=S2
      STETA(M)=THETA
      SPHI(M)=PHI
      R(M)=SQRT(R2SQR)
      TT(M)=TT(M-1)+TTT*S2/SQRT(EN)
      IF(N.LT.NUNT.OR.N.GT.NOB)GOTO 40
      WRITE(6,678)N,M,X1,Y1,Z1,S2,THETA,PHI,X2,Y2,Z2,R2SQR
  678 FORMAT(2I6,' RPOLAR',10F10.3//)
   40 CONTINUE
C
C     FESTSTELLEN WO NEUER WW PUNKT LIEGT
C
C
C     ENTSCHEIDUNG WO NEUTRONENBAHN KUGELSCHALEN MIT RIN,ROUT,RPROBE
C     TRIFFT
C
   42 XN1=0.
      YN1=R(M-1)
      PYY=(R(M-1)+R(M)+S2)/2.
      IF(PYY.GT.AMAX1(R(M-1),R(M),S2))GOTO 43
C
C     SPEZIALFALL R(M-1),R(M)UND S2 LIEGEN AUF EINER GERADE
C
      WRITE(6,698)N,M,R(M-1),R(M),S2
  698 FORMAT(' STREUUNG SPEZIELL BEH.DA XN2=0, R(M-1),R(M),S2: ',2I10,3F
     110.5)
      IF(R(M).GE.R(M-1).AND.R(M).GT.ROUT.AND.S2.LT.AMAX1(R(M),R(M-1)))GO
     1TO 104
      GOTO 101
  104 DIFF1=R(M)-ROUT
      GOTO 200
  101 IF(R(M).GE.R(M-1).AND.R(M).LE.ROUT.AND.S2.LT.AMAX1(R(M),R(M-1)))GO
     1TO 3333
      IF(R(M).LT.R(M-1).AND.R(M).GE.RIN.AND.S2.LT.AMAX1(R(M),R(M-1)))GOT
```

```
   10 3333
    IF(R(M).LT.R(M-1).AND.R(M).LT.RIN.AND.S2.LT.AMAX1(R(M),R(M-1)))GOT
   10 103
    IF(R(M).LE.ROUT.AND.S2.GT.AMAX1(R(M),R(M-1)))GOTO 103
    IF(R(M).GT.ROUT.AND.S2.GT.AMAX1(R(M),R(M-1)))DIFF1=R(M)-ROUT
    GOTO 200
103 S2=S2+2.*RIN
    CALL RPOLAR(X1,Y1,Z1,S2,THETA,PHI,X2,Y2,Z2,R2SQR)
    XX(M)=X2
    YY(M)=Y2
    ZZ(M)=Z2
    SS(M)=S2
    R(M)=SQRT(R2SQR)
    TT(M)=TT(M-1)+TTT*S2/SQRT(E(M))
    IF(N.GE.NUNT.AND.N.LE.NOB)WRITE(6,685)X2,Y2,Z2,R2SQR
    TIMEPR=TT(M-1)+TTT*R(M-1)/SQRT(E(M))
    IF(N.GE.NUNT.AND.N.LE.NOB)WRITE(6,650)TIMEPR
650 FORMAT(' PROBE ZENTRAL DURCHQUERT TIMEPR: ',F10.5)
    GOTO 201
C
C   NORMALFALL R(M-1),R(M)UND S2 LIEGEN NICHT AUF EINER GERADEN
C
 43 PXX=SQRT((PYY-S2)*(PYY-R(M-1))*(PYY-R(M))/PYY)
    PALPHA=ATAN(PXX/(PYY-S2))
    PALPHA=PALPHA*2.
    XN2=R(M)*SIN(PALPHA)
    YN2=R(M)*COS(PALPHA)
    STEIG=(YN1-YN2)/(XN1-XN2)
    PPPP=2.*STEIG*YN1/(1.+STEIG**2)
    QQQQ=(YN1**2-RIN**2)/(1.+STEIG**2)
    QQQ1=(YN1**2-RPROB**2)/(1.+STEIG**2)
    QQQ2=(YN1**2-ROUT**2)/(1.+STEIG**2)
    DISK=PPPP**2/4.-QQQQ
    DISK1=PPPP**2/4.-QQQ1
    DISK2=PPPP**2/4.-QQQ2
    IF(N.GE.NUNT.AND.N.LE.NOB)WRITE(6,679)XN1,YN1,PALPHA,XN2,YN2,
   1STEIG,DISK,DISK1,DISK2
679 FORMAT(' XN1,YN1,PALPHA,XN2,YN2,STEIG,DISK,DISK1,DISK2',/,10F10.4)
C
C   FESTSTELLUNG OB NEUE WW PUNKT AUSSERHALB LIEGT
C
    IF(R2SQR.LE.QROUT)GOTO 13
C
C   BERECHNUNG WANN NEUTRON DIE AUSSENKUGEL DURCHQUERT
C
    XN3=-PPPP/2.+SQRT(DISK2)
    XN4=-PPPP/2.-SQRT(DISK2)
    YN3=STEIG*XN3+YN1
    YN4=STEIG*XN4+YN1
    DIFF1=SQRT((YN2-YN3)**2+(XN2-XN3)**2)
    DIFF2=SQRT((YN2-YN4)**2+(XN2-XN4)**2)
    IF(N.GE.NUNT.AND.N.LE.NOB)WRITE(6,681)XN3,XN4,YN3,YN4,DIFF1,DIFF2
681 FORMAT(' SNITTPUNKTE MIT AUSSENKUGEL XN3,XN4,YN3,YN4,DIFF1,DIFF2 '
   1,6F10.4)
    DIFF1=AMIN1(DIFF1,DIFF2)
200 TT(M)=TT(M-1)+TTT*(S2-DIFF1)/SQRT(EN)
```

```
      IF(N.GE.NUNT.AND.N.LE.NOB)WRITE(6,677)TT(M)
  677 FORMAT(' ZEITPUNKT WANN NEUTRON DIE KUGEL VERLAESST  ',F10.5)
      NOUT(M)=NOUT(M)+1
      KKK=1
      MMM=M
      GOTO 1111
   13 IF(DISK.LE.0.)GOTO 3333
C
C     NEUTRONENBAHN SCHNEIDET DIE INNENKUGEL
C
      XN3=-PPPP/2.+SQRT(DISK)
      XN4=-PPPP/2.-SQRT(DISK)
      YN3=STEIG*XN3+YN1
      YN4=STEIG*XN4+YN1
C
C     ENTSCHEIDUNG OB NEUTRON NACH INNEN ODER AUSSEN FLIEGT
C
      IF(XN2*XN3.LT.0.)GOTO 3333
      DIFF1=SQRT((YN1-YN3)**2+(XN1-XN3)**2)
      DIFF2=SQRT((YN1-YN4)**2+(XN1-XN4)**2)
      IF(S2.LE.AMIN1(DIFF1,DIFF2))GOTO 3333
C
C     BERECHNUNG DES NEUEN KORRIGIERTEN ORTES DER NAECHSTEN WW
C
      S2=S2+ABS(DIFF1-DIFF2)
      IF(N.GE.NUNT.AND.N.LE.NOB)WRITE(6,680)XN3,XN4,YN3,YN4,DIFF1,DIFF2,
     1S2
  680 FORMAT(' INNENK.DURCHQXN3,XN4,YN3,YN4,DIFF1,DIFF2,S2NEU  ',7F10.4)
      CALL RPOLAR(X1,Y1,Z1,S2,THETA,PHI,X2,Y2,Z2,R2SQR)
      XX(M)=X2
      YY(M)=Y2
      ZZ(M)=Z2
      SS(M)=S2
      R(M)=SQRT(R2SQR)
      TT(M)=TT(M-1)+TTT*S2/SQRT(E(M))
      IF(N.GE.NUNT.AND.N.LE.NOB)WRITE(6,685)X2,Y2,Z2,R2SQR
  685 FORMAT(' X2NEU,Y2NEU,Z2NEU,R2SQRNEU  ',4F10.4)
      IF(DISK1.LE.0.)GOTO 41
C
C     NEUTRON HAT BEREICH DER PROBE GETROFFEN
C
      XN3=-PPPP/2.+SQRT(DISK1)
      XN4=-PPPP/2.-SQRT(DISK1)
      YN3=STEIG*XN3+YN1
      YN4=STEIG*XN4+YN1
      DIFF1=SQRT((YN1-YN3)**2+(XN1-XN3)**2)
      DIFF2=SQRT((YN1-YN4)**2+(XN1-XN4)**2)
C
C     BERECHNUNG DES ZEITPUNKTS WANN PROBE GETROFFEN
C
      DIFF1=(DIFF1+DIFF2)/2.
      TIMEPR=TT(M-1)+TTT*DIFF1/SQRT(E(M))
      IF(N.GE.NUNT.AND.N.LE.NOB)WRITE(6,682)XN3,XN4,YN3,YN4,DIFF1,DIFF2,
     1TIMEPR
  682 FORMAT(' PROBE DURCHQUERT XN3,XN4,YN3,YN4,DIFF1,DIFF2,TIMEPR  ',
     17F10.4)
```

```
  201 NIN(M)=NIN(M)+1
      KPP=KPP+1
      ITIME=TIMEPR/10.
      ITIME=ITIME+1
      IF(ITIME.GT.200)ITIME=200
      NTIMEI(ITIME)=NTIMEI(ITIME)+1
      IENER=100.*E(M)/ENO
      IENER=IENER+1
      IF(IENER.GT.100)IENER=100
      NENIN(IENER)=NENIN(IENER)+1
C
C     FESTSTELLEN OB KORRIGIERTER ORT DER WW NOCH INNERHALB DER KUGEL
C
   41 IF(R2SQR.LE.QROUT)GOTO 3333
      GOTO42
C
C     ENTSCHEIDUNG OB NAECHSTE WW EINFANG ODER STREUUNG
C
 3333 PPP=RANDOM(0.)
      IF(PPP.LT.GRENZ1)PPP=GRENZ1
      IF(PPP.GT.GRENZ2)PPP=GRENZ2
C..33 PPP=PPAAA(M)
      IF(N.GE.NUNT.AND.N.LE.NOB)WRITE(6,694)N,M,PPP
  694 FORMAT(' ',2I10,'ZUFALLSZAHL FUER NAECHSTE WW  ',F10.5)
      IF(PPP.LE.PS1)GOTO 45
      IF(PPP.LE.PS2)GOTO 46
      IF(PPP.LE.PS3)GOTO 47
      NCAP(M)=NCAP(M)+1
      KCC=1
      MMM=M
      IF(N.GE.NUNT.AND.N.LE.NOB)WRITE(6,695)N,M
  695 FORMAT(' ',2I10,'  NEUTRON EINGEFANGEN  ')
      GOTO 1111
   45 AAA=AA1
      GOTO 2222
   46 AAA=AA2
      GOTO 2222
   47 AAA=AA3
 2222 CONTINUE
C
C     WEG DES NEUTRONS IST BEENDET ENTWEDER ENTKOMMEN ODER EINGEFANGEN
C
 1111 IF(M.EQ.100)WRITE(6,686)N
  686 FORMAT(' NEUTRON MIT FOLGENDER NUMMER BLEIBT IM KRISTALL ',I10)
      IF(N.LT.NUNT.OR.N.GT.NOB)GOTO 51
      WRITE(6,683)
  683 FORMAT(' E(M),XX(M),YY(M),ZZ(M),TT(M),SS(M),TETA(M),PHI(M),R(M)')
      DO 50 K=1,M
      WRITE(6,684)E(K),XX(K),YY(K),ZZ(K),TT(K),SS(K),STETA(K),SPHI(K),
     1R(K)
  684 FORMAT(10F10.4)
   50 CONTINUE
      IF(M.LT.NWRITE)WRITE(6,696)
  696 FORMAT(' '////)
   51 ITIME=TT(M)/10.
      ITIME=ITIME+1
```

```
      IF(ITIME.GT.200)ITIME=200                                         00045600
      IENER=100.*E(M)/ENO                                               00045700
      IENER=IENER+1                                                     00045800
      IF(IENER.GT.100)IENER=100                                         00045900
      IF(KCC.EQ.1)GOTO 55                                               00046000
      IF(KKK.EQ.1)GOTO 56                                               00046100
      NNN=NNN+1                                                         00046200
      GOTO 1000                                                         00046300
   55 NTIMEC(ITIME)=NTIMEC(ITIME)+1                                     00046400
      NENCAP(IENER)=NENCAP(IENER)+1                                     00046500
C.... IF(ITIME.LT.20)WRITE(6,651)N,M,ITIME,TT(M),E(M),R(M)              00046510
C.651 FORMAT(' NEUTRON EINGEFANGEN N,M,ITIME,TT,E,R  ',3I10,3F10.5)     00046520
      GOTO 1000                                                         00046600
   56 NTIMEO(ITIME)=NTIMEO(ITIME)+1                                     00046700
      NENOUT(IENER)=NENOUT(IENER)+1                                     00046800
C1000 WRITE(6,697)N,M,KKK,KCC,KPP                                       00046900
  697 FORMAT(' N,M,KKK,KCC,KPP  ',5I10)                                 00047000
 1000 CONTINUE                                                          00047100
      WRITE(6,703)                                                      00047200
  703 FORMAT('1'/)                                                      00047300
      WRITE(6,690)                                                      00047400
      WRITE(6,691)                                                      00047500
  690 FORMAT('                        RAUSGESTREUTE NEUTRONEN           EI00047600
     1NGEFANGENE NEUTRONEN                  NEUTRONEN DIE PROBE TREFFEN 00047700
     2  '/)                                                             00047800
  691 FORMAT('         KANAL    ANZAHL   ENERGIE     ZEIT1      ZEIT2   ANZ00047900
     1AHL   ENERGIE     ZEIT1      ZEIT2    ANZAHL   ENERGIE      ZEIT1 00048000
     2  ZEIT2  '/)                                                      00048100
      DO 59 KK1=1,10                                                    00048200
      DO 60 KK2=1,10                                                    00048300
      K=(KK1-1)*10+KK2                                                  00048400
      WRITE(6,692)K,NOUT(K),NENOUT(K),NTIMEO(K),NTIMEO(100+K),NCAP(K),  00048500
     1NENCAP(K),NTIMEC(K),NTIMEC(100+K),NIN(K),NENIN(K),NTIMEI(K),      00048600
     2NTIMEI(100+K)                                                     00048700
   60 CONTINUE                                                          00048800
  692 FORMAT(' ',13I10)                                                 00048900
      WRITE(6,699)                                                      00049000
  699 FORMAT(' ')                                                       00049100
   59 CONTINUE                                                          00049200
      WRITE(6,700)                                                      00049300
  700 FORMAT(/' GEMITTELTE ERGEBNISSE UEBER 10 KANAELE  '/)             00049400
      DO 63 KK1=1,10                                                    00049500
      DO 63 KK2=1,12                                                    00049600
   63 IFELD(KK1,KK2)=0                                                  00049700
      DO 61 KK1=1,10                                                    00049800
      DO 62 KK2=1,10                                                    00049900
      K=(KK1-1)*10+KK2                                                  00050000
      IFELD(KK1,1)=IFELD(KK1,1)+NOUT(K)                                 00050100
      IFELD(KK1,2)=IFELD(KK1,2)+NENOUT(K)                               00050200
      IFELD(KK1,3)=IFELD(KK1,3)+NTIMEO(K)                               00050300
      IFELD(KK1,4)=IFELD(KK1,4)+NTIMEO(100+K)                           00050400
      IFELD(KK1,5)=IFELD(KK1,5)+NCAP(K)                                 00050500
      IFELD(KK1,6)=IFELD(KK1,6)+NENCAP(K)                               00050600
      IFELD(KK1,7)=IFELD(KK1,7)+NTIMEC(K)                               00050700
      IFELD(KK1,8)=IFELD(KK1,8)+NTIMEC(100+K)                           00050800
      IFELD(KK1,9)=IFELD(KK1,9)+NIN(K)                                  00050900
```

```
      IFELD(KK1,10)=IFELD(KK1,10)+NENIN(K)                              00051000
      IFELD(KK1,11)=IFELD(KK1,11)+NTIMEI(K)                             00051100
      IFELD(KK1,12)=IFELD(KK1,12)+NTIMEI(100+K)                         00051200
   62 CONTINUE                                                          00051300
      WRITE(6,692)KK1,(IFELD(KK1,J),J=1,12)                             00051400
   61 CONTINUE                                                          00051500
      DO 64 I=1,12                                                      00051510
      DO 64 K=2,10                                                      00051520
   64 IFELD(1,I)=IFELD(1,I)+IFELD(K,I)                                  00051530
      K=1                                                               00051540
      WRITE(6,701)                                                      00051550
  701 FORMAT(/' TOTALE SUMMEN'/)                                        00051560
      WRITE(6,692)K,(IFELD(1,I),I=1,12)                                 00051570
      WRITE(6,693)NNN                                                   00051580
  693 FORMAT(/' NEUTRONEN IN DER PROBE STEKENGEBL.  ',I10)              00051600
      AMIOUT=0.                                                         00051610
      AMICAP=0.                                                         00051620
      AMIIN=0.                                                          00051630
      DO 65 K=1,100                                                     00051640
      AMIOUT=AMIOUT+FLOAT(K*NOUT(K))                                    00051650
      AMICAP=AMICAP+FLOAT(K*NCAP(K))                                    00051660
      AMIIN=AMIIN+FLOAT(K*NIN(K))                                       00051670
   65 CONTINUE                                                          00051680
      AMIOUT=AMIOUT/FLOAT(IFELD(1,1))                                   00051690
      AMICAP=AMICAP/FLOAT(IFELD(1,5))                                   00051691
      AMIIN=AMIIN/FLOAT(IFELD(1,9))                                     00051692
      WRITE(6,702)AMIOUT,AMICAP,AMIIN                                   00051693
  702 FORMAT(/' MITTLERE ANZAHL DER WW,MIOUT,MICAP,MIIN:  ',3F10.5)     00051694
      DO112 K=1,100                                                     00051695
      MENOUT(L,K)=NENOUT(K)                                             00051696
      MENCAP(L,K)=NENCAP(K)                                             00051697
      MTIMEO(L,K)=NTIMEO(K)                                             00051698
      MTIMEC(L,K)=NTIMEC(K)                                             00051699
      MTIMEO(L,100+K)=NTIMEO(100+K)                                     00051700
      MTIMEC(L,100+K)=NTIMEC(100+K)                                     00051701
  112 CONTINUE                                                          00051702
 4444 CONTINUE                                                          00051703
C                                                                       00051704
C     BERECHNUNG DES TOF SPEKTRUMS DES EFFEKT                           00051705
C                                                                       00051706
      DO113 K=1,NENER                                                   00051707
      TIMELO(K)=TTT*FLUGW/SQRT(ELOWER(K))                               00051708
      TIMEUP(K)=TTT*FLUGW/SQRT(EUPPER(K))                               00051709
  113 CONTINUE                                                          00051710
      DO114 K=1,NENER                                                   00051711
      KK1=TIMEUP(K)/10.                                                 00051712
      KK1=KK1+1                                                         00051713
      KK2=TIMELO(K)/10.                                                 00051714
      IF(KK2.LT.KK1)KK2=KK1                                             00051715
      AFLUSS=FLUSS(K)*SIGMAG(K)/FLOAT(KK2-KK1+1)                        00051716
      AFLUSS=AFLUSS*(EUPPER(K)-ELOWER(K))/10.                           00051717
      DO 115 I=KK1,KK2                                                  00051718
      IF(I.GT.200)J=I-200                                               00051719
      J=I                                                               00051720
      EFFEKT(J)=EFFEKT(J)+AFLUSS                                        00051721
  115 CONTINUE                                                          00051722
```

```
  114 CONTINUE
C
C     BERECHNUNG DER ZEITVERTEILUNG DER EINFANGERREIGNISSE
C     UND NEUTRONEN DIE DIE KUGEL VERLASSEN
C
      DO117 K=1,NENER
      TMIT=(TIMEUP(K)+TIMELO(K))/2.
      ITMIT=TMIT/10.
      ITMIT=ITMIT+1
      FLNORM=FLUSS(K)*SIGMAG(K)*FAKTOR(K)/FLOAT(NEUTRS)
      FLNORM=FLNORM*(EUPPER(K)-ELOWER(K))/10.
      DO 118 I=1,199
      J=I+ITMIT
      IF(J.GT.200)J=J-200
      UNTCAP(J)=UNTCAP(J)+FLOAT(MTIMEC(K,I))*FLNORM
      UNTOUT(J)=UNTOUT(J)+FLOAT(MTIMEO(K,I))*FLNORM
  118 CONTINUE
C
C     UNTERGRUND MIT MEHR ALS 2 MICROSEC WIRD ALS KONSTANNTE ADDIERT
C
      UNTCO1=FLOAT(MTIMEC(K,200))*FLNORM
      UNTCO2=FLOAT(MTIMEO(K,200))*FLNORM
      UNTCO1=UNTCO1/200.
      UNTCO2=UNTCO2/200.
      DO119 I=1,200
      UNTCAP(I)=UNTCAP(I)+UNTCO1
      UNTOUT(I)=UNTOUT(I)+UNTCO2
  119 CONTINUE
  117 CONTINUE
C
C     BERECHNUNG DER ENERGIEVERTEILUNG DER NEUTRONEN CAP UND OUT
C
      DO 120 K=1,NENER
      FLNORM=FLUSS(K)*SIGMAG(K)*FAKTOR(K)/FLOAT(NEUTRS)
      FLNORM=FLNORM*(EUPPER(K)-ELOWER(K))/10.
      EMIT=(ELOWER(K)+EUPPER(K))/2.
      DO 121 I=1,100
      EEE=EMIT*FLOAT(I)/100.-EMIT/200.
      IEEE=EEE/0.1
      IEEE=IEEE+1
      IF(IEEE.GT.1000)IEEE=1000
      ENECAP(IEEE)=ENECAP(IEEE)+FLOAT(MENCAP(K,I))*FLNORM
      ENEOUT(IEEE)=ENEOUT(IEEE)+FLOAT(MENOUT(K,I))*FLNORM
  121 CONTINUE
  120 CONTINUE
      DO 125 K=1,200
      I=(K-1)*5+1
      ENECAP(K)=ENECAP(I)+ENECAP(I+1)+ENECAP(I+2)+ENECAP(I+3)+ENECAP(I+4
     1)
      ENEOUT(K)=ENEOUT(I)+ENEOUT(I+1)+ENEOUT(I+2)+ENEOUT(I+3)+ENEOUT(I+4
     1)
  125 CONTINUE
      WRITE(6,703)
      WRITE(6,417)
  417 FORMAT('     KANAL      EFFEKT     UNTCAP     UNTOUT     ENECAP     ENE
     1OUT   '/)
```

```
      DO 123 KK1=1,20
      DO 126 KK2=1,10
      K=(KK1-1)*10+KK2
      WRITE(6,416)K,EFFEKT(K),UNTCAP(K),UNTOUT(K),ENECAP(K),ENEOUT(K)
  126 CONTINUE
      WRITE(6,699)
  123 CONTINUE
      DO 127 KK1=1,20
      DO 127 KK2=1,5
  127 OFELD(KK1,KK2)=0.
      WRITE(6,700)
      DO 128 KK1=1,20
      DO 129 KK2=1,10
      K=(KK1-1)*10+KK2
      OFELD(KK1,1)=OFELD(KK1,1)+EFFEKT(K)
      OFELD(KK1,2)=OFELD(KK1,2)+UNTCAP(K)
      OFELD(KK1,3)=OFELD(KK1,3)+UNTOUT(K)
      OFELD(KK1,4)=OFELD(KK1,4)+ENECAP(K)
      OFELD(KK1,5)=OFELD(KK1,5)+ENEOUT(K)
  129 CONTINUE
      WRITE(6,416)KK1,(OFELD(KK1,J),J=1,5)
  128 CONTINUE
      DO 130 I=1,5
      DO 130 K=2,20
      OFELD(1,I)=OFELD(1,I)+OFELD(K,I)
  130 CONTINUE
      K=1
      WRITE(6,701)
      WRITE(6,416)K,(OFELD(1,I),I=1,5)
  416 FORMAT(' ',I10,5F10.3)
      DO 131 K=1,200
      XXX(K)=FLOAT(K)
  131 CONTINUE
      DO 132 K=1,200
      EFFEKT(K)=EFFEKT(K)+UNTCAP(K)
  132 CONTINUE
      CALL PLOTS(IBUF,8000,1)
      CALL PLOT(1.,1.,-3)
      CALL PLOT2(200.,0.,9,1,XXX,1.,200.,10.,0.,200.,EFFEKT,5.,0.,100.,Y
     1YY,YYY,0)
      CALL PLOT2(200.,0.,9,1,XXX,1.,200.,10.,0.,200.,UNTCAP,5.,0.,100.,Y
     1YY,YYY,0)
      CALL SYMBOL(4.,4.,0.25,17HEFFEKT+UNTERGRUND,0.,17)
      CALL PLOT(0.,6.,-3)
      CALL PLOT2(200.,0.,9,1,XXX,1.,200.,10.,0.,200.,UNTCAP,5.,0.,100.,Y
     1YY,YYY,0)
      CALL SYMBOL(4.,4.,0.25,6HUNTCAP,0.,6)
      CALL PLOT(0.,6.,-3)
      CALL PLOT2(200.,0.,9,1,XXX,1.,200.,10.,0.,200.,UNTOUT,5.,0.,200.,Y
     1YY,YYY,0)
      CALL SYMBOL(4.,4.,0.25,6HUNTOUT,0.,6)
      IF(AA1.EQ.137)CALL SYMBOL(4.,6.,0.25,3HBAF,0.,3)
      IF(AA1.EQ.209)CALL SYMBOL(4.,6.,0.25,3HBGO,0.,3)
      CALL NUMBER(4.,5.5,0.25,RIN,0.,1)
      CALL NUMBER(6.,5.5,0.25,ROUT,0.,1)
      CALL PLOT(11.,-12.,-3)
```

```
      DO 133 K=1,100                                                    00051835
      I=(K-1)*2+1                                                       00051836
      ENECAP(K)=ENECAP(I)+ENECAP(I+1)                                   00051837
      ENEOUT(K)=ENEOUT(I)+ENEOUT(I+1)                                   00051838
  133 CONTINUE                                                          00051839
      CALL PLOT2(200.,0.,9,1,XXX,1.,100.,10.,0.,100.,ENECAP,5.,0.,200.,Y00051840
     1YY,YYY,0)                                                         00051841
      CALL SYMBOL(4.,4.,0.25,6HENECAP,0.,6)                             00051842
      CALL PLOT(0.,6.,-3)                                               00051843
      CALL PLOT2(200.,0.,9,1,XXX,1.,100.,10.,0.,100.,ENEOUT,5.,0.,400.,Y00051844
     1YY,YYY,0)                                                         00051845
      CALL SYMBOL(4.,4.,0.25,6HENEOUT,0.,6)                             00051846
      DO 136 K=1,100                                                    00051847
      ENEIN(K)=0.                                                       00051848
  136 CONTINUE                                                          00051849
      DO 134 K=1,NENER                                                  00051850
      KK1=ELOWER(K)                                                     00051851
      KK2=EUPPER(K)                                                     00051852
      KK2=KK2-1                                                         00051853
      DO 135 I=KK1,KK2                                                  00051854
      ENEIN(I)=FLUSS(K)                                                 00051855
  135 CONTINUE                                                          00051856
  134 CONTINUE                                                          00051857
      CALL PLOT(0.,6.,-3)                                               00051858
      CALL PLOT2(200.,0.,9,1,XXX,1.,100.,10.,0.,100.,ENEIN,5.,0.,100.,Y 00051859
     1YY,YYY,0)                                                         00051860
      CALL SYMBOL(4.,4.,0.25,5HENEIN,0.,5)                              00051861
      CALL PLOT(0.,0.,999)                                              00051862
  999 STOP                                                              00051863
      END                                                               00051870
      SUBROUTINE CMLAB(EN,THETA,AAA)                                    00051900
C                                                                       00052000
C             INPUT  :  NEUTRON ENERGY                                  00052100
C                       STREUWINKLE IN CENTER OF MASS FRAME             00052200
C             OUTPUT :  ENERGY & ANGLE , IN LAB. FRAME                  00052300
C                                                                       00052400
      COMMON NUNT,NOB,N,M,IY,DENSTY,ESIG,SIGC,SIGN,AI1,AI2,AI3          00052500
      DIMENSION ESIG(3,100)                                             00052600
      CTHETA=COS(THETA)                                                 00052700
      A1A1=AAA**2+2.*AAA*CTHETA+1.                                      00052800
      IF(AAA.EQ.1..AND.A1A1.EQ.0.)TETLAB=1.5708                         00052810
      IF(AAA.EQ.1..AND.A1A1.EQ.0.)GOTO 2                                00052820
      CTHLAB=(AAA*CTHETA+1.)/SQRT(A1A1)                                 00052900
      TETLAB=ACOS(CTHLAB)                                               00053000
    2 ENNEU=EN*A1A1/(AAA+1.)**2                                         00053100
      IF(ENNEU.LE.ESIG(1,1).AND.EN.GT.ESIG(1,1))WRITE(6,601)N,M         00053200
  601 FORMAT(' NEUTRONENENERGIE AN UNTERER GRENZE  N,M  ',2I10)         00053300
      IF(ENNEU.LE.ESIG(1,1))ENNEU=ESIG(1,1)                             00053400
      IF(N.GE.NUNT.AND.N.LE.NOB)WRITE(6,600)N,M,THETA,TETLAB,EN,ENNEU,  00053500
     1AAA                                                               00053510
  600 FORMAT(2I6,'CMLAB: TETA-CM,TETA-LAB,EIN,EOUT,AAA',5F10.3/)        00053600
      THETA=TETLAB                                                      00053700
      EN=ENNEU                                                          00053800
      RETURN                                                            00053900
      END                                                               00054000
      SUBROUTINE EULER(XIN,YIN,ZIN,RMATRX,R,THETA,PHI,XOUT,YOUT,ZOUT,   00054100
```

```
     2R2SQR)
      COMMON NUNT,NOB,N,M,IY,DENSTY,ESIG,SIGC,SIGN,AI1,AI2,AI3
      DIMENSION RMATRX(3,3),RR(3,3),EUL(3,3)
C        ----     XYZ IN ROTATED FRAME     ----
      X=R*SIN(THETA)*COS(PHI)
      Y=R*SIN(THETA)*SIN(PHI)
      Z=R*COS(THETA)
C        ----      XYZ IN LAB. FRAME        ----
      XOUT=XIN+X*RMATRX(1,1)+Y*RMATRX(1,2)+Z*RMATRX(1,3)
      YOUT=YIN+X*RMATRX(2,1)+Y*RMATRX(2,2)+Z*RMATRX(2,3)
      ZOUT=ZIN+X*RMATRX(3,1)+Y*RMATRX(3,2)+Z*RMATRX(3,3)
      R2SQR=XOUT**2+YOUT**2+ZOUT**2
C...  IF(M.LT.NWRITE)WRITE(6,600)N,M,XIN,YIN,ZIN,R,THETA,PHI,XOUT,YOUT,
C... 2ZOUT,R2SQR
C.600 FORMAT(2I6,' EULER: XYZ-IN  S2  TETAFI-IN  XYZ-OUT  R2'/10F10.3/)
C  ----   ROTATION MATRIX FOR THE INPUT THETA-PHI VALUES   ----
      EUL(1,1)=COS(THETA)*COS(PHI)
      EUL(1,2)=-SIN(PHI)
      EUL(1,3)=SIN(THETA)*COS(PHI)
      EUL(2,1)=COS(THETA)*SIN(PHI)
      EUL(2,2)=COS(PHI)
      EUL(2,3)=SIN(THETA)*SIN(PHI)
      EUL(3,1)=-SIN(THETA)
      EUL(3,2)=0.
      EUL(3,3)=COS(THETA)
C...  IF(M.LT.NWRITE)WRITE(6,611)RMATRX,EUL
C.611 FORMAT(2X,'RMATRX-IN , EUL(TETA,FI)'/9F7.2/9F7.2/)
C       ----   ROTATION MATRIX OF THE NEW FRAME   ----
      DO 10 I=1,3
      DO 10 J=1,3
   10 RR(I,J)=0.
      DO 100 I=1,3
      DO 100 J=1,3
      DO 100 K=1,3
  100 RR(I,J)=RR(I,J)+RMATRX(I,K)*EUL(K,J)
      DO 11 I=1,3
      DO 11 J=1,3
   11 RMATRX(I,J)=RR(I,J)
C   ----   THETA-PHI OF NEW Z-AXIS , IN THE LAB. FRAME   ----
      THETA=ARCOS(RMATRX(3,3))
C     PHI=ARCOS(RMATRX(2,2))
C     IF(RMATRX(1,2).GT.0.)PHI=2.*3.1416-PHI
      XZUNIT=RMATRX(1,3)
      YZUNIT=RMATRX(2,3)
      IF(XZUNIT.EQ.0.)PHI=1.5708
      IF(XZUNIT.EQ.0.)GOTO 12
      PHI=ATAN(YZUNIT/XZUNIT)
   12 IF(XZUNIT.LT.0.)PHI=PHI+3.1416
C.612 FORMAT(' RMATRX-OUT    TETA,FI-OUT'/2X,9F10.2/2F10.3/)
C...  IF(M.LT.NWRITE)WRITE(6,612)RMATRX,THETA,PHI
      RETURN
      END
      SUBROUTINE B10H14(EN,SIGDEN,PPS1,PPS2,PPS3)
C
C  INPUT : N-ENERGY (EN)
C  OUTPUT: AVERAGE FREE PATH SIGDEN
C          PROBABILITY OF SCATTERING WITH NUCLEUS 1     PPS1
```

```
C                                  WITH NUCLEUS 1+2   PPS2
C                                  WITH NUCLEUS 1+2+3 PPS3
C                     OF CAPTURE   1-PPS3
C
      COMMON NUNT,NOB,N,M,IY,DENSTY,ESIG,SIGC,SIGN;AI1,AI2,AI3
      DIMENSION ESIG(3,100),SIGC(3,100),SIGN(3,100),SIGC1(3),SIGN1(3)
      DO 1 K=1,3
      SIGC1(K)=0.
      SIGN1(K)=0.
    1 CONTINUE
      II=3
      IF(SIGN(3,1).EQ.0.)II=2
      IF(SIGN(2,1).EQ.0.)II=1
C
C     LINEARE INTERPOLATION DER STREU UND EINFANGQUERSCHNITTE
C
      DO 5 I=1,II
      DO 6 K=1,99
      IF(EN.LE.ESIG(I,K+1).AND.EN.GE.ESIG(I,K))GOTO 2
      IF(K.EQ.99)WRITE(6,608)EN
  608 FORMAT(' NEUTRONENENERGIE NICHT IM BEREICH DER STUETZST. ',F10.5)
    6 CONTINUE
    2 SIGC1(I)=SIGC(I,K)+(EN-ESIG(I,K))*(SIGC(I,K+1)-SIGC(I,K))/
     1(ESIG(I,K+1)-ESIG(I,K))
      SIGN1(I)=SIGN(I,K)+(EN-ESIG(I,K))*(SIGN(I,K+1)-SIGN(I,K))/
     1(ESIG(I,K+1)-ESIG(I,K))
      IF(N.GE.NUNT.AND.N.LE.NOB)WRITE(6,605)EN,SIGC1(I),SIGN1(I)
  605 FORMAT(' INTERPOLIERTER QUERSCHNITT PRO ATOM  ',3F10.5)
    5 CONTINUE
C
C     GESAMMTQUERSCHNITTE PRO MOLEKUEL CAPTURE,STREUUNG,TOTAL
C
      SIGCTO=AI1*SIGC1(1)+AI2*SIGC1(2)+AI3*SIGC1(3)
      SIGNTO=AI1*SIGN1(1)+AI2*SIGN1(2)+AI3*SIGN1(3)
      SIGTTO=SIGCTO+SIGNTO
      PPS1=AI1*SIGN1(1)/SIGTTO
      PPS2=(AI1*SIGN1(1)+AI2*SIGN1(2))/SIGTTO
      PPS3=(AI1*SIGN1(1)+AI2*SIGN1(2)+AI3*SIGN1(3))/SIGTTO
      IF(N.GE.NUNT.AND.N.LE.NOB)WRITE(6,606)SIGCTO,SIGNTO,SIGTTO
  606 FORMAT(' TOTALE QUERSCHNITTE JE MOLEKUEL,CAPT,SCATT,TOTAL ',3F10.4
     1)
      SIGTTO=SIGTTO*1.E-24
      SIGDEN=1./(DENSTY*SIGTTO)
      IF(N.GE.NUNT.AND.N.LE.NOB)WRITE(6,607)SIGDEN
  607 FORMAT(' FREIE WEGLAENGE  ',F10.5)
      RETURN
      END
      SUBROUTINE RPOLAR(XIN,YIN,ZIN,R,THETA,PHI,XOUT,YOUT,ZOUT,R2SQR)
C GANZ DUMM : ROUT=RIN+(R,TETA,FI)
      XOUT=R*SIN(THETA)*COS(PHI)+XIN
      YOUT=R*SIN(THETA)*SIN(PHI)+YIN
      ZOUT=R*COS(THETA)+ZIN
      R2SQR=XOUT*XOUT+YOUT*YOUT+ZOUT*ZOUT
      RETURN
      END
      FUNCTION RANDOM(ANY)
C  GENERATING RANDON NO. IN (0. BIS 1.)INTERVAL
C  INPUT ANY "ANY" VALUE, IT WILL BE IGNORED ANYWAY
```

```
COMMON NUNT,NOB,N,M,IY,DENSTY,ESIG,SIGC,SIGN,AI1,AI2,AI3
IX=IY
CALL RANDU(IX,IY,RA)
RANDOM=RA
RETURN
END
```

APPENDIX B Tables of coordinates for a spherical shell of 12 pentagons and 30 hexagons

Table B.1 Midpoints of all hexagons and pentagons forming a sphere with 430 mm radius in Cartesian and polar coordinates .

Number	Type	X	Y	Z	δ	φ
1	P	0	0	430.000	0	0
2	H	132.877	182.890	365.780	54.000	31.717
3	H	215.000	-69.858	365.780	342.000	31.717
4	H	0	-226.064	365.780	270.000	31.717
5	H	-215.000	-69.859	365.780	198.000	31.717
6	H	-132.877	182.890	365.780	126.000	31.717
7	H	0	365.780	226.064	90.000	58.283
8	P	226.064	311.151	192.302	54.000	63.435
9	H	347.877	113.032	226.064	18.000	58.283
10	P	365.780	-118.849	192.302	342.000	63.435
11	H	215.000	-295.922	226.064	306.000	58.283
12	P	0	-384.604	192.302	270.000	63.435
13	H	-215.000	-295.922	226.064	234.000	58.283
14	P	-365.780	-118.849	192.302	198.000	63.435
15	H	-347.877	113.032	226.064	162.000	58.283
16	P	-226.064	311.151	192.302	126.000	63.435
17	H	132.877	408.954	0	72.000	90.000
18	H	347.877	252.748	0	36.000	90.000
19	H	430.000	0	0	0	90.000
20	H	347.877	-252.748	0	324.000	90.000
21	H	132.877	-408.954	0	288.000	90.000
22	H	-132.877	-408.954	0	252.000	90.000
23	H	-347.877	-252.748	0	216.000	90.000
24	H	-430.000	0	0	180.000	90.000
25	H	-347.877	252.748	0	144.000	90.000
26	H	-132.877	408.954	0	108.000	90.000
27	P	0	384.604	-192.302	90.000	116.565

Number	Type	X	Y	Z	δ	φ
28	H	215.000	295.922	-226.064	54.000	121.717
29	P	365.780	118.849	-192.302	18.000	116.565
30	H	347.877	-113.032	-226.064	342.000	121.717
31	P	226.064	-311.151	-192.302	306.000	116.565
32	H	0	-365.780	-226.064	270.000	121.717
33	P	-226.064	-311.151	-192.302	234.000	116.565
34	H	-347.877	-113.032	-226.064	198.000	121.717
35	P	-365.780	118.849	-192.302	162.000	116.565
36	H	-215.000	295.922	-226.064	126.000	121.717
37	H	0	226.064	-365.780	90.000	148.283
38	H	215.000	69.858	-365.780	18.000	148.283
39	H	132.877	-182.890	-365.780	306.000	148.283
40	H	-132.877	-182.890	-365.780	234.000	148.283
41	H	-215.000	69.858	-365.780	162.000	148.283
42	P	0	0	-430.000	0	180.000

Table B.2 Edges of all hexagons and pentagons forming a sphere of 430 mm diameter, the missing second half of the points is obtained by replacing Y by -Y and Z by -Z or δ by 180+δ and φ by 180-φ.

Number	Type	X	Y	Z	δ	φ
1	PH	0	148.585	403.513	90.000	20.215
2	PH	141.313	45.915	-.-	18.000	-.-
3	PH	87.336	-120.208	-.-	306.000	-.-
4	PH	-87.336	-120.208	-.-	234.000	-.-
5	PH	-141.313	45.915	-.-	162.000	20.215
6	HH	0	261.037	341.701	90.000	37.377
7	HH	248.261	80.665	-.-	18.000	-.-
8	HH	153.434	-211.183	-.-	306.000	-.-
9	HH	-153.434	-211.183	-.-	234.000	-.-

Number	Type	X	Y	Z	δ	φ
10	HH	-248.261	80.665	-.-	162.000	-.-
11	PH	109.884	299.828	287.973	69.873	47.956
12	PH	251.199	197.156	-.-	38.127	-.-
13	PH	319.109	-11.852	-.-	357.873	-.-
14	PH	265.131	-177.980	-.-	326.127	-.-
15	PH	87.339	-307.154	-.-	285.873	-.-
16	PH	-87.339	-307.154	-.-	254.127	-.-
17	PH	-265.131	-177.980	-.-	213.873	-.-
18	PH	-319.109	-11.852	-.-	182.127	-.-
19	PH	-251.199	197.156	-.-	141.873	-.-
20	PH	-109.882	299.829	-.-	110.127	-.-
21	PH	109.884	391.659	139.388	74.328	71.085
22	PH	338.534	225.535	-.-	33.672	-.-
23	PH	406.446	16.524	-.-	2.328	-.-
24	PH	319.109	-252.271	-.-	321.672	-.-
25	PH	141.313	-318.447	-.-	290.328	-.-
26	PH	-141.313	-381.447	-.-	249.672	-.-
27	PH	-319.109	-252.271	-.-	218.328	-.-
28	PH	-406.446	16.524	-.-	177.672	-.-
29	PH	-338.534	225.535	-.-	146.328	-.-
30	PH	-109.884	391.659	-.-	105.672	-.-
31	HH	0	422.366	80.665	90.000	79.188
32	HH	401.694	130.518	-.-	18.000	-.-
33	HH	248.261	-341.701	-.-	306.000	-.-
34	HH	-248.261	-341.701	-.-	234.000	-.-
35	HH	-401.694	130.518	-.-	162.000	-.-
36	PH	251.197	345.744	47.558	54.000	83.650
37	PH	406.446	-132.062	-.-	342.000	-.-
38	PH	0	-427.363	-.-	270.000	-.-
39	PH	-406.446	-132.062	-.-	198.000	-.-
40	PH	-251.197	345.744	-.-	126.000	-.-

Table B.3 Midpoints of the edges of all hexagons and pentagons forming a sphere of 430 mm diameter. The remaining half of the points is obtained by replacing Y by −Y and Z by −Z or δ by 180+δ and φ by 180−φ .

Number	Type	X	Y	Z	δ	φ
1	PH	72.161	99.321	412.102	54.000	16.589
2	PH	−116.769	−37.937	−.−	198.000	−.−
3	PH	0	−122.768	−.−	270.000	−.−
4	PH	116.759	−37.937	−.−	342.000	−.−
5	PH	−72.161	99.321	−.−	126.000	−.−
6	HH	0	207.128	376.826	90.000	28.796
7	HH	196.990	64.006	−.−	18.000	−.−
8	HH	121.747	−167.570	−.−	306.000	−.−
9	HH	−121.747	−167.570	−.−	234.000	−.−
10	HH	−196.990	64.006	−.−	162.000	−.−
11	HH	55.565	283.609	318.401	78.915	42.229
12	HH	252.557	140.485	−.−	29.085	−.−
13	HH	286.898	34.795	−.−	6.915	−.−
14	HH	211.654	−196.784	−.−	317.085	−.−
15	HH	121.748	−262.104	−.−	294.915	−.−
16	HH	−121.748	−262.104	−.−	245.085	−.−
17	HH	−211.653	−196.784	−.−	222.915	−.−
18	HH	−286.898	34.795	−.−	173.085	−.−
19	HH	−252.557	140.485	−.−	150.915	−.−
20	HH	−55.565	283.609	−.−	101.085	−.−
21	PH	184.383	253.782	294.104	54.000	46.846
22	PH	298.338	−96.936	−.−	342.000	−.−
23	PH	0	−311.692	−.−	270.000	−.−
24	PH	−298.338	−96.936	−.−	198.000	−.−
25	PH	−184.383	253.782	−.−	126.000	−.−
26	PH	112.223	353.103	218.229	72.369	59.502
27	PH	301.143	215.844	−.−	35.631	−.−
28	PH	370.500	2.386	−.−	0.369	−.−
29	PH	298.338	−219.705	−.−	323.631	−.−

Number	Type	X	Y	Z	δ	φ
30	PH	116.760	-351.629	-.-	288.369	-.-
31	PH	-116.760	-351.629	-.-	251.631	-.-
32	PH	-298.338	-219.705	-.-	216.369	-.-
33	PH	-370.500	2.386	-.-	179.631	-.-
34	PH	-301.143	215.844	-.-	144.369	-.-
35	PH	-112.221	353.104	-.-	107.631	-.-
36	HH	55.563	411.619	111.275	82.312	75.002
37	HH	374.302	180.043	-.-	25.688	-.-
38	HH	408.643	74.351	-.-	10.312	-.-
39	HH	286.897	-300.346	-.-	313.688	-.-
40	HH	196.990	-365.667	-.-	298.312	-.-
41	HH	-196.990	-365.667	-.-	241.688	-.-
42	HH	-286.897	-300.346	-.-	226.312	-.-
43	HH	-408.643	74.351	-.-	169.688	-.-
44	HH	-374.302	180.043	-.-	154.312	-.-
45	HH	-55.565	411.619	-.-	97.688	-.-
46	PH	184.259	376.379	96.370	63.916	77.049
47	PH	301.021	291.546	-.-	44.084	-.-
48	PH	414.897	-58.930	-.-	351.916	-.-
49	PH	370.297	-196.195	-.-	332.084	-.-
50	PH	72.164	-412.801	-.-	279.916	-.-
51	PH	-72.164	-412.801	-.-	260.084	-.-
52	PH	-370.297	-196.195	-.-	207.916	-.-
53	PH	-414.897	-58.930	-.-	188.084	-.-
54	PH	-301.021	291.546	-.-	135.916	-.-
55	PH	-184.256	376.380	-.-	116.084	-.-
56	HH	0	429.674	16.739	90.000	87.769
57	HH	408.644	132.777	-.-	18.000	-.-
58	HH	252.556	-347.614	-.-	306.000	-.-
59	HH	-252.556	-347.614	-.-	234.000	-.-
60	HH	-408.644	132.777	-.-	162.000	-.-

APPENDIX C

Mechanical construction of the 4π detector

Fig.C1	The hexagonal crystal
Fig.C2	The pentagonal crystal
Fig.C3	Hexagonal honeycomb of the supporting structure
Fig.C4	Pentagonal honeycomb of the supporting structure
Fig.C5	Triagonal flange for the fixation of the hexagonal crystal in the supporting structure
Fig.C6	Triagonal flange for the fixation of the pentagonal crystal in the supporting structure
Fig.C7	Glass fibre tube for fixation of the hexagonal crystal
Fig.C8	Glass fibre tube for fixation of the pentagonal crystal
Fig.C9	Ground frame for fixation of the spherical honeycomb structure

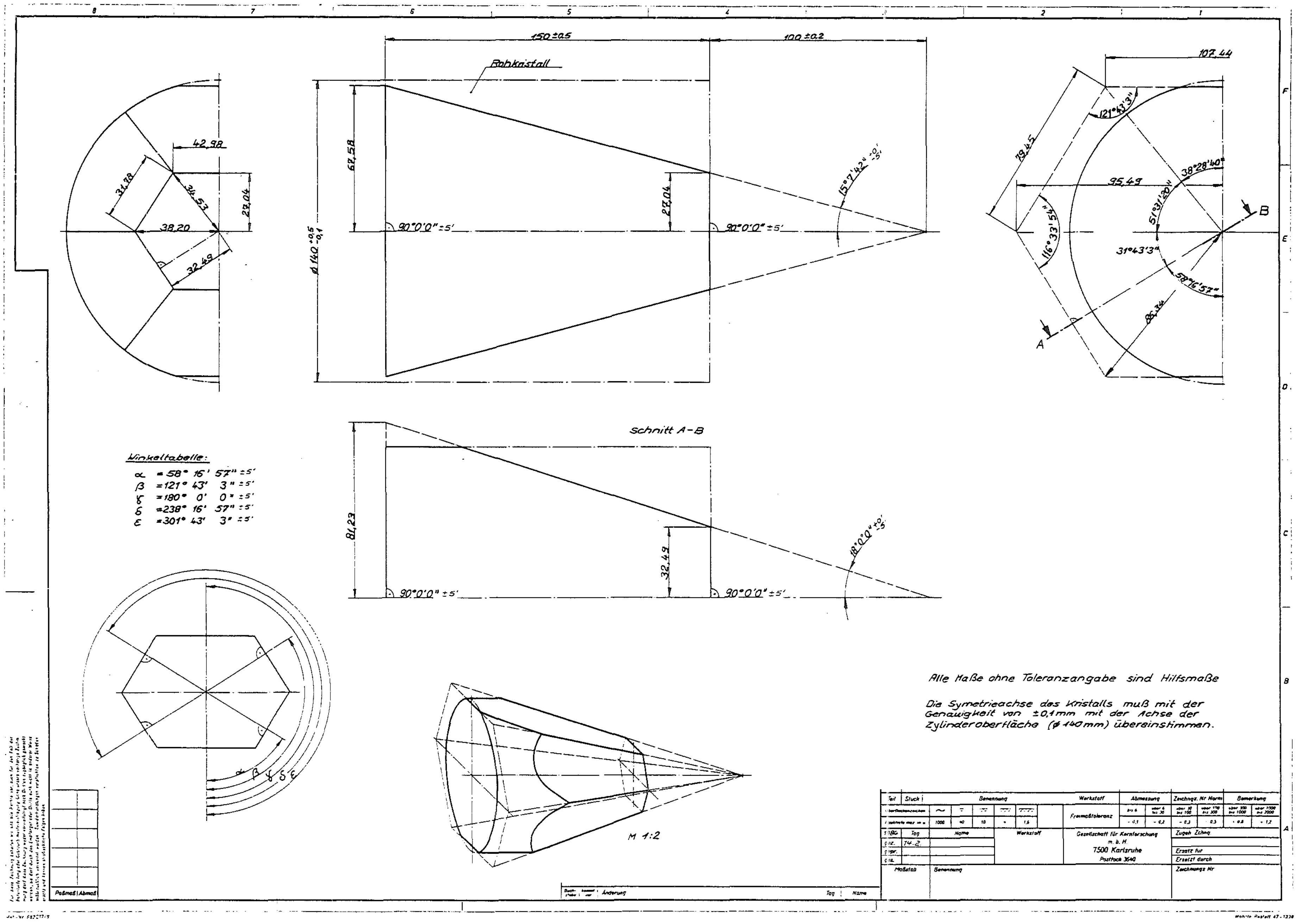

150 ±0,5
100 ±0,2
Rohkristall
107,44
42,98
34,78
34,53
27,04
38,20
32,49
67,58
ø 140 +0,5 -0,1
90°0'0" ±5'
15°7'42" +0' -5'
79,45
121°43'3"
38°28'40"
95,49
51°31'20"
116°33'54"
31°43'3"
58°16'57"
86,34
A
B
Schnitt A-B
Winkeltabelle:
α = 58° 16' 57" ±5'
β = 121° 43' 3" ±5'
γ = 180° 0' 0" ±5'
δ = 238° 16' 57" ±5'
ε = 301° 43' 3" ±5'
84,23
32,49
18°0'0" +0' -5'
α β γ δ ε
M 1:2
Alle Maße ohne Toleranzangabe sind Hilfsmaße
Die Symetrieachse des Kristalls muß mit der Genauigkeit von ±0,1mm mit der Achse der Zylinderoberfläche (ø 140mm) übereinstimmen.
Gesellschaft für Kernforschung m. b. H.
7500 Karlsruhe
Postfach 3640

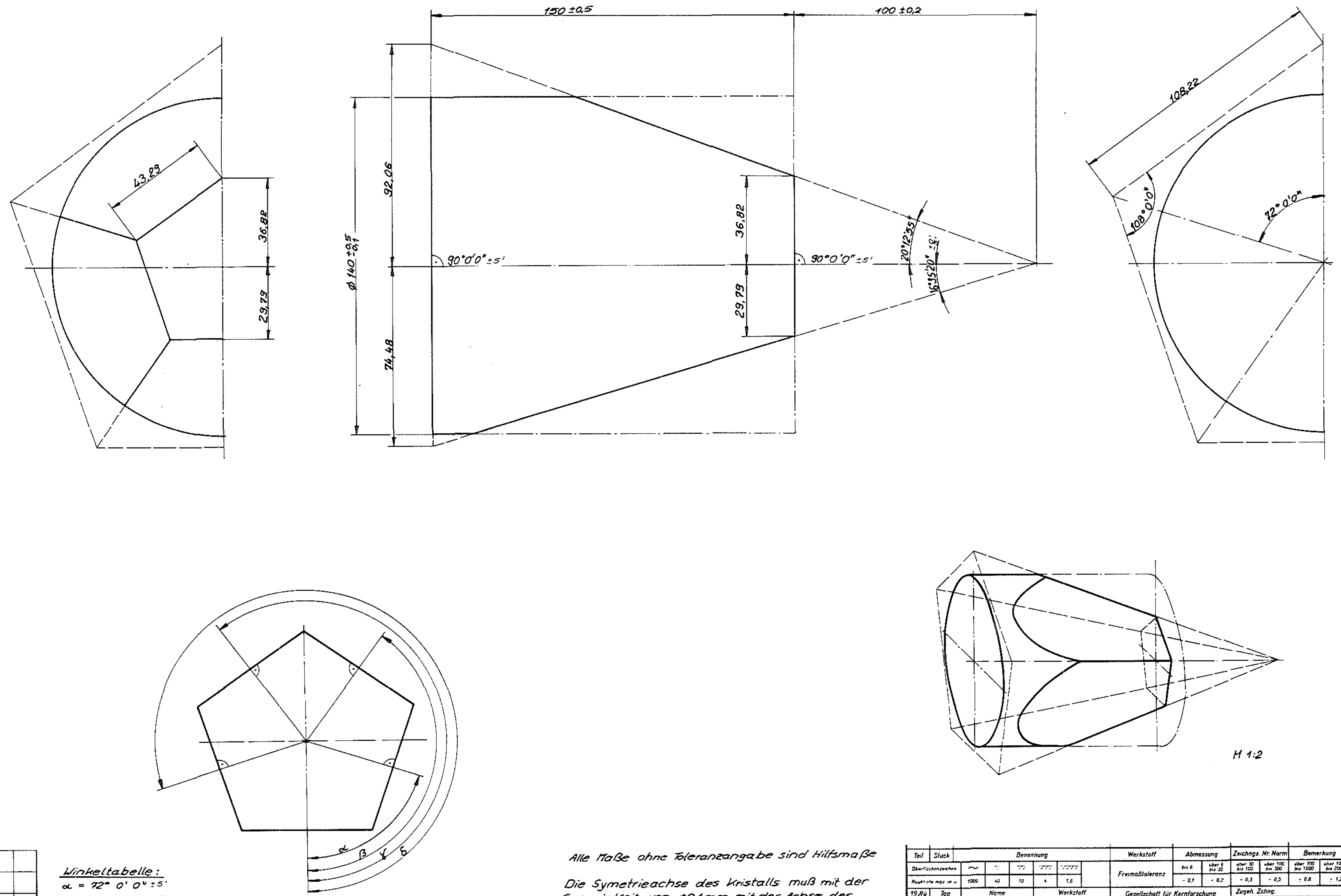

Winkeltabelle:

α = 72° 0' 0" ±5'
β = 144° 0' 0" ±5'
γ = 216° 0' 0" ±5'
δ = 288° 0' 0" ±5'

Alle Maße ohne Toleranzangabe sind Hilfsmaße

Die Symetrieachse des Kristalls muß mit der Genauigkeit von ±0,1 mm mit der Achse der Zylinderfläche (ϕ 140 mm) übereinstimmen.

Teil	Stück	Benennung						Werkstoff	Abmessung		Zeichngs. Nr. Norm		Bemerkung	
Oberflächenzeichen		~	▽	▽▽	▽▽▽	▽▽▽▽		Freimaßtoleranz	bis 6	über 6 bis 30	über 30 bis 100	über 100 bis 300	über 300 bis 1000	über 1000 bis 2000
Rauhtiefe max. in µ		1000	40	10	4	1,6			±0,1	±0,2	±0,3	±0,5	±0,8	±1,2

1984	Tag	Name	Werkstoff	Gesellschaft für Kernforschung m. b. H. 7500 Karlsruhe Postfach 3640	Zugeh. Zchng.
gez.	13.2				
gepr.					Ersatz für
ges.					Ersetzt durch
Maßstab	Benennung				Zeichnungs Nr.

Buchstabe	kommt vor	Änderung	Tag	Name

Paßmaß	Abmaß

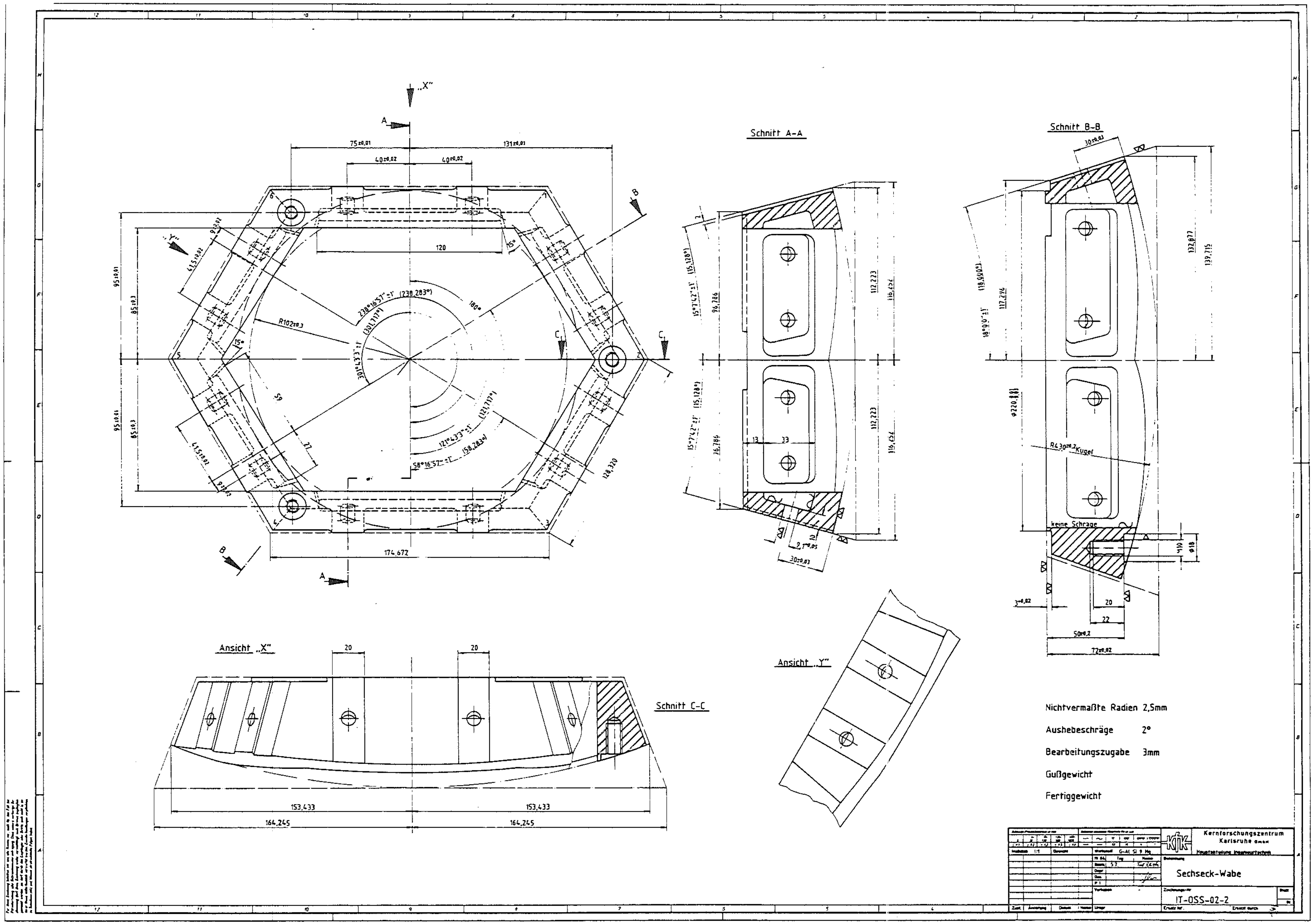

Schnitt A-A
Schnitt B-B
Ansicht „X"
Schnitt C-C
Ansicht „Y"
R430±0,2 Kugel
keine Schräge
Nichtvermaßte Radien 2,5mm
Aushebeschräge 2°
Bearbeitungszugabe 3mm
Gußgewicht
Fertiggewicht
Kernforschungszentrum Karlsruhe GmbH
Sechseck-Wabe
IT-OSS-02-2

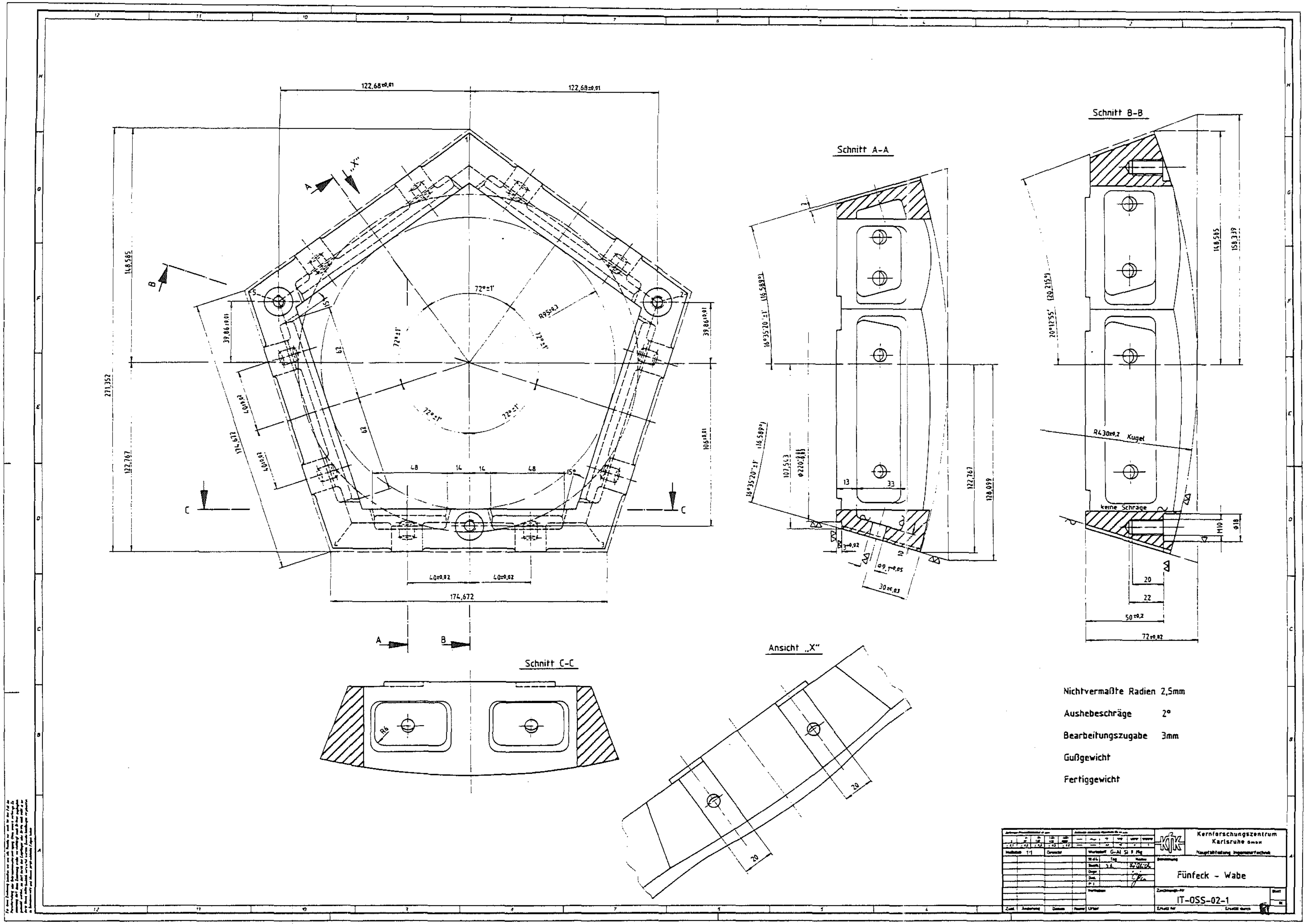
Schnitt A-A
Schnitt B-B
Schnitt C-C
Ansicht „X"
72°±1'
R95±0,2
R430±0,2 Kugel
keine Schräge
122,68±0,01
174,672
271,352
Nichtvermaßte Radien 2,5mm
Aushebeschräge 2°
Bearbeitungszugabe 3mm
Gußgewicht
Fertiggewicht
Maßstab 1:1
Werkstoff G-Al Si 7 Mg
Kernforschungszentrum Karlsruhe GmbH
Hauptabteilung Ingenieurtechnik
Fünfeck - Wabe
IT-OSS-02-1

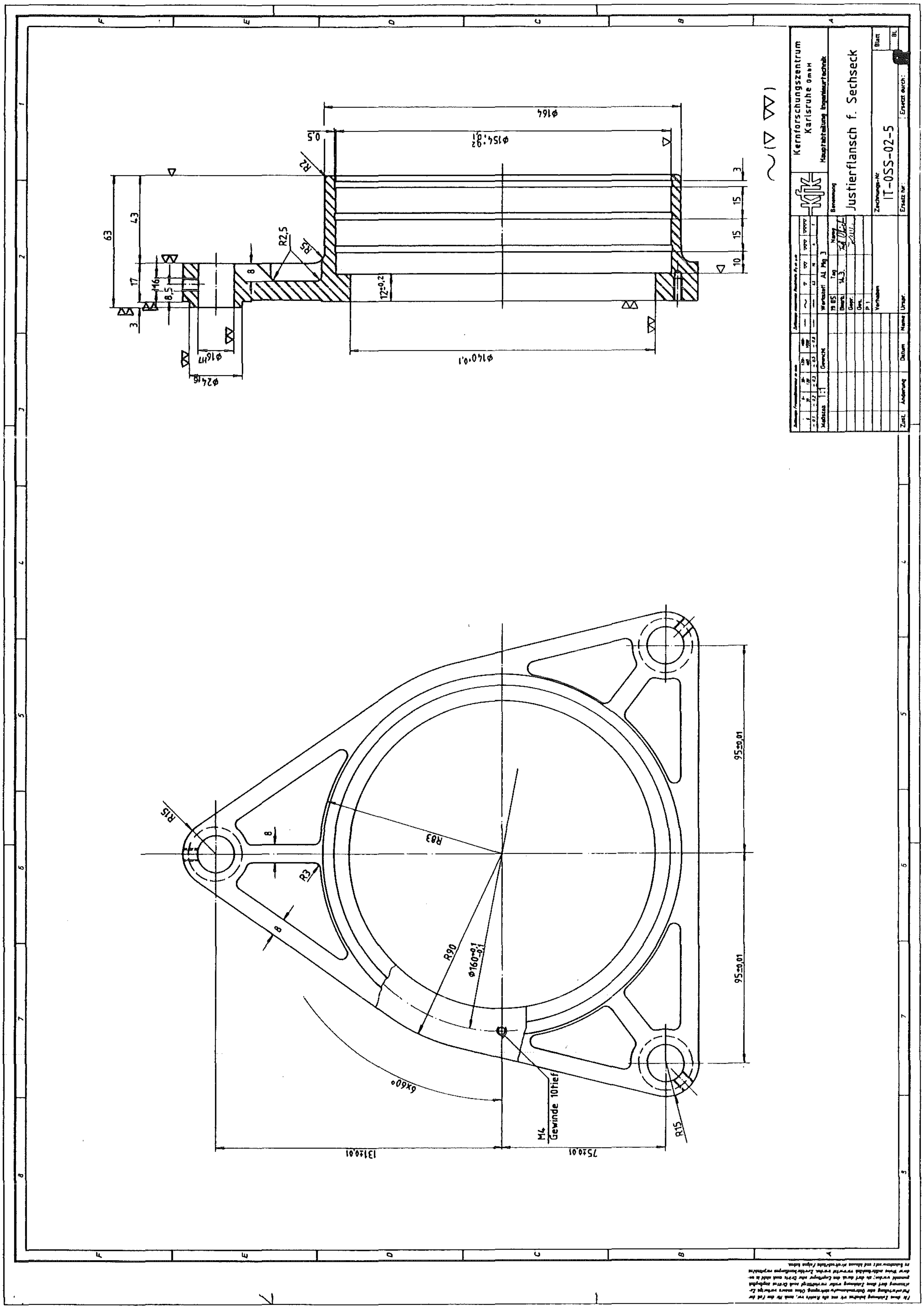
Kernforschungszentrum
Karlsruhe GmbH
Justierflansch f. Sechseck
IT-0SS-02-5
Maßstab 1:1
Ø164
Ø154
Ø140±0,1
R83
R90
R15
M4
Gewinde 10tief
6x60°
95±0,01
131±0,01
75±0,01

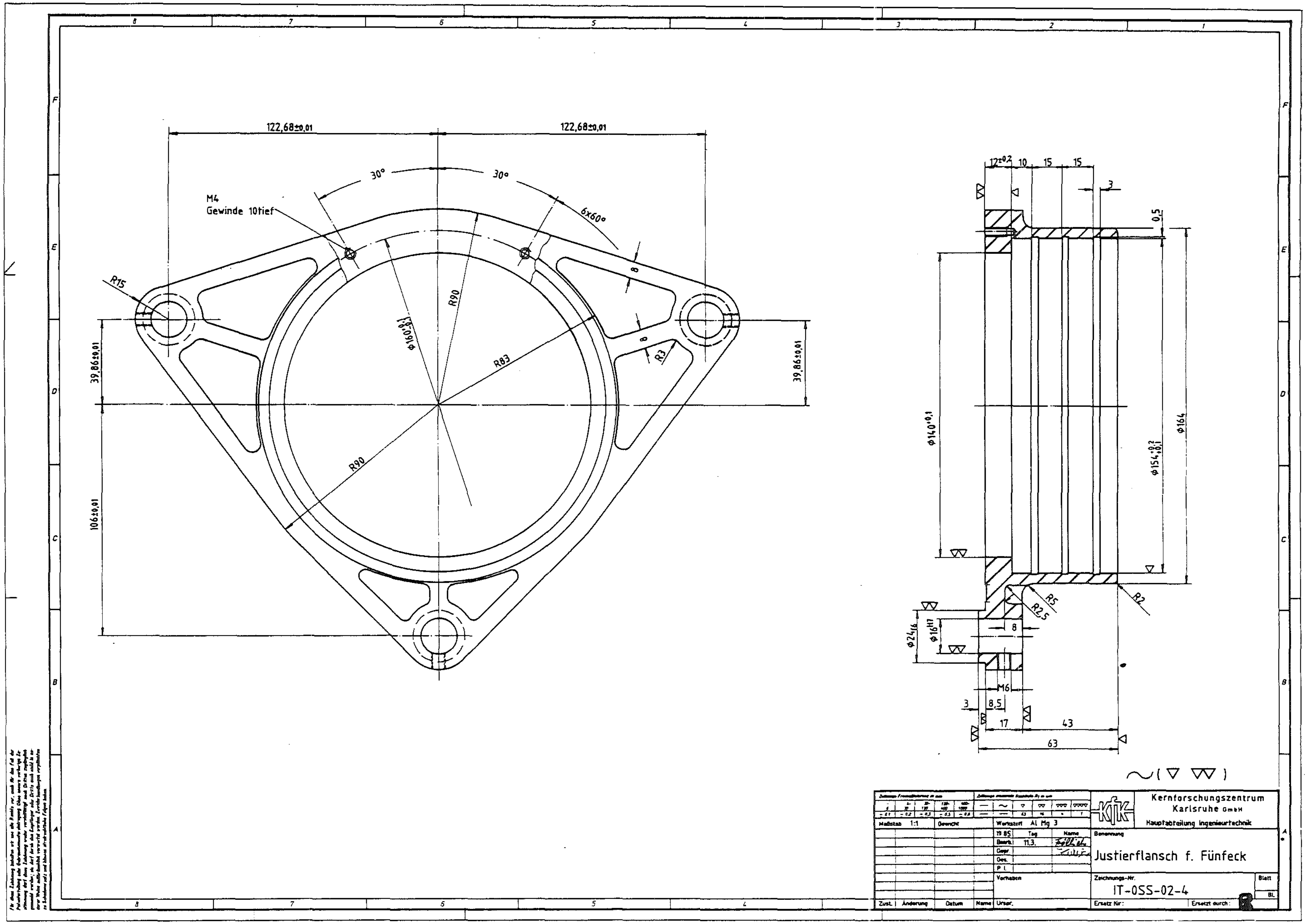

122,68±0,01
122,68±0,01
30°
30°
M4
Gewinde 10tief
6x60°
R15
R90
R83
R90
R3
8
8
39,86±0,01
39,86±0,01
106±0,01
12±0,2
10
15
15
3
0,5
ϕ140+0,1
ϕ164
R5
R2,5
R2
8
M6
3
8,5
17
43
63
Kernforschungszentrum
Karlsruhe GmbH
Hauptabteilung Ingenieurtechnik
Maßstab 1:1
Gewicht
Werkstoff Al Mg 3
19 85
Tag
Name
Bearb. 11.3.
Gepr.
Ges.
P L
Vorhaben
Benennung
Justierflansch f. Fünfeck
Zeichnungs-Nr.
IT-0SS-02-4
Blatt
Bl.
Zust.
Änderung
Datum
Name
Urspr.
Ersatz für:
Ersetzt durch:

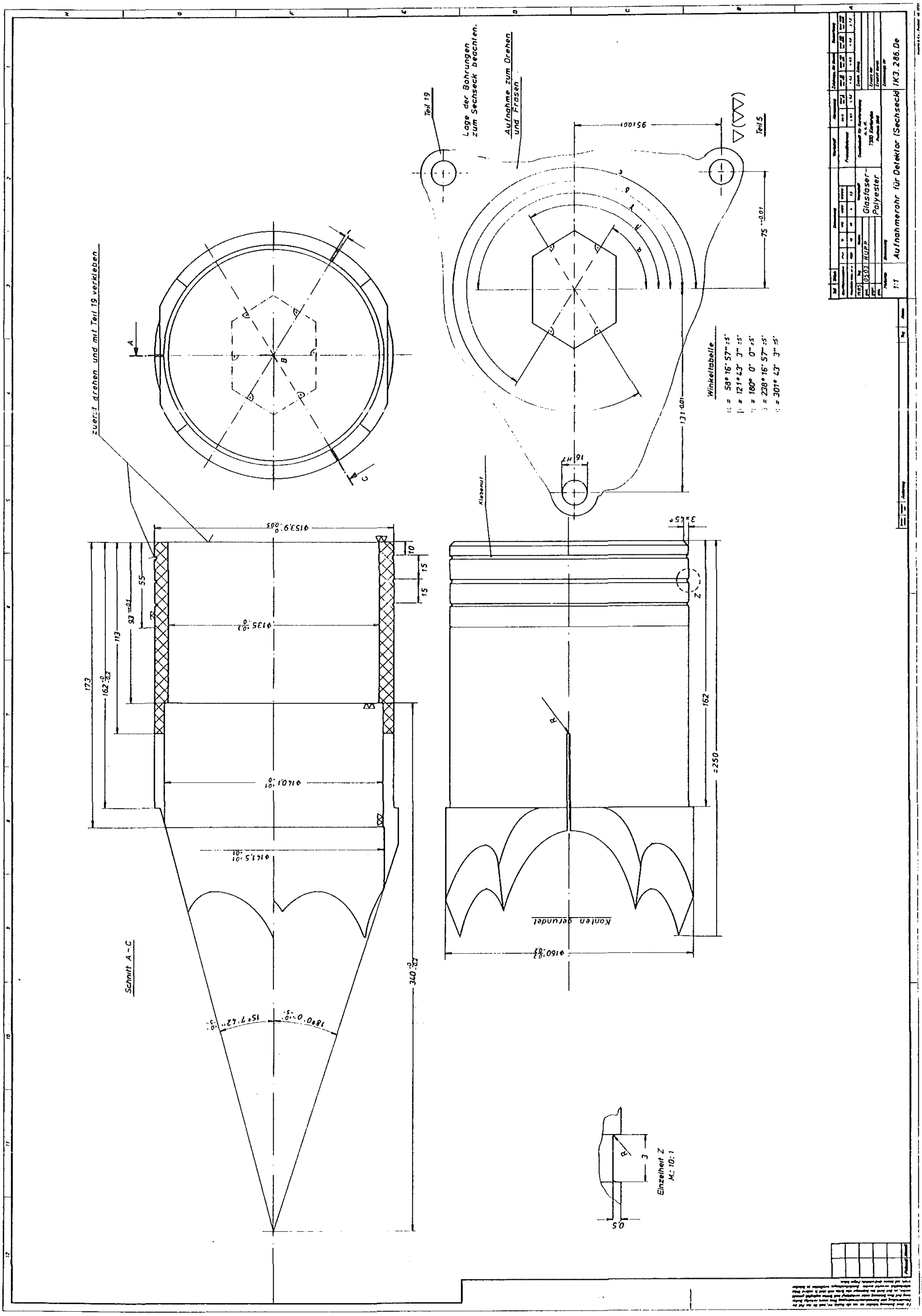
Teil 19
Lage der Bohrungen zum Sechseck beachten.
Aufnahme zum Drehen und Fräsen
Teil 5
zuerst drehen und mit Teil 19 verkleben
Winkeltabelle
58° 16' 57" ±5'
121° 43' 3" ±5'
180° 0' 0" ±5'
238° 16' 57" ±5'
301° 43' 3" ±5'
Klebenut
Kanten gerundet
Schnitt A – C
Einzelheit Z
M.: 10:1
Glasfaser-Polyester
Aufnahmerohr für Detektor (Sechseck)
1:1
1K3.286.De

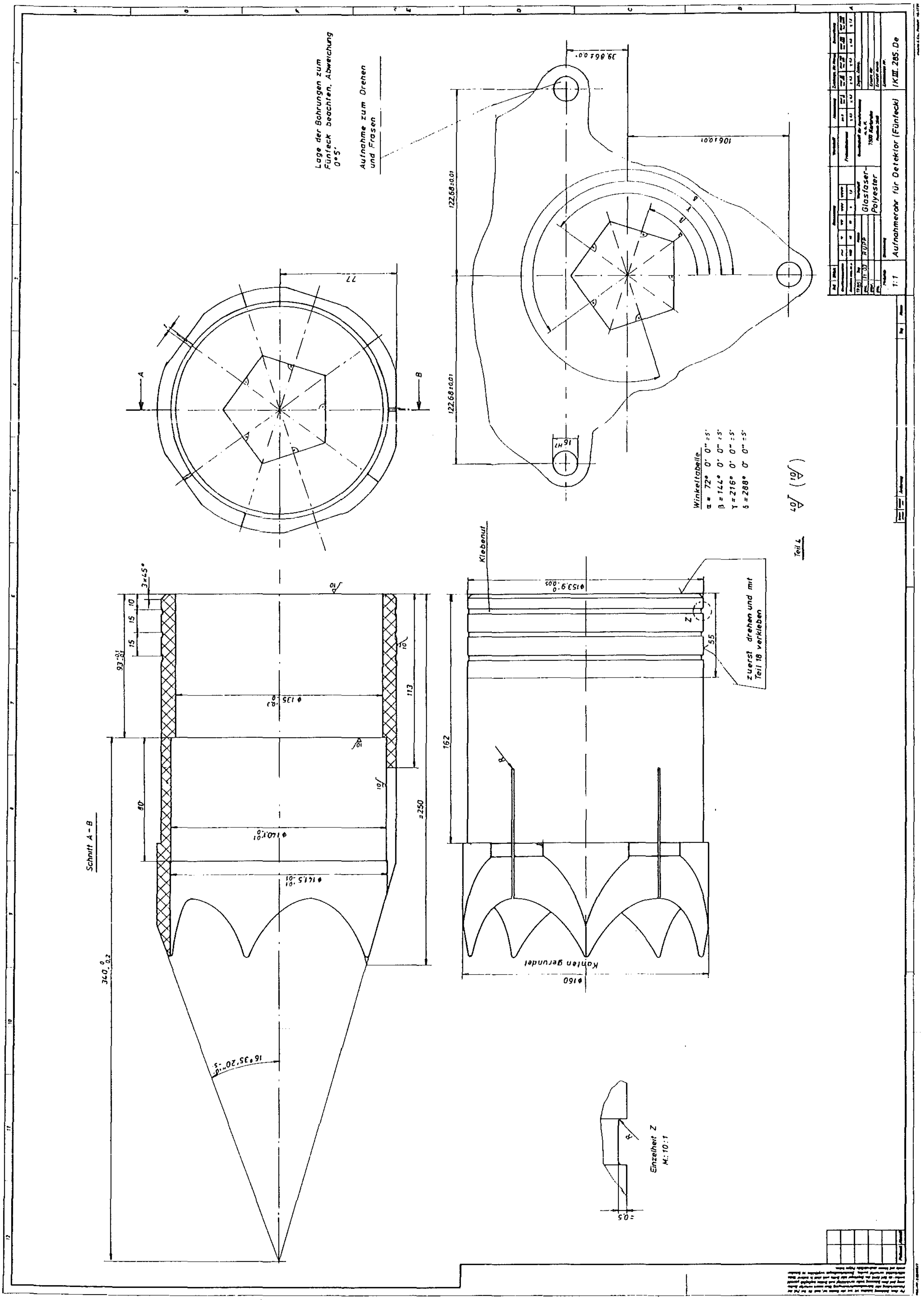
Lage der Bohrungen zum Fünfeck beachten. Abweichung 0°5'
Aufnahme zum Drehen und Fräsen
Schnitt A - B
Klebenut
zuerst drehen und mit Teil 18 verkleben
Kanten gerundet
Winkeltabelle
Einzelheit Z
M: 10:1
Teil 4
Glasfaser-Polyester
Aufnahmerohr für Detektor (Fünfeck)
IKIII.285.De
1:1

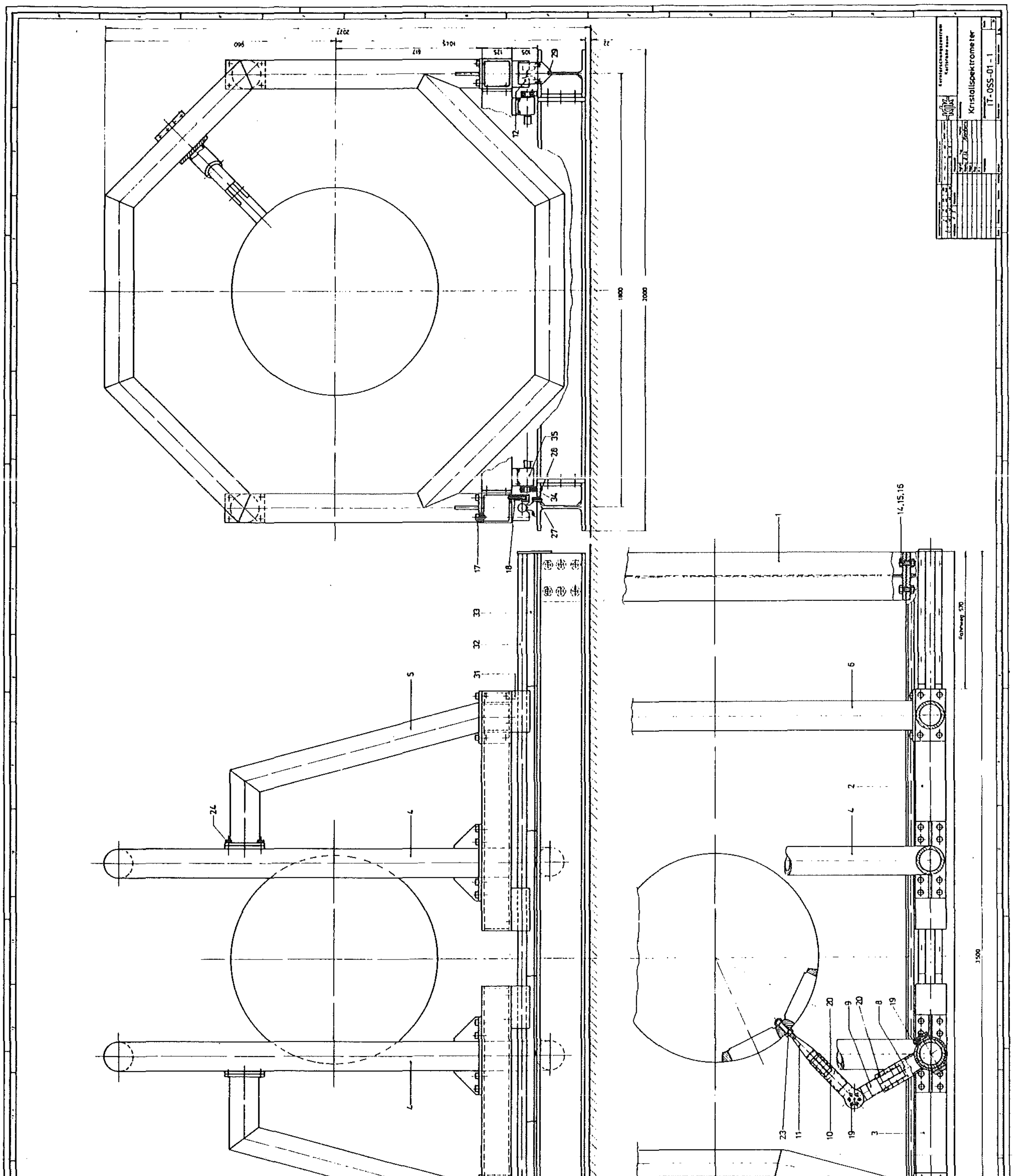
Kristallspektrometer
IT-OSS-01-1
1800
2000
3500
Fahrweg 570
Fahrweg 700

ACKNOWLEDGEMENTS

Design, setup, and operation of such an elaborate detector system was only possible by the help and enthusiasm of many colleagues at KfK and from abroad as well as from various companies. Here, we would like to express our thanks to all who contributed to the success of this project.

In particular we are indebted to Mrs. H. Braun for her care and patience in fabricating the many electronic modules and more than thousand cable connections, and to O. Walz for the adjustment and tests of the home made CAMAC electronics. We although thank Mrs. J. M. Fröhlich for the many drawings and D. Adami for his excellent machining of the complicated honeycomb structure.

Our work was greatly facilitated by the fact that we could make use of the experience from the construction of the Heidelberg crystal ball detector. Thanks to the generous support by Prof. D. Habs and R. Repnow (MPI für Kernphysik Heidelberg), H. Farr and P. von Walter (Elektroniklabor des Physikalischen Instituts, University of Heidelberg), and E. Malwitz (GSI Darmstadt) practically all aspects of the detector development including geometry, mechanical construction, electronics, and automatic operation were influenced and facilitated. In an early stage of the project F. E. Beck from the CRN Strasbourg kindly provided us with the first information on BaF_2 scintillators.

Last but not least thanks are due to Dr. K. Korth and E. Merck, the companies which supplied our BaF_2 crystals. Persisting efforts of G. Karschnik, C. D. Knöchel and J. Korth were necessary to produce large crystals with the particular quality that now make the detector so outstanding.